The Development of a Patient-Specific, Open Source Computational Fluid Dynamics Tool to Comprehensively and Innovatively Study Coarctation of the Aorta in a Limited Resource Clinical Context

LIAM SWANSON

Supervised by: Dr Malebogo Ngoepe

Co-Supervised by: Prof Liesl Zuhlke

University of Cape Town

Department of Mechanical Engineering

November 2019

WORDS: 29000

PLAGIARISM DECLARATION

1. I know the meaning of plagiarism and declare that all the work in the document, save for that which is properly acknowledged, is my own. This thesis/dissertation has been submitted to the Turnitin module (or equivalent similarity and originality checking software) and I confirm that my supervisor has seen my report and any concerns revealed by such have been resolved with my supervisor.
2. I have used the IEEE convention for citation and referencing. Each significant contribution to, and quotation in, this report/project from the work(s) of other people has been attributed, and has been cited and referenced

Signature … Signed by candidate

ABSTRACT

Congenital heart disease (CHD) has a global prevalence of 8 per 1000 births [1] and coarctation of the aorta (CoA) is one of the most common defects with a prevalence of 7% of all cases. The occurrence of CHD in Africa is estimated to be significantly lower, which is attributed to a lack of data [2]. This emphasises the restricted human resources, as well as diagnostic and intervention capacity of specialists in Africa which leads to delayed treatment, presentation with established severity and, consequently, a worse prognosis.

Computational Fluid Dynamics (CFD) is seen as the tool that will lead to a better understanding of the haemodynamic effects caused by the malformations related to CoA and provide insights into post-repair morbidity. In addition, the development of a computational tool is envisaged to improve the clinical capacity for diagnosis as well as provide a tool to conduct *in silico* repair planning. In a low and lower-middle income country healthcare facility, the supplementary data that CFD can provide can add diagnostic value, plan interventions to be more effective and efficient, as well as provide data that may improve post-repair patient management.

The aim of this project is to develop a patient-specific, open source, computational fluid dynamics toolchain that is able to study the haemodynamics relating to CoA. In order to do so, a protocol for the collection of doppler echocardiography (echo) and CTA data is proposed. The method for processing the echo data and manually segmenting the CTA data is presented and evaluated. The open source, OpenFOAM code is used to simulate a patient-specific CoA case as well as two *in silico* designs of coarctation repairs based on expanding the coarctation from the original dataset.

The CFD toolchain was developed such that patient data collected from the hospital could be processed to present key haemodynamic metrics such as velocities in the field at the coarctation zone, the pressure gradient across the coarctation and volumetric flow rates through each supra-aortic branch. These results are obtained for each case's geometry, and the trends and impacts that increasing the coarctation ratio has on each of the haemodynamic metrics is presented. The results show that the coarctation pressure gradient and maximum coarctation velocity decrease while perfusion of the lower limbs recovers with expanding coarctation ratio.

Following an analysis of the results, it is evident that the pipeline is capable of running patient-specific CFD simulations and can present clinically relevant results. It is noted that this work is a proof of concept and so several steps are discussed that will improve the pipeline.

ACKNOWLEDGEMENTS

The research that was conducted in this paper is the result of truly invaluable contributions from many people without whom the progress and success would not have been possible.

1. I would first and foremost like to thank my supervisor, Dr Malebogo Ngoepe, for all your teachings, guidance and support over the course of the study. I sincerely appreciate your will to help beyond call of duty and patience throughout the process as well as the exposure to cardiovascular biomechanics and beyond that you have given me.
2. Thank you to my co-supervisor, Professor Liesl Zühlke for your support in the clinical aspects of the project as well as your support and guidance through each conference and abstract submission. It has been a pleasure to be a part of the research and thank you for your work in co-ordinating the PROTEA project such that it becomes what it is today and given me the opportunity to experience so much.
3. Thank you to my University of Manchester engineering supervisors, Dr Alistair Revell and Dr Ben Owen, for your patience and teachings and for making my stay at Manchester such an incredible experience.
4. Thank you to Professor Bernard Keavney for your key role in the DJEMBE and PROTEA projects and for your guidance and financial support throughout conference processes.
5. This research has rested so heavily on obtaining sufficient data to carry out investigations. This would not have been possible without the team at the Red Cross War Memorial Children's Hospital: Prof John Lawrenson, Prof Rik de Decker, Dr Thomas Aldersley, Dr George Comitis and Dr Barend Fourie. The help in developing data collection protocols, identifying patients and collecting data has made this possible. Your willingness to field my questions and teach me beyond the scope of the project has taught me so much for which I am grateful.
6. Thank you to the CSIR HPC team for access to the Lengau Cluster. Thanks go specifically to Charles Crosby for facilitating my work on the HPC and guiding me through the process.
7. I would like to sincerely thank the University of Cape Town, National Research Foundation, Harry Crossley Foundation and Oasis Crescent Fund Trust for your generous financial support that has made my two years possible. In addition, I have gratitude for the financial support by the MRCUK for their support of the DJEMBE project.
8. Finally, an enormous thank you to my family and friends for their relentless support, patience and understanding through all ups and downs and for making the time aside from work so much fun

CONTENTS

LIST OF FIGURES

1. LIST OF TABLES

NOMENCLATURE

SCALARS		VECTORS	
$\boldsymbol{P}$	Pressure	$\boldsymbol{u}$	Velocity Vector
$\boldsymbol{K}$	Modified Bernoulli Equation Constant	$\underline{\boldsymbol{n}}$	Surface Normal
$\boldsymbol{v_{max}}$	Maximum Velocity Magnitude	$\boldsymbol{g}$	Body Force (Gravity)
$\boldsymbol{\theta}$	An Angle (Degrees)	$\boldsymbol{c}$	Area Vector of Cell Face
$\boldsymbol{\phi}$	Scalar Fluid Property	$\underline{\boldsymbol{x}}$	Eulerian Position Vector
$\boldsymbol{\rho}$	Fluid Density	$\underline{\boldsymbol{X}}$	Lagrangian Position Vector
$\boldsymbol{u_x/u}$	x-component of Velocity	$\mathbf{x}$	Cell Vertex Position
$\boldsymbol{u_y/v}$	y-component of Velocity		Second Order Tensors
$\boldsymbol{\mu}$	Dynamic Viscosity	$\boldsymbol{T}$	General Stress Tensor (2nd Order)
$\boldsymbol{A}$	Area	$\boldsymbol{D}$	Constitutive Tensor
$\boldsymbol{m}$	Mass	$\boldsymbol{\tau}$	Stress Tensor
$\boldsymbol{a}$	Upwinding Coefficient	**OPERATORS**	
$\boldsymbol{\alpha_p}$	Pressure Relaxation Factor	$\boldsymbol{\nabla}$	Nabla
$\boldsymbol{\alpha_v}$	Velocity Under Relaxation Factor	$\frac{D}{Dt}$	Lagrangian Partial Derivative
$\boldsymbol{D}$	Diameter	$\frac{\partial}{\partial t}$	Eulerian Partial Derivative
$\boldsymbol{R}$	Coarctation Ratio	Δ	Delta/Change In
$\boldsymbol{L}$	Length	**GEOMETRY LABELS**	
$\boldsymbol{V}$	Volume	f	Cell Face
$\boldsymbol{t}$	Time	n	A Point in Time
REFERENCE FRAMES		C	A Bounding Curve
$(\boldsymbol{x}, \boldsymbol{y}, \boldsymbol{z})$	Eulerian Co-ordinate	S	Surface
$(\boldsymbol{X}, \boldsymbol{Y}, \boldsymbol{Z})$	Lagrangian Co-ordinate		

ACRONYMS

3EWM	Three Element Windkessel Model
BC	Boundary Condition
CFD	Computational Fluid Dynamics
CFL	Courant-Friedrichs Lewy
CHD	Congenital Heart Disease
CSIR	Council for Scientific and Industrial Research
CTA	Computed Tomography Angiography
CVD	Cardiovascular Disease
FVM	Finite Volume Method
FEM	Finite Element Method
FSI	Fluid-Solid Interaction
GUCH	Grown Up Congenital Heart Disease
HPC	High Performance Computing
LCCA	Left Common Carotid Artery
LSCA	Left Subclavian Artery
MRI	Magnetic Resonance Imaging
OSI	Oscillatory Shear Index
PC-MRI	Phase Contrasted Magnetic Resonance Imaging
PISO	Pressure Implicit with Splitting Operators
QUICK	Quadratic-Upwind-Interpolation for Convective Kinetics
ROI	Region of Interest
RTT	Reynold's Transport Theorem
RXH	Red Cross Memorial Children's Hospital

SIMPLE	Semi-Implicit Method for Pressure-Linked Equations
TAWSS	Time Averaged Wall Shear Stress
TTE	Transthoracic Echocardiography
WSS	Wall Shear Stress

ABBREVIATIONS

CoA	Coarctation of the Aorta
DAo	Descending Aorta
Echo	Echocardiography

1. INTRODUCTION

This chapter gives context to the research which is presented in this dissertation by introducing congenital heart disease and coarctation of the aorta and describing its relevance to Africa and synergies with computational fluid dynamics. An overview of the research is then provided through discussing the objectives, scope of the research and the plan of development of the dissertation

1.1 BACKGROUND AND PROBLEM STATEMENT

Congenital heart disease (CHD) is the subset of cardiovascular disease (CVD) where a paediatric patient is born with a malformation of their cardiovascular structures. The range of different types of abnormalities that may occur is vast and vary in degrees of severity and complexity. CHD has a global prevalence of 8 per 1000 births [1] and coarctation of the aorta (CoA) is one of the most common with a prevalence of 7% of all CHD cases. This rate, as well as the survival rate, has been shown to have significant variations if segmented geographically or by regional wealth [1].

CHD in Africa is seen to deviate significantly from the global rate with a reported prevalence of 1.9 cases per 1000 births. This highlights a lack of readily available data in low income regions and casts doubt as to the true representation of the prevalence in Africa [2]. The potential for underestimation is substantiated by a localised study conducted by Marijon *et al.* [3] who, in a study of 2170 public school students between the age of 6 and 17 years in Maputo, Mozambique, diagnosed four children with a CHD who previously were undiagnosed. This gives a prevalence of 2.3 cases per 1000 children but, importantly, emphasises the lack of diagnostic ability in poorer regions of Africa which leads to delayed treatment, more severe cases being presented and, consequently, worse prognosis.

From a human resources perspective, 3% of the world's healthcare professionals operate in Africa, which carries 24% of the global disease burden. In contrast, the Americas home 37% of healthcare professionals while only carrying 10% of the global disease burden [4]. A study at the *Instituto do Curaçao* in Mozambique showed that only 53.8% of patients were diagnosed before the age of two. This is in stark contrast to the developed nations that on average will diagnose 60% of cases within one month of birth [5]. Solutions which improve the capacity to effectively and efficiently diagnose and treat patients in novel ways will be vital if the prognosis of a child who is born with a congenital heart disease is to improve in countries where resources are limited and especially when considering that the morbidity after repair is so linked to the speed of intervention [1].

In CoA specifically, it is postulated that the repair of the coarcted site can cause alterations to the haemodynamics in the region which may lead to long term morbidities such as secondary hypertension and recoarctation despite the repair being considered a success [6], [7]. In addition, increases in wall shear stress (WSS) and decreases in the oscillatory shear index (OSI) have been associated with a higher susceptibility to atherosclerosis [8]. The synergies between computational fluid dynamics (CFD) and the study of haemodynamics in the highly variable geometries of CHD illustrates a high potential for the development of patient-specific studies for CoA [9].

In coarctation of the aorta specifically, CFD is seen as the tool that will lead to a growing understanding of the haemodynamic effects caused by coarctation and the repairs which will provide insight into post repair morbidity. In addition, the development of a computational tool improves the clinical capacity by allowing clinicians to supplement diagnostic data and conduct *in silico* repair planning [10], [11].

1.2 OBJECTIVES

The objective of this research is to develop a computational fluid dynamics tool based on an open source pipeline that gathers patient-specific data and ultimately produces haemodynamic metrics of a diseased aorta as well as *in silico* generated repairs. To achieve this, a patient data collection protocol was to be developed in collaboration with a team of clinicians at the Red Cross War Memorial Children's Hospital (RXH) to obtain geometry, pressure and velocity data of the specific CoA case. Following data acquisition, an approach to geometry, velocity and pressure data pre-processing must be developed so that a CFD simulation can be conducted and the results presented. The results which are presented must be clinically relevant for diagnostic, *in silico* repair planning or for insight into the pathophysiology that exists.

The objective of this study is to show that it is possible to take approaches and implement methods that are clinically applicable and feasible. This requires that the pipeline be, as far as possible, based on open source software and use clinical techniques that are within standard protocol for care. This objective threads through the entire pipeline and fundamentally focusses the methodology and maintains that it be a tool that is applicable in healthcare facilities that have limited resources.

1.3 SCOPE OF RESEARCH

Each of the several constituents of this research is an area that has had specialised and detailed investigations conducted with regards to patient-specific CFD. Thus, it is important to define

a clear scope of research so that the objectives are reached and that expectations as well as the time frame is managed correctly.

The global scope of the project is that open source software packages be prioritised where necessary and possible. The packages used included SimVascular (release 19.01.27) [12] for image segmentation, ANSYS ICEM CFD (19.2 Academic Licence) for finite volume meshing, Plot Digitizer [13] for data processing, OpenFOAM (version 6), for numerical simulation and ParaView (version 5.6) for results post processing. The project does not compare or evaluate the software packages themselves. Nor does it compile these constituents into one black box style software package where data transfer and processing is automated.

The data collection protocol is developed in collaboration with clinicians and is restricted to modalities that were agreed to be within ethical and clinical protocols. The research acknowledges and presents the different modalities that are implemented in literature but, with consideration for the resources found at RXH as well as patient safety, the project does not assess the different modalities. The modalities that are used are computed tomography angiogram (CTA) and doppler echocardiography (echo).

The segmentation methods which are used are only those which are available in the SimVascular software package. A full comparison of different segmentation methods is out of scope and so methods are constrained to manual and thresholding segmentation. *In silico* repair design testing requires the development of further test geometries. These geometries could not be developed with clinical data and so had to be developed in collaboration with clinical teams at RXH. The geometries which are developed are done so through a methodical approach, albeit an educated approximation and collaboratively sanity-checked with the clinical specialists. The study tests three geometries. This does not constitute a parametric study of the expansion of the coarctation and so remains as an indicative result as to the impact that an expansion has on the haemodynamics.

Volumetric discretisation was conducted in ANSYS ICEM CFD (19.2 Academic). A grid independence study was conducted to ascertain adequate refinement, however, a comprehensive study to optimise the mesh through cell types or optimum boundary layer parameters was not considered necessary at this time. In the name of the open source objective, the study proposes open source alternatives but does not evaluate, compare or use meshes that may be derived from them.

While OpenFOAM enables users to customise code, the boundary conditions (BC(s)), numerical schemes and numerical solvers that were implemented were kept as those that were available as standard with the installation. The development of specific solver and boundary condition code and its validation is currently seen as out of scope. The steady state, Newtonian

viscosity and laminar flow assumption which is made is not compared to transient or alternative viscosity models at this conceptual development phase. To incorporate turbulence and non-Newtonian fluid models is out of scope but considered as future work.

Results processing focusses on the clinically relevant haemodynamic metrics which can be derived from the pressure and velocity fields. Due to the steady state nature of the simulation, other clinical metrics such as time-averaged wall shear stress (TAWSS) and the oscillatory shear index (OSI) are not included in the analysis.

Importantly, the results which are obtained, although both qualitative and quantitative in nature, are not rigorously validated with *in vivo* or *in vitro* experimental results as this was not possible. The results are thus compared to the data which was originally obtained and highlights where errors exist and where improvements are required to be made.

1.4 PLAN OF DEVELOPMENT

This report begins by giving an overview of the clinical theory regarding the background of CoA, its diagnosis and repair techniques as well as how current literature has recognised and implemented CFD numerical modelling in studying the haemodynamics in the diseased vessels. An in-depth review of the current state of the art in patient-specific CFD modelling of cardiovascular disease and the relevant numerical techniques that are applied is then conducted. In this review focus is placed on data acquisition techniques, the implementation of different boundary conditions and the results which have been obtained by literature previously.

After establishing a grounding in the current literature, the fundamental principles which underpin the finite volume method used for this numerical modelling are revised. In addition, the fundamental principles behind medical imaging modalities which define and differentiate them is discussed. Based on these fundamental principles and the knowledge of current literature in cardiovascular and CoA haemodynamic modelling, the method which was followed for each phase in the pipeline is described. The results of each constituent in the methodology are then presented and discussed in relation to how they achieve or align with the objectives laid out previously.

To conclude, a summary of the research is presented and accompanied by a set of recommendations for future line of work based on this foundation.

2. LITERATURE REVIEW

This chapter provides an overview of the fundamental theory relating to coarctation of the aorta, its pathophysiology and current repair techniques. This gives context to the space in which a patient-specific CFD tool should be considered. The current research which is being conducted in each CFD pipeline constituents' field is then investigated with the aim of informing methodology development and understanding how CFD has been implemented in cardiovascular disease before.

2.1 OVERVIEW OF COARCTATION OF THE AORTA:

2.1.1 Background

Coarctation of the aorta (CoA) is a congenital heart defect where there is a local narrowing or folding of the arterial wall at the aortic isthmus in the descending aorta as shown schematically in Figure 2-1. This can also be referred to as a stenosis and many variations in its severity, complexity and location have been found [1], [14].

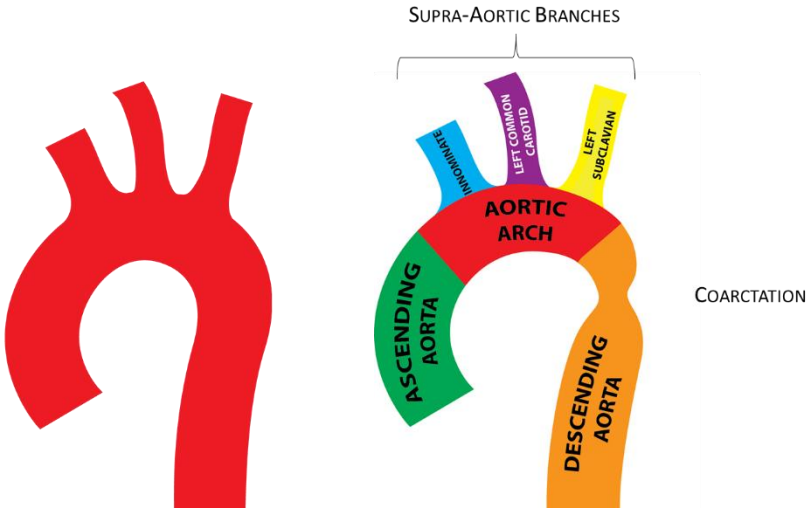

Figure 2-1: Schematic of a coarctation of the aorta case (right) compared to a normal aorta structure (left).

These variations highlight the patient-specific nature of this CHD, but ultimately the common result of CoA is the increased resistance to flow through the coarctation to the distal arterial network. Consequently, the central aortic pressure is elevated while the blood pressure distal to the coarctation drops. The difference between the pressure values proximal and distal to the coarctation at peak systole is referred to as the pressure gradient in a clinical setting and carries implications to the health of the patient. Systemic hypertension, left ventricular afterload, hypoperfusion of the lower limbs, increased turbulence in flow distal to the coarctation and the potential for collateral vessel formation are risks that are closely linked to the degree of stenosis and by implication the magnitude of the pressure gradient. These consequently

increase the risk of morbidities, among others, such as left ventricular hypertrophy, cardiac failure, accelerated atherosclerosis and persistent hypertension which results in a poor prognosis if the coarctation is untreated [15].

The consequence of a delayed treatment of CoA places pressure on clinicians to make an early and accurate diagnosis and plan a treatment approach. From an engineering perspective, it has been found that pressure and velocity information that would inform such a diagnosis is obtainable through CFD studies [10], [11]. The synergies between computational modelling of haemodynamics and the clinical protocol in managing patients with CoA and CHD as a whole, has led to an expansion of this field of engineering research [16]. However, the treatment and management procedures of CoA should first be understood to give context to the aims and methodologies of current CFD research in CHD and highlight its potential areas of implementation as well. Of particular importance in this consideration is the clinical challenges which limited resource healthcare facilities face and how they translate into either barriers or potential gaps for the application of CFD.

2.1.2 Coarctation of the Aorta Diagnosis Techniques

CoA will present with signs and symptoms that depend on the severity of the coarctation. To finalise a diagnosis, an investigation may utilise a combination of invasive and non-invasive techniques which each provide different metrics that may cross-validate a certain diagnosis. The main modalities that are currently applied in various combinations and settings are catheter pressure gradient measurements, cuff pressure measurements, doppler echocardiography (echo), cardiac magnetic resonance imaging (MRI), CTA, 3D rotational angiography and x-ray angiograms [1]. The different combinations of these methods provide information regarding blood flow velocities, pressure measurements and volumetric information of the diseased structures. A clinician's analysis of this data will form the basis of their planning of the treatment approach.

The benchmark for coarctation intervention has been defined as the point where the pressure gradient across the coarctation at peak systole exceeds $20\,mmHg$ [1]. However, echo-measured flow continuation through the descending aorta during diastole, evidence of a coarctation seen in chest x-rays, murmurs and abnormal pulses are additional markers that indicate the presence of a stenosis [17]. Each investigative modality carries advantages and disadvantages which may promote or restrict their application from patient to patient or even between different hospitals, however, each can contribute to the evidence for an appropriate diagnosis and treatment plan.

It is at this initial point in the clinical management process where current research in CFD has been shown to have its first potential role to play, not only in CHD but also in a variety of

CVD [18], [19]. Where certain modalities may provide some data in specific locations, CFD may provide high resolution detail of flow in the entire volume in easily understandable graphs and plots. It could be argued that phase-contrasted MRI (PC-MRI) can offer similar benefits, but at the very least, CFD would be able to complement this data with its high-resolution capability.

For a CFD protocol to be clinically applicable, it is vital that the data that is collected by standard clinical modalities be interpreted and leveraged by engineers for patient-specific simulations. If successfully implemented, additional information could be added to the dataset that would otherwise not be traditionally obtained and provide insight for doctors to further personalise the approach to treating the patient.

2.1.3 Coarctation of the Aorta Repair Approaches in Infants and Young Children

The primary aim of any repair is to reduce the pressure gradient caused by the coarctation to as close to 0 $mmHg$ as possible. Over the decades, techniques have been constantly improved through empirical studies and clinical experience [20]. This has resulted in today's survival rates being at least 80% on condition that treatment is received early enough [14]. However, there still remains debate regarding the superior repair strategy with persisting hypertension, aneurysm formation and, importantly, recoarctation remaining as risks [7], [14], [21], [22].

Figure 2-2 shows a schematic representation of balloon angioplasty and resection with end-to-end anastomosis (REEA). These are the two most commonly used repair strategies for neo-natal and infant paediatric patients [14]. Balloon angioplasty inflates a balloon at the site of the coarctation via a catheterisation procedure to dilate the artery to a point where slight tearing occurs. This forces the site to heal in the expanded configuration and so achieve a reduction in pressure gradient. Coarctation REEA is a surgical approach that aims to remove the length of the aorta which is affected. Although both are used, there are advantages and disadvantages of each technique which have not established one to be clearly superior to the other. For example, REEA is a far more invasive procedure which requires longer hospitalisation for recovery compared to the minimally invasive catheter-based ballooning approach. However, in comparing the long term outcomes of each methodology, it has been found that REEA has a lower risk of aneurysm formation which is favourable for long term patient well-being [22]. The decision is thus made on a patient by patient basis and is based primarily on age but can be related to the preference of the centre or specialist as well.

Regardless of the chosen repair technique, mechanistic responses occur within the aorta wall due to unfavourable or sub-optimal haemodynamics pre- and post-repair respectively. The wall shear stress and oscillatory shear index have been particularly associated with the

likelihood of developing atherosclerosis [23]. In addition it has been reported that one third of CoA patients are likely to become hypertensive later in life [6].

Research of clinical application of CFD during the repair planning phase has focussed on two areas [16]. An intrinsic strength of *in silico* studies gives the flexibility to experiment with different repair techniques to optimise a procedure so as to achieve the required pressure gradient and promote favourable haemodynamics post-repair. Within the context of the relationship between WSS and atherosclerosis, literature has shown that CFD is able to highlight areas which are at risk of unfavourable vessel remodelling [24]. In low and lower-middle income countries where the large distances between patients and their centre of care makes follow up and consultation difficult, it would be highly valuable to be able to use CFD to determine a risk factor and subsequently develop the optimal follow up care for the patient.

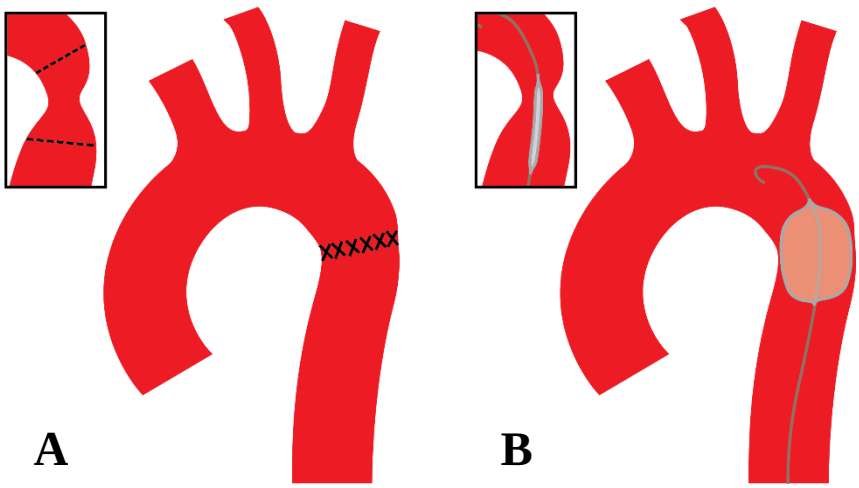

Figure 2-2: Illustration of two of the different approaches to an aortic coarctation repair in young or infant patients. A: Resection and end-to-end anastomosis. B: Balloon angioplasty and stenting.

2.1.4 Computational Fluid Dynamics and Clinical Decision Making

The probability of the development of further cardiac lesions such as atherosclerosis, hypertension, recoarctation and aneurysms is significant enough to warrant the continual screening of the patients over a lifetime. This is an expensive and strenuous routine for the patient, doctors and state healthcare systems alike. Currently the future trend shows a compounding of the effect as the cohort of grown up congenital heart disease patients (GUCH) increases [25]. The need to address demand has called for the development of new technologies that can improve surgical procedures, improve understanding of consequent lesions and improve the management of patients.

Computational mathematics and biomechanics has seen a recent maturity that establishes it as an increasingly feasible tool for modelling and studying cardiovascular haemodynamics so as to extend clinicians' capability for pre-surgical study, therapy planning and patient monitoring

[10], [16], [26], [27]. Coarctation of the aorta has been an example of a defect that has received significant attention from the CFD community due to the valuable insights that can be gained from modelling the haemodynamics. The capability of CFD has been shown to be useful in calculating the pressure gradient values [28] as well as the evaluation of WSS, TAWSS, the OSI and turbulence quantification [24]. Knowledge of this additional blood flow data empowers clinicians to be able to judge the risk of morbidity such as atherosclerosis and aneurysms [10], [11], [28], [29].

The process of conducting a patient-specific CFD study that is clinically applicable is in many ways similar to a standard CFD methodology yet there are added complexities in acquiring and processing the organic and complex patient-specific dataset. The constant consideration for clinical application in a low income country will dictate and limit the cost implications of the methodology as well as the data that is available to the engineering teams. For clinical application in countries with limited resources, these considerations are all the more important.

2.2 IMPLEMENTING CFD IN COARCTATION OF THE AORTA

The process of conducting a CFD simulation in patient-specific CHD cases has been explored and documented well in a number of cases [16], [30], [31]. It is often the case that, for capability, support and ease of use, research oriented projects use commercially available software for the bulk of the work [16]. Despite this, groups recognise the need to consolidate a package which houses a vascular haemodynamics pipeline for broad clinical application such as SimVascular [12]. In general, the process of conducting vascular haemodynamics modelling consists of these primary phases:

1. Patient-specific data acquisition
2. Medical image segmentation
3. Volume discretisation (meshing)
4. Boundary condition prescription
5. Numerical solving of the flow fields
6. Result processing, visualisation and analysis

At each point in this pipeline, there is a wide variety of techniques which have been developed and range between being simplistic and complex. As a consequence, research continues to evaluate and compare techniques towards the aim of converging towards a gold standard and consolidated approach [32]–[35]. A methodology which is focussed on being clinically applicable needs to be developed within the bounds of what data can be obtained and balance accuracy with speed of result acquisition. Working towards this goal, while remaining relevant

to emerging economy healthcare facilities, adds a layer of consideration when evaluating the methodologies which are proposed in literature.

2.2.1 Patient-Specific Data Acquisition for Computational Fluid Dynamics

The common modalities that are used by clinicians to inform their diagnostic, intervention and surgical decisions have been discussed previously in section 2.1.2. The same modalities are used to obtain the data pertaining to geometry, velocity and pressure for CFD studies, however, the way in which this data is interpreted as well as the points of interest differ from standard clinical protocol [16], [36]. Each modality has associated advantages and disadvantages for both diagnosis and computational modelling that make it applicable or preferable in different cases and institutions respectively. However, the accuracy of any simulation result is dependent on which data and the quality of such data that is used to generate the patient geometry and define the specific boundary conditions.

Every patient-specific numerical simulation that has been conducted in literature has depended on some form of data collection. Subsequently, the development of a CFD protocol should be guided by taking into account pros and cons of common approaches in literature regarding general patient-specific simulations as well as those publications which specifically compare methods. Clinical application has been emphasised as the primary goal and so, while methodologies employed by literature will be discussed, the first consideration in evaluating their relevance should be the feasibility within RXH infrastructure and protocols.

2.2.1.1 ***Patient-specific Geometry Acquisition Modalities***

CTA and MRI are leading imaging modalities due to their ability to provide geometry information in a three-dimensional space through discrete voxels. A key differentiation between these two modalities is the use of ionising radiation in CTA compared to electromagnetism in cardiac MRI. In both cases there are aspects which will lead to one being superior to the other under different circumstances. In the case of a clinically applicable CFD toolchain, the chosen methodology for data acquisition needs to align with clinical practice to enable easy assimilation and minimise ethical dilemmas.

When studying literature that implements CFD modelling in cardiovascular structures, the popular imaging modality tends towards PC-MRI [11], [36]–[38]. However, it must be noted that, in these papers, the discussion around the choice of modality does not render CTA redundant. In fact, when reminding oneself that clinical assimilation is a strong priority, a strong argument is made for the use of CTA as a clinical visualisation tool due to its vastly superior scan time, spatial resolution and the recent advances which continue to reduce doses of ionising radiation towards safer levels [1]. These are important considerations in paediatric

applications when breath-holding and anaesthesiology related to MRI scans are unfavourable [39].

In the CFD sphere of literature there is no definitive argument that specifically excludes CTA or MRI as a favourable modality for geometry segmentation. In fact, in some studies, both are used to enhance a data set [38]. In a recent review of CFD studies, there was a preference for the use of PC-MRI as an imaging modality [36], however, in supplementing articles it can be seen that this is primarily driven by the "two-birds with one stone" ability of PC-MRI to extract geometry and flow data at the same time [11], [33], [36], [40]–[42]. It should be noted that three dimensional rotational angiography (3DRA), a comparatively young development, has been successfully used in some computational studies [43]. The benefit of this modality is how it may be conducted while the patient is undergoing a catheterisation procedure. This is beneficial in the reduction of conducting multiple x-rays, however, research incorporating this is not yet at the same volume as what the old and broadly implemented CTA and MRI modalities have experienced. Thus, although noteworthy, 3DRA is generally not included in a number of comparative literature publications and, in the case of RXH is yet to become available.

The final step in developing patient-specific geometries is through the segmentation of the region which is of interest. The choice of method in literature ranges from being completely manual through varying levels of automation [16], [28], [33], [44]. With the advent and popularisation of deep learning technologies, fully automated segmentation tools for specific anatomical structures are starting to see maturity although not on a broadly applied scale [45]. The presence of noise and the size of the object of interest can alter the choice of a segmentation modality [39]. Commercial and in-house software packages were often quoted for segmentation of the geometry and the most popular are summarised in Table 2-1.

Table 2-1: Commonly used medical image segmentation packages categorised by whether they can be obtained with or commercial licences

Open Source	**Commercial**
Vascular Modelling Toolkit [46]	VMTKLab
Insight Toolkit (Kitware) [47]	Simpleware
SimVascular (Stanford) [12]	Mimics
Horos [48]	OsiriX

2.2.1.2 ***Patient-Specific Velocity Data Acquisition***

In aortic flow modelling, it is typical to place an outlet patch at each of the supra-aortic vessels and the descending aorta prior to any bifurcations and an inlet patch at the ascending aorta [11], [49]–[51]. To adequately impose and tune different boundary conditions, it is important to know the time dependent pressure and/or velocity waveforms at these boundary patches as well as points within the domain [43]. PC-MRI and doppler ultrasound echocardiography are the leading modalities for velocity data acquisition. Echocardiography has been described predominantly as a complimentary modality for CTA to add flow data to the acquired geometry data [37]. However, in contrast to PC-MRI, echo experiences limitations stemming from the dependency on adequate acoustic windows, the steadiness of the patient and the angle of the probe axis relative to the direction of flow.

In considering the capabilities of either modality, PC-MRI has been shown favour by the CFD community proven by the volume of projects which utilise the methodology in some way [9], [11], [16], [36], [52]. However, echo cannot be said to be redundant. In low and lower-middle income country settings especially, it is justified by being a cheap and portable point of care which is accessible in a majority of institutions. This contrasts with the specialised, advanced and expensive PC-MRI facility [53]. Where the ability to measure flow non-invasively exists, techniques for non-invasive pressure measurements are yet to be developed.

2.2.1.3 ***Patient-Specific Pressure Field Data Acquisitions***

It is widely agreed that the gold standard for central pressure measurements is through an invasive catheterisation procedure [51]. Pressure measurements are especially important in the tuning of lumped parameter boundary conditions which research is converging towards agreeing upon as the best for approximating physiological responses at the outlets [33], [44]. However, a catheter procedure carries a risk to the patient and is broadly being aimed to be replaced by non-invasive technologies with several mathematical models, including CFD, being proposed.

Echocardiography uses a modified Bernoulli's equation to calculate pressure drops based on the measured velocity but has been shown to overestimate the result [54], [55]. Pressure mapping using the flow field derived from 4D phase contrasted MRI scans and the pressure Poisson equation have been proposed as an improvement in calculating CoA pressure drops [51] but has been found to underestimate these values [55]. It is broadly opined that on adequate maturation and development, CFD methods based on flow data alone will ultimately lead to the replacement of catheterisation in CoA patients [56]. These are three examples that are not necessarily exhaustive nor are they intended to generate a sombre outlook on non-invasive pressure measurement techniques, however, at this stage, robust validation of CFD

tools will depend on accurate, absolute pressure measurements [16]. Alternatively a toolchain may instead attempt to make assumptions and derivations to accurately predict pressure from available velocity fields but the risk of oversimplification should always be a consideration in these cases [51], [57].

2.2.2 Cardiovascular CFD Boundary Conditions

Boundary conditions are mandatory in numerical simulations to describe flow at the inlets, outlets and bounding wall of the vessel domain. In larger vessels the BC is required to, in various ways, account for the effect of downstream vasculature which is not included in the computational domain [58]. BCs effectively constrain the problem in such a way as to produce a unique solution and, importantly, form the intersection between the computational model and clinical reality. The accuracy of the solution has been shown to be sensitive to the choice of BCs [33] which has led to a significant proportion of global research working to develop or appropriately implement a wide variety of BCs in haemodynamic studies [34], [35], [39], [59].

Each boundary condition may vary in complexity from either an implementation perspective or from the specific dataset that is required to define them. The discussion surrounding inlet and outlet BCs primarily focusses on the impact that each BC has on a solution accuracy, be it from a qualitative or quantitative perspective [33], [34], [59]. The most popular inlet and outlet BCs from literature are shown in Figure 2-3 along with an indication of their relative complexity.

Typically a no slip, rigid wall condition at vessel walls has been broadly applied in literature but it is worth mentioning that some research contests the validity of this assumption using fluid-solid interaction (FSI) models [60], [61]. However, developing a tool for clinical application may necessitate a compromise between computational efficiency and result accuracy. Thus, it is important to take the various arguments into account to be able to make decisions for which the consequence on accuracy is accounted for.

2.2.2.1 ***Inlet Boundary Conditions***

It is generally accepted that the prescription of velocities at the inlet boundary of the ascending aorta, be it steady or pulsatile, is adequate in haemodynamic simulations [59], [62]. This is especially shown in a 2013 global collaborative research challenge to conduct a CFD study of a patient-specific aneurysm case. As a result, a broad spectrum of techniques could be seen in most aspects except the inlet boundary conditions where all twenty-seven participants specified velocity at the inlet instead of pressure. The only division was how the velocity profile was idealised with 15/27 participants using a fully developed, parabolic velocity profile and 12/27 used plug profiles [63].

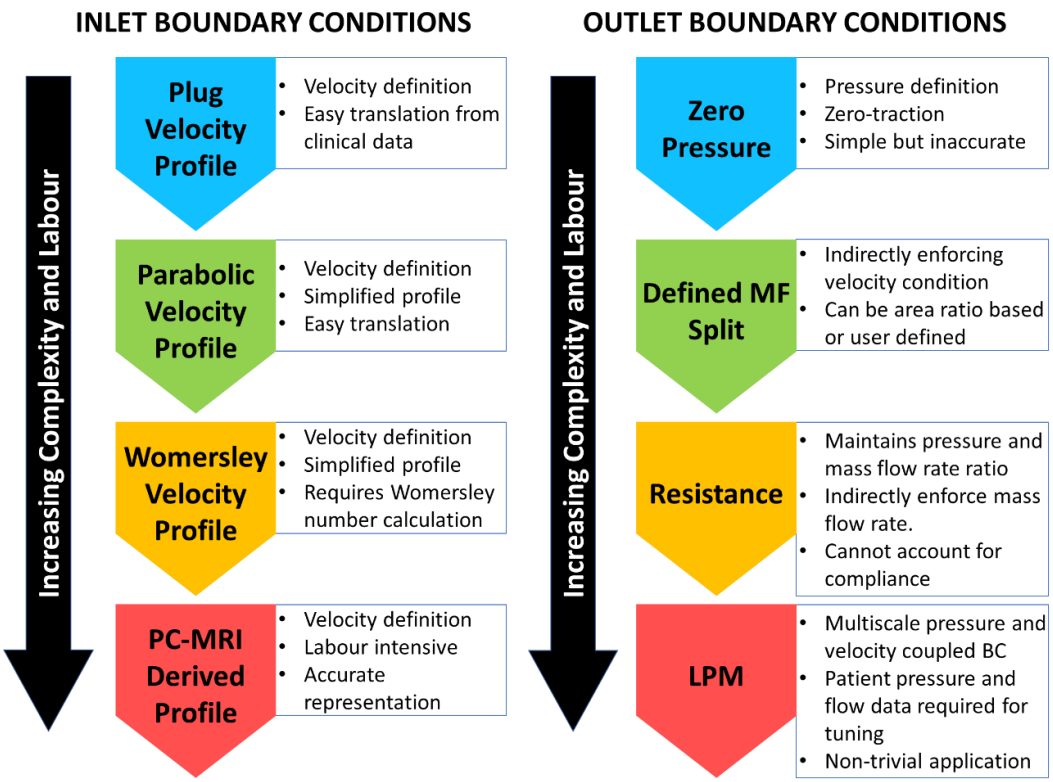

Figure 2-3: Summary of most popular boundary conditions for inlets and outlets in patient-specific computational fluid dynamics models. LPM = Lumped Parameter Model, MF = Mass Flow.

The approach to the idealisation of a velocity profile for a given mass flow (be it transient or steady) has been found to be an important consideration in designing a numerical model [59]. Alternatives to a simple plug velocity profile are suggested to be fully developed parabolic profiles, Womersley flow or PC-MRI defined flow profiles [35], [59], [64]–[66]. The choice of idealisation, however, has been shown to impact the model. In fact, Madhavan *et al.* shows that the variation in haemodynamic values is significant up to two inlet diameters distal to the inlet patch [65]. McElroy *et al.* supports this through a comparison of TAWSS and OSI using a plug and fully developed inlet flow profile. This study found that significant quantitative and qualitative differences in TAWSS and OSI distributions existed but primarily in the ascending aorta only [66]. This suggests that, in a coarctation of the aorta case, the velocity profile at the inlet could be idealised to be a plug flow due to the region of interest primarily being at the coarctation site.

In general, as the inlet boundary condition is simplified, it is understandable that the effects of the sudden opening and closing of the aortic valve (especially in the case of diseased valves) is lost. Morbiducci *et al.* tests an idealised and PC-MRI derived velocity profile and stresses the impact that simplifying assumptions have on bulk fluid flow properties such as helicity, TAWSS and OSI. In this case, significant differences throughout the domain are shown to

exist [59]. This is further supported by Goubergrits *et al.* who shows both visually and quantitatively that simplified BCs neglect clearly significant flow features [56].

In considering these differences, the choice of inlet boundary condition should be made while remaining aware of the impact that these assumptions may have on the bulk fluid flow. Ultimately, the choice will first rely on the data that is available to define the boundary conditions due to the modality being used.

2.2.2.2 ***Outlet Boundary Conditions***

The outlet boundary conditions are crucial in driving the final solution of the flow field. Thus, the choice of outlet boundary condition is an important one, especially in cases where the fluid domain has multiple outlets [44]. Zero-pressure, area ratio defined mass flow splits, PC-MRI defined mass flow rates and lumped parameter models are popular outlet boundary conditions that vary in complexity and accuracy as well as in their application.

The variability that can be seen in the choice of boundary conditions for studies could be a result of the focus and intended complexity of the research as well as which clinical data was available to the engineers. It has been shown that, although simple to implement, a zero pressure outlet is inadequate for replicating physiological pressure and flow metrics [35], [44]. In both transient and steady state simulations, PC-MRI based definitions of velocities at the outlets have been shown to adequately replicate *in-vivo* measured velocity [35] and catheter based pressure gradient measurements across a coarctation [55]. However, the labour in processing the data that is required for this method in addition to the challenges of synchronising data taken at difference points in time can render this method impractical [34]. Vignon-Clemental *et al.* highlights the paradox in using pre-intervention outlet boundary conditions in modelling intervention and surgical repairs as these boundary conditions would also be affected by the new state of geometry as a result of a repair [67].

The three-element Windkessel model (3EWM) shown in Figure 2-4 is an electrical circuit analogy which uses a combination of 0D resistors and capacitors to approximate the resistance and compliance effect of downstream vasculature. Purely resistive models have been used too, but 3EWM has become the leading choice in outlet boundary condition [16], [27], [29], [52], [68]. In a study by Pirola *et al.* [33] it was found that the 3EWM outlet boundary condition outperformed simplified BCs such as area ratio defined mass flow rate splits and zero-pressure [33]. The sentiment for the superior nature of 3EWM as an outlet boundary condition is reiterated in further studies [34], [44], [58].

It is important to note that implementing a 3EWM outlet boundary condition requires patient-specific velocity and pressure data at each outlet in order to calculate appropriate resistance and capacitance values, which is often a limiting factor for studies. This could be especially pertinent in country healthcare facilities who may not routinely conduct PC-MRI and catheter procedures for CoA leaving the derivation of the 3EWM parameters to be a challenge. It should be noted that a technique has been proposed by Romarowski *et al.* to deal with incomplete datasets but this has yet to be implemented broadly [38]. Although echocardiography is a feasible modality in countries with otherwise limited resources, there is a stark lack of research which persists with implementing the doppler ultrasound derived velocity data as boundary conditions.

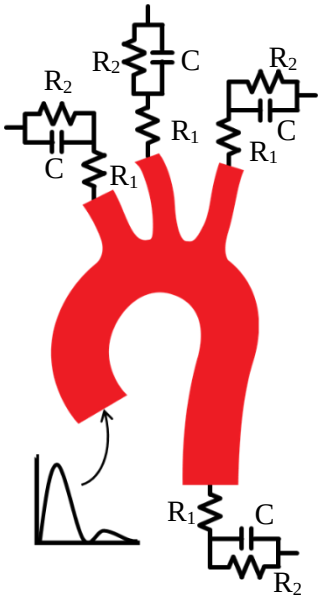

Figure 2-4: Schematic showing the typical three element Windkessel model for each outlet in an example aorta schematic. R_1 = Proximal resistance, R_2 = Distal vasculature resistance, C = Distal vasculature compliance

2.2.2.3 ***Wall Boundary Conditions***

The vessel wall is commonly treated in one of two manners; either as a rigid wall or as a deformable solid using FSI principals [40]. In either case, the boundary condition that represents the interaction at the contact point between the fluid and solid domain is commonly prescribed using a no slip condition which forces the fluid velocity layer directly adjacent to the wall to be zero.

The decision to implement FSI instead of rigid wall assumptions is debated in literature. The debate centres around the value add to the accuracy of the results considering the significant increase in computational demand [9]. An in-depth review of this consideration is conducted by Brown *et al.*, which indicates the computational time between a rigid and deformable wall assumption in an aortic study as being 6.6 and 145 hours respectively. In a clinical application, the former is far more favourable especially because it was found that values relevant for

diagnosis such as pressure were comparable [60]. However, it was found by Jin *et al.* that the compliance of the aorta, in addition its curvature, contributes to helical flow features which may be under-emphasised under rigid wall assumptions [42].

From a developmental perspective it is important to recognise that the implementation of FSI is non-trivial. Thus, the previous considerations as to data-collection, image processing and boundary condition definition should be first call for development and validation prior to the added complexity and time required to develop an accurate FSI model.

2.2.3 Coarctation of the Aorta Simulation Results

The bulk of CFD studies of haemodynamics in CoA focusses on the analysis of velocity, pressure and wall shear stress and their derivative metrics such as time averaged wall shear stress, oscillatory shear index, mass flow rate, helicity and pressure gradients. The nature of patient-specific CFD studies inherently nullifies the direct comparison of results between different studies. However, in most cases there are general expected flow features such as helicity, which may occur as a consequence of the aortic arch. Thus, the intention of this section of the review is not to give benchmark data metrics for validation but rather to build an expectation of order of magnitude as well as features of results that would be able to confirm how realistic the study's results are.

Studies by Goubergrits *et al.* and Pirola *et al.* provide insight into the expected flow regimes in a coarctation case [11], [33]. In a simulation of a coarctation with a plug flow inlet velocity profile by Goubergrits *et al.* [11], the peak systolic velocity values were found to be in excess of $1\ m.s^{-1}$. The nature of patient-specific data measurements is such that data collected across patients cannot be directly compared or set as any baseline standard. However, the value in evaluating studies such as these would be to prime the researcher with an expectation that could be useful for sanity checking results and providing an expectation for order of magnitude of velocities in these patients. In this same study, it was interesting to note how the streamline visualization of the flow field showed a low helicity in the ascending aorta and aortic arch but, distal to the coarctation zone, two distinct flow features were present. The first was a high velocity jet through the coarctation and the second, a tortuous helicity throughout the descending aorta adjacent to the jet. Cosentino *et al.* as well as Pirola *et al.* quantify the percentage mass flow split across each outlet patch for a variety of tested outlet boundary conditions. It is found in these instances that the descending aorta, in healthy or repaired aortas accommodates $70-80\%$ of the total outlet mass flow rate respectively [33], [52].

Of the body of literature reviewed on CoA CFD, the studies by Rinaudo *et al.* and Goubergrits *et al.* [28], [55] are examples which focus on pressure analyses. In these studies, the pressure gradients were calculated for several degrees of stenosis. Goubergrits *et al.* expressed pressure

gradients which ranged from $10\ mmHg - 25\ mmHg$ for stenosis ratios that ranged from $24.3\ \%$ to $92.0\ \%$. However, Rinaudo *et al.* calculated pressure gradients in excess of $40\ mmHg$. In both cases these values correlated closely to catheter derived pressure gradients. Although these results are not directly pertinent in any other case, they give expectation for the range of pressure gradients which may exist.

In general, WSS is measured through transient analyses and the time-average value calculated. Due to the contribution by the low flow rates during early systolic acceleration, late systolic deceleration and diastole, this value may be as low a $4 - 14\ Pa$ [28], [33], [65] or as high as $50\ Pa$ [24]. However, results from a study by Olivieri *et al.* gives evidence to suggest that the maximum WSS at peak systolic flow may exceed $100\ Pa$. In the same study it was also interesting to note the predominance of zero WSS values over the surface [69]. The existence of these significantly higher peak WSS values are postulated as being relevant, despite only existing for a fraction of the cardiac cycle. This is due to the proportional relationship between the risk of developing atherosclerosis and the WSS that the endothelial cells in the vessel wall are subjected to [23].

This literature review has aimed to give an overview of the current methodologies that are being employed in patient-specific haemodynamic computational modelling in the context of the background to coarctation of the aorta and congenital heart disease itself. There are several approaches to carrying out each phase of such a computational pipeline and focus was given to those which were used in data acquisition, image segmentation, boundary conditions and result analysis. The implications that each method has on accuracy and implementation were highlighted and evaluated based on the larger goal of being used within resource constrained healthcare facilities.

3. THEORETICAL APPROACH

In this study each constituent of the toolchain from data acquisition, through data processing and, finally, numerical simulation, has its own theoretical background. Thus, this chapter aims to give a brief overview of the theory which underpins the key components of the pipeline to give context to the experimental methodology.

3.1 PATIENT-SPECIFIC DATA ACQUISITION MODALITIES

Clinicians inform their diagnostic and intervention decisions based on velocity, pressure and geometry information that is obtained through various imaging and measurement modalities. Each of these modalities will have associated advantages and disadvantages that make it applicable and or advantageous in different cases.

3.1.1 Doppler Echocardiography

Echocardiography is a high-resolution ultrasound imaging technique that provides geometry data in either 2D or 3D. By nature of the propagation and reflection of soundwaves through air and bone, an echocardiographic investigation is limited to regions known as acoustic windows where the signal is able to propagate adequately without interference from bones or air in the lungs. These acoustic windows are important to consider when planning which measurements are to be taken.

An adaptation of standard echocardiography is to leverage the doppler effect caused by the interaction between a moving blood cell and the emitted soundwave to measure the flow velocity. This adaptation of the technology is referred to as doppler echocardiography and is widely used in cardiovascular medicine.

Doppler echocardiography can estimate a pressure drop based on the measured velocity data through the modified Bernoulli equation shown in Eq 3.1 below.

Eq 3.1. $$\Delta P = K v_{max}^2$$

Where K is typically set to 4 [70].

While this can be useful, the simplification has been shown to have varying degrees of success with regards to accuracy. In general, the measurement has been shown to overestimate the pressure gradient in coarctation of the aorta [54] and so other modalities for pressure measurement are preferred to be used in this case.

3.1.2 Catheterisation

The gold standard for measuring pressures in the cardiovascular system remains catheterisation [71]. Catheterisation is a flexible modality that is capable of measuring blood pressure at a majority of locations along the aorta and other major branch vessels and veins, depending on the entry site. This is particularly useful in the assessment of the CoA pressure gradient. As reliable and versatile as the measurements are, the inherent risk in the procedure stems from the radiation required to monitor the location of the catheter, possibility of infection, vessel puncture and effects of anaesthetics.

3.1.3 Computed Tomography Angiography

The fundamental premise of CTA is the measure of the difference between the emitted and detected intensities of ionising x-rays after passing through a subject. The rotation of a CTA emitter and detector provides detail of the subject which is displayed in a 2D slice as opposed to the 1D projection of an x-ray. As the emitter and detector move axially along the subject, multiple 2D slices constitute a complete 3D dataset [72].

In cardiovascular disease the volume of blood flowing in a specific vessel is commonly referred to as the blood pool. To highlight the blood pool in the CTA scan, a radiopaque dye is injected into the bloodstream to increase the absorption of the energy as the x-ray is increased. This process aids the segmentation of the vessel geometry.

3.1.4 Magnetic Resonance Imaging

When a patient is subjected to a uniform magnetic field, molecules in the body align with this field. Radio waves are then applied to excite the molecules away from this aligned state and the consequent electromagnetic wave which is generated can be interpreted to provide information of the location of the particle as well as differentiate between the tissue to which it belongs. In a similar sense to CTA, MRI produces axial slices along the patient to generate a 3D space of information regarding geometry of different tissue structures.

In cardiovascular applications where a region of blood flow is of interest, the addition of a phase contrasting agent allows an MRI scan to elucidate time-average velocity fields and time-varying velocity fields in addition to the geometric information of the vessel. However, the spatial resolution is inferior when compared to CTA and as a result may not be sufficient to capture the detail of relatively small vessels in young and infant patients [73]. Due to the lack of ionising radiation, the scan can be conducted repeatedly at numerous points during the cardiac cycle to generate a cine-image to provide actual flow data of the blood over the cardiac cycle [11].

3.2 DICOM IMAGES AND THRESHOLDING

A DICOM (Digital Imaging and Communications in Medicine) image presents an image through an array of voxels which, for different structures, carry different grayscale values. What is unique about a DICOM image is that there is metadata about the patient (if not anonymised), the properties of the scan itself and the dimensions of the voxels amongst others.

The dimension data of the pixels is especially useful so that the image may be a tool for the measurement of different objects in the image. In segmentation, the intensity (or grayscale value) of the pixel of an object can be used to delineate that object from the surrounding structures such as the blood in a vessel otherwise referred to as the blood pool [74]. Thresholding is a simple method of segmentation which refers to the differentiation of different structures based on their relevant pixel intensity.

The DICOM image can be mathematically represented as a 2D array of 1D grayscale values. The concept of thresholding is in effect a binarization of grayscale values in the image. Fundamentally any pixels (or entries in the image array) that have a grey scale value within a specified range are assigned a 1 and those pixels outside of the specified range, a zero [75]. This is shown graphically using a simple phantom in Figure 3-1 which segments the crescent moon shape with a pixel grayscale value of 250.

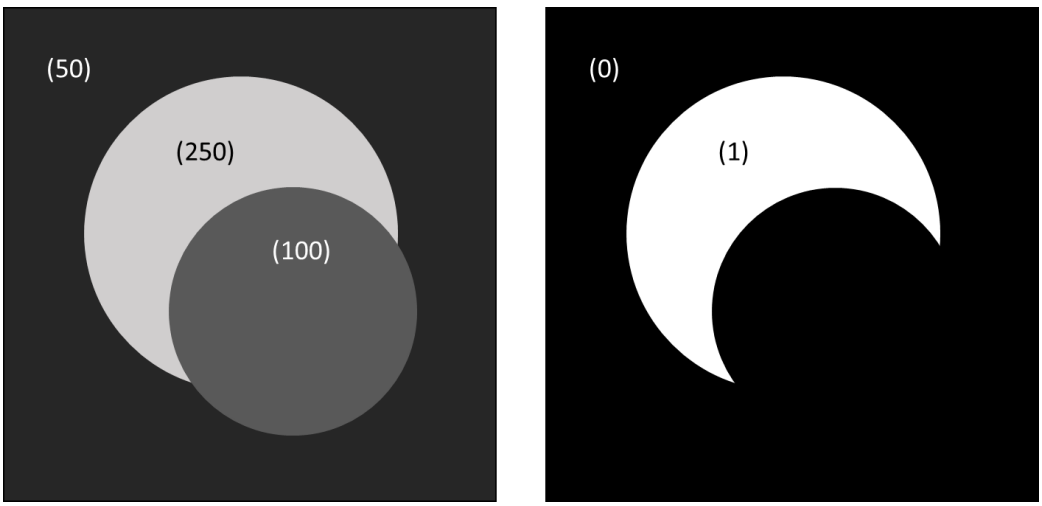

Figure 3-1: Simplified image which has a region divided into a background, circle and crescent moon shape identified by different grayscale values 50, 100 and 250 respectively.

3.3 VOLUME DISCRETISATION

In organic geometries such as blood vessels, an unstructured hybrid volume discretisation (or meshing) approach is favourable to adequately capture the geometry as well as to calculate the complex flow detail resulting from the irregular geometry. As can be seen from Figure 3-2 there are intricate details which a discretisation method needs to be able to capture while maintaining mesh quality. There are many approaches to discretising a volume, however, the importance of a good quality mesh cannot be stressed enough as it has a direct impact on the outcome of the numerical approach. A poor-quality mesh is certain to lead to corrupted results and should be avoided. In light of this, the advantages and disadvantages of each cell type as well as the overall mesh quality metrics should be considered [76].

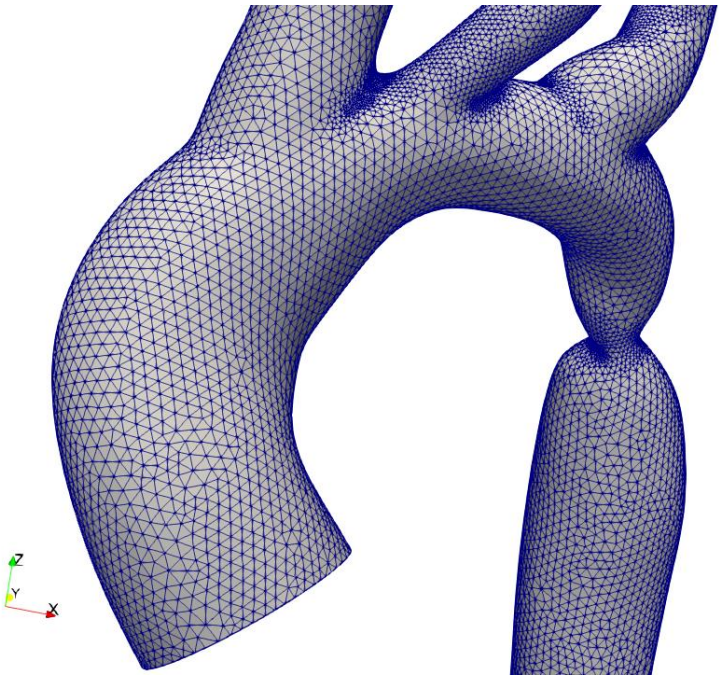

Figure 3-2: An example of a discretised aorta model to illustrate the discretisation of an organic shape and particularly the need to use an approach that is able to capture the detail in areas of high curvature such as the branch and stenosis sites.

3.3.1 Mesh Quality Metrics

The overall mesh quality is judged on the skewness, non-orthogonality and aspect-ratios of the cells. An orthogonal and good aspect ratio mesh is shown in Figure 3-3 (A) and an example of cell skewness and non-orthogonality is shown in Figure 3-3 (B). Cell skewness refers to the distance between the midpoint of the interfacing cell face and the point of intersection of the line AB. Non-orthogonality is a measure of the angle which the line joining two centroids of the adjacent cells makes with the normal of the face between these two cells [77]. The aspect ratio of a cell is measured by ANSYS Fluent as the maximum ratio between the distance from the cell centroid to the face centroids and the cell centroid and the nodes of the cell as shown in Figure 3-3 (C) [78].

In a perfect mesh the non-orthogonality metric should approach 0^o (i.e. an orthogonal mesh), the cell skewness after normalisation should range between 0 and 1 with 0 being the target and 1 being a degenerate cell [78]. Finally, the value of the aspect ratio of cells should be considered within the cells' context. For example, the boundary layer of cells requires that the cells are thin which inherently leads to a worse aspect ratio but is necessary to capture the flow near the wall.

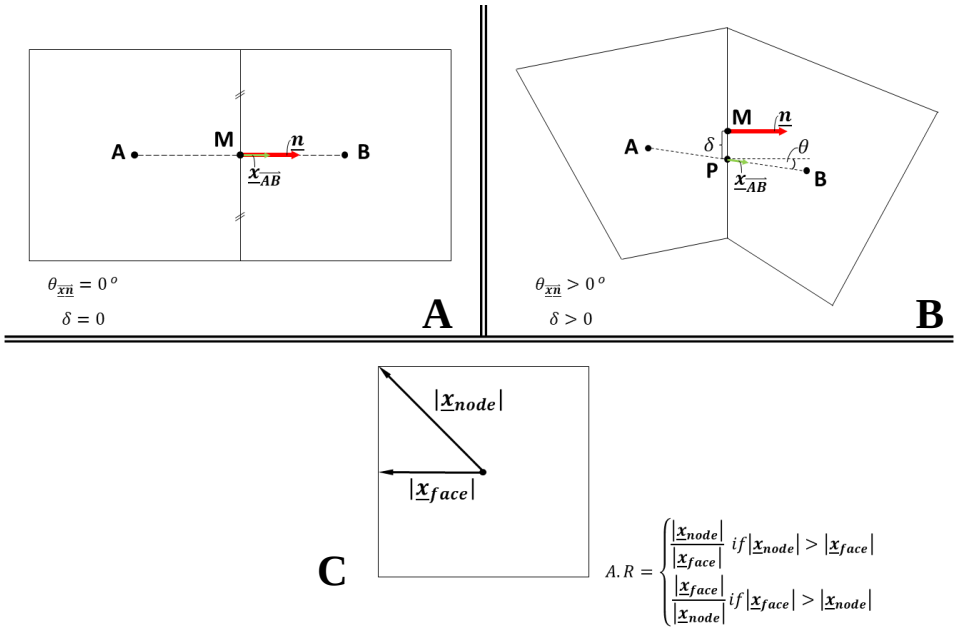

Figure 3-3: (A): Two cells which are perfectly orthogonal and not skew. (B): Two cells which are non-orthogonal and skew. A and B indicate the centroids of the cells, M indicates the midpoint of the shared face, P indicates the intersection point with the shared face by the line joining A and B. θ and δ indicate the non-orthogonality and skewness respectively. (C): metrics used for aspect ratio measurement in ANSYS Fluent

3.3.2 Cell Geometry

In geometries that are organic, tetrahedral cells are beneficial for the bulk of the mesh volume but, especially when wall shear stress is a relevant haemodynamic feature, it is important to include a boundary layer of thin prismatic cells. A boundary layer of triangular prism cells and a schematic of a tetrahedral cell is shown in Figure 3-4. A cell size in general is bound by defined maximum and minimum lengths. The additional parameters to define the triangular prism boundary layers are the number of boundary layers, the total height of the boundary layer and the growth rate from layer to layer.

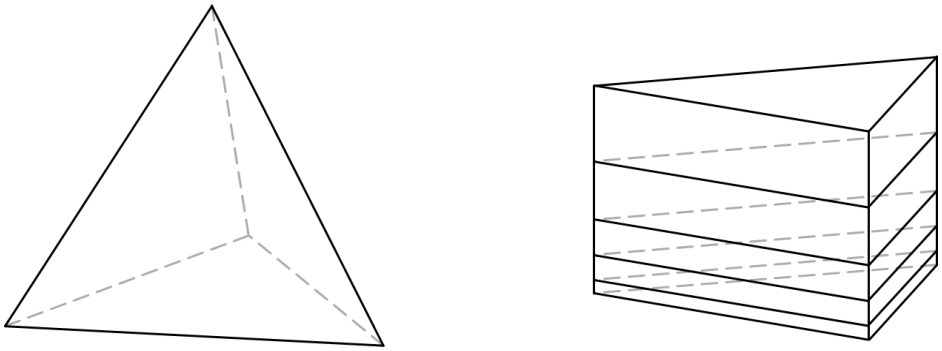

TETRAHEDRAL CELL BOUNDARY LAYER PRISM CELL

Figure 3-4: Schematics of a tetrahedral and five stacked prism cells. The prism cells have been shown in the configuration that they may be in as part of a boundary layer with a growth ratio increasing the thickness of the cell.

3.4 FUNDAMENTAL PRINCIPLES OF COMPUTATIONAL FLUID DYNAMICS

3.4.1 Computational Fluid Dynamics

Computational fluid dynamics and specifically the finite volume method (FVM) are numerical approaches to solving the Navier-Stokes equations to obtain velocity and pressure fields of fluid flow as it interacts with objects and boundaries in a given domain. Although fundamentally being an approximation, this numerical approach is especially important when analysing complex cases for which analytical solutions are difficult or impossible to find such as in patient-specific blood flows.

Regardless of the application, CFD is founded on the Navier-Stokes equations for continuity and conservation of momentum. To gain a good understanding of the foundation for these equations, one must understand the two spatial frames of reference used in the FVM after which the key mathematical theorems used to derive the continuous governing equations of fluid flow will be addressed. These can then be used as the foundation for describing the process of obtaining the discretised governing equations used in the finite volume method as well as the solving algorithms.

3.4.2 Reference Frames:

When subjected to shear, no matter how small, a fluid will respond by continuously deforming. The reference frame used for deriving governing equations for fluid deformation thus becomes an important consideration. This consideration is between an Eulerian or Lagrangian frame of reference.

3.4.2.1 ***Eulerian Frame of Reference:***

An Eulerian frame of reference is one that considers a control volume that is fixed in space and the properties of fluid flow are analysed in this space as they are transported by flow in and out of the control volume over time. That is to say that the spatial and temporal variables are considered as independent of the fluid particle being analysed and that a fluid property $\boldsymbol{\phi}$ can be expressed as:

$$\phi = \phi(\underline{\boldsymbol{x}}, t)$$

Where:

$$\underline{\boldsymbol{x}} = (x, y, z)$$

and (x, y, z) are the chosen spatial coordinates in the reference frame and t is the time.

3.4.2.2 ***Lagrangian Frame of Reference:***

The Lagrangian reference frame considers a control volume of the fluid which is not fixed in space and moves with the fluid flow. Thus, the property being analysed is linked to the control volume as it moves and deforms with the fluid. Thus, a fluid property can be defined as:

$$\phi = \phi(\underline{\boldsymbol{X}}, t)$$

Where:

$$\underline{\boldsymbol{X}} = (X, Y, Z)$$

(X, Y, Z) describes the reference position of a particular volume of fluid at time, t.

Both the Lagrangian and Eulerian frames of reference are important in the derivation of the governing equations of fluid flow. This is because the way in which a control volume is defined in the Lagrangian configuration allows the Navier-Stokes equations to be easily derived. However, because a finite volume mesh is inherently an Eulerian reference frame, the governing equations need to be converted to be expressed in this configuration so that the finite volume method can be applied. Reynold's Transport Theorem is this link between the Lagrangian and Eulerian reference frame.

3.4.3 Reynolds' Transport Theorem:

Reynolds' Transport Theorem expresses the Lagrangian derivative of a scalar property ϕ with respect to time in terms of the Eulerian or reference configuration. To do this, consider the arbitrary volume in Figure 3-5

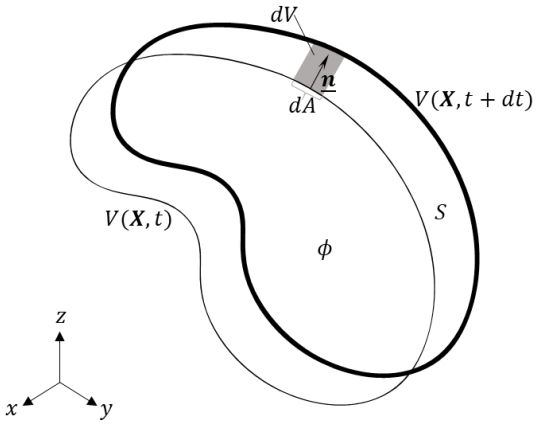

Figure 3-5: Control volume at time t and t + dt

At a given time, t, the total ϕ, that is contained in the control volume is

Eq 3.2. $$\Phi = \int_{V(t)} \phi dV$$

Where $\phi(\boldsymbol{x}, t) = \phi(x, y, z, t)$

The temporal derivative of ϕ in the Lagrangian configuration can be analysed from a differential approach by expressing it as

Eq 3.3. $$\frac{D}{Dt}\int_{V(t)}\phi dV = \lim_{\delta t\to 0}\left[\frac{1}{\delta t}\left\{\int_{V(t+\delta t)}\phi(\boldsymbol{x},t+\delta t)dV - \int_{V(t)}\phi(\boldsymbol{x},t)dV\right\}\right]$$

With this as a starting point and through a series of manipulations, the weak and strong form of RTT is obtained in Eq 3.4 and Eq 3.5 respectively

Eq 3.4. $$\frac{D}{Dt}\int_{V(t)}\phi\, dV = \int_{V(t)}\frac{\partial\phi(\boldsymbol{x},t)}{\partial t} + \boldsymbol{\nabla}\cdot(\phi\boldsymbol{u})\, dV$$

Eq 3.5. $$\frac{D\phi}{Dt} = \frac{\partial\phi(\boldsymbol{x},t)}{\partial t} + \boldsymbol{\nabla}\cdot(\phi\boldsymbol{u})$$

The terms on the right-hand side of Eq 3.5 can be interpreted as:

$\frac{\partial\phi(\boldsymbol{x},t)}{\partial t}$ The temporal derivative of the value ϕ in the Eulerian reference configuration

$\boldsymbol{\nabla}\cdot(\phi\boldsymbol{u})$ The divergence of the product of the scalar value ϕ and the velocity represents the convection of ϕ as a result of the flow of the fluid

3.4.4 Governing Equations of Fluid Flow:

The Navier-Stokes equations are derived from the fundamental principles of conservation of mass (continuity) and momentum. These constitute the governing equations of fluid flow and for interest, are fully derived in Appendix 1.

To give a spatial context for the discussion of the governing equations which follows, it is helpful to visualise the arbitrary, Lagrangian control volume, V, in Figure 3-6.

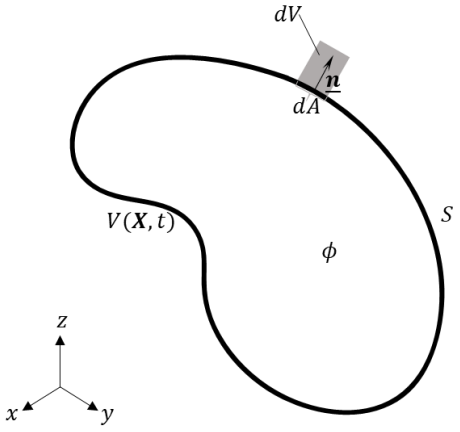

Figure 3-6: Arbitrary control volume in the Lagrangian reference frame

3.4.5 Conservation of Mass (Continuity)

If one considers V in Figure 3-6, it is necessary that, although the shape of the volume may deform and move, the mass contained within the volume remains constant and can be calculated by

Eq 3.6. $$m = \int_V \rho dV$$

Conservation of mass dictates that this quantity does not change over time and so it follows that the material derivative of the mass is zero. In conjunction with Reynolds' Transport Theorem, the weak form of the conservation of mass is given as

Eq 3.7. $$\frac{D}{Dt}\int_V \rho dV = \int_{V(t)} \frac{\partial \rho}{\partial t} + \nabla \cdot (\rho \boldsymbol{u}) dV = 0$$

By the fact that V is arbitrary and the fluid incompressible the integral in Eq 3.7 can be dropped and the integrand simplifies to what is known as the continuity equation

Eq 3.8. $$\boldsymbol{\nabla} \cdot \boldsymbol{u} = 0$$

In other words, Eq 3.8 says that, the conservation of mass for an incompressible equation requires that the divergence of the velocity field is zero.

3.4.6 Conservation of Momentum

The conservation of momentum is based on Newton's second law of motion which states that the rate of change of momentum of an arbitrary control volume of fluid such as in Figure 3-6, is equal to the total force acting on that control volume.

Consider that the momentum of an arbitrary element of fluid is the product of the mass of the control volume and its velocity and that the total force acting on V as a result of body (usually gravity, or $\boldsymbol{g}$) and surface forces (i.e. pressure, stress and shear, or, in total, $\boldsymbol{\tau}$). Newton's Second Law for momentum is expressed as

Eq 3.9. $$\int_V \frac{D}{Dt}(\rho \boldsymbol{u}) dV = \int_V \rho \boldsymbol{g} + \boldsymbol{\nabla} \cdot \boldsymbol{\tau} dV$$

In most cases the primary forces acting on a control volume is pressure and viscous forces. Eq 3.9 expresses the weak form of the problem, but by making the appropriate substitutions, considering the arbitrariness of V and assuming a Newtonian fluid (where viscosity is independent of shear rate), the strong form can be extracted

Eq 3.10. $$\frac{\partial}{\partial t}(\rho \boldsymbol{u}) = -\boldsymbol{\nabla} P - \boldsymbol{\nabla} \cdot \left((\rho \boldsymbol{u}) \otimes \boldsymbol{u}\right) + \mu \boldsymbol{\nabla}^2 \boldsymbol{u} + \rho \boldsymbol{g}$$

In summation the terms of the conservation of momentum equation in Eq 3.10 represents:

$\frac{\partial}{\partial t}(\rho \boldsymbol{u})$: The rate of change of momentum per unit volume in the Eulerian reference frame. In the case of steady state problems this term is neglected and set to zero.

$-\boldsymbol{\nabla} P$: The gradient of the pressure field in the Eulerian frame of reference. The negative of this term can intuitively be understood by the fact that an element of fluid flows from a high to low region of pressure and thus will have an increase in momentum as it flows in the direction of a negative pressure gradient

$\mu \boldsymbol{\nabla}^2 \boldsymbol{u}$: The diffusive term. This describes the change in momentum of the fluid within the Eulerian control volume due to the viscous effect of the flow of surrounding fluid elements. In effect the momentum increases or decreases within a fluid element due to the diffusion of momentum from or to other neighbouring elements.

$-\boldsymbol{\nabla} \cdot \left((\rho \boldsymbol{u}) \otimes \boldsymbol{u}\right)$: Commonly referred to as the convective term, this term describes the transport of momentum through an Eulerian reference frame control volume due to the velocity of the fluid flow itself.

$\rho \boldsymbol{g}$: This is the contribution to the increase of momentum due to a body force which acts on the fluid which, in the case of gravity, is in the direction in which gravity acts relative to the orientation of the system. In cardiovascular CFD this is often neglected

3.5 THE FINITE VOLUME METHOD

The finite volume method refers to the numerical approach towards solving the weak form of the Navier-Stokes equations through spatially discretising them and iteratively solving for pressure and velocity which are implicitly linked. The FVM can be generally described by three steps:

1. Generate the mesh by discretising the domain into discrete control volumes
2. Integrate the governing equations over each control volume (i.e. find the weak form) so that the discrete form of the governing equations can be found
3. Iteratively solve the spatially discretised governing equations over each finite volume in the numerical mesh.

The methodology of step 2 is vital for the finite volume method. There are several schemes of varying orders of accuracy and so the fundamental principle behind the discretisation of each term in the governing equation will be described along with the defining variation of the scheme that is applied in the methodology used for this study.

3.5.1 Discretisation of the Governing Equations

For the purpose of describing the underlying principles of discretising the governing equations, each term will be considered on a 2D structured cell with notation as shown in Figure 3-7. Note that the cell is chosen for analysis but is surrounded by similar cells.

For each derivation only the x-component of Navier-Stokes equations for an incompressible, Newtonian fluid is considered as the method translates easily to the other components.

Eq 3.11. $$\boldsymbol{\nabla} \cdot u = \frac{\partial u_x}{\partial x} + \frac{\partial u_y}{\partial y}$$

Eq 3.12. $$\frac{\partial}{\partial t}(\rho u_x) + \boldsymbol{\nabla} P + \boldsymbol{\nabla} \cdot (\rho u_x \boldsymbol{u}) - \mu \boldsymbol{\nabla}^2 u_x = 0$$

A common term which will be required is what is referred to as the edge coefficient (Eq 3.13), or, in other words, the outward pointing area vector of each face of the cell which is defined as

Eq 3.13. $$c|_f = (A\boldsymbol{n})|_f$$

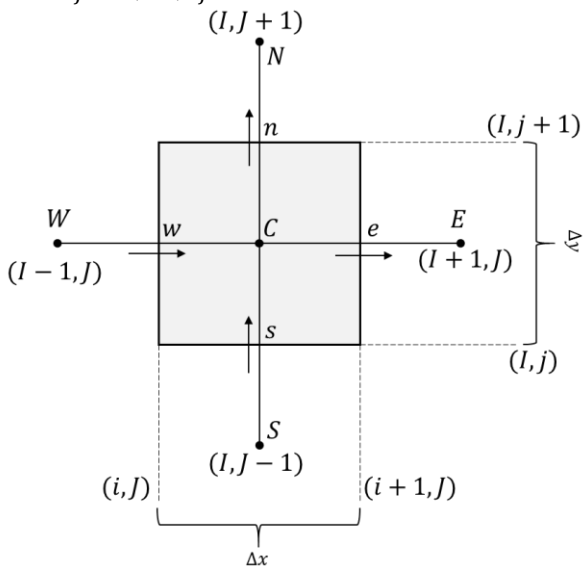

Figure 3-7: A single structured finite volume vertex centred cell with centre vertex, C, neighbouring cell vertices E, N, W, S and cell faces e, n, w, s. Flow in the x and y direction is indicated by arrows at the faces.

3.5.1.1 ***Convective Term Discretisation***

The strong form of the convective term is first approximated by its weak form which, because of the divergence theorem can be calculated by summing the dot product of the $\rho u_x \boldsymbol{u}$ and the edge coefficient, $c|_f$ (as described in Eq 3.13) on each face.

Thus

Eq 3.14. $$\boldsymbol{\nabla} \cdot (\rho u_x \boldsymbol{u})|_{I,J} \approx \frac{1}{V_{I,J}} \int_{V_{I,J}} \boldsymbol{\nabla} \cdot (\rho u_x \boldsymbol{u})|_{I,J} dV = \frac{1}{V_{I,J}} \sum_{f \in A_{I,J}} \rho u_{x_{\boldsymbol{up}}} \boldsymbol{u} \cdot \boldsymbol{c}|_{\boldsymbol{f}}$$

In Eq 3.14, the velocity vector at each face of the cell is obtained through first order upwinding which is a linear interpolation between the velocities of the nodes adjacent to the face being examined. The value of $u_{x_{up}}$ in first order upwinding is defined by

$$u_{x_{up}} = \begin{cases} \boldsymbol{u}_{\boldsymbol{x_{I+1,J}}} \; if \; \boldsymbol{u} \cdot \boldsymbol{c}|_f \geq 0 \\ \boldsymbol{u}_{\boldsymbol{x_{I,J}}} \; if \; \boldsymbol{u} \cdot \boldsymbol{c}|_f < 0 \end{cases}$$

And similarly, for each other face in its relative direction.

In order to expand this scheme to higher orders of accuracy, higher order upwinding such as the second-order, quadratic-upwind-interpolation for convective kinetics (QUICK) or central difference method can be employed. The difference lies primarily in the incorporation of nodes further upstream to interpolate the value of $\boldsymbol{u}$ at the face which is being considered.

In OpenFOAM, the "Gauss linearUpwind grad(U)", discretisation scheme is used. This scheme is a second order, unbounded discretisation scheme that is corrected explicitly on the local cell gradient [79].

3.5.1.2 ***Diffusive Term Discretisation***

The strong form of the diffusive term is first approximated by its weak form which, because of the divergence theorem can be calculated by summing the dot product of the grad of u_x and the edge coefficient, $c|_f$ over each cell face. This approach to discretisation can be expanded to any Laplacian term that may otherwise exist with the fluid property changing from u_x to the relevant fluid property.

The strong form is approximated by

Eq 3.15. $$\mu \boldsymbol{\nabla}^2 u_x \approx \frac{\mu}{V_{I,J}} \int_{V_{I,J}} \boldsymbol{\nabla} \cdot (\boldsymbol{\nabla} u_x)|_{I,J} dV = \frac{\mu}{V_{I,J}} \sum_{f \in A_{I,J}} \boldsymbol{\nabla} u_x \cdot \boldsymbol{c}|_{\boldsymbol{f}}$$

This summation evaluates to:

Eq 3.16. $$\mu \boldsymbol{\nabla}^2 u_x|_{I,J} \approx \frac{\mu}{V_{I,J}} \left[\frac{\left(u_{x_{I+1,J}} - u_{x_{I,J}}\right) A_{i+1,j}}{|\mathbf{x}_{I+1,J} - \mathbf{x}_{I,J}|} + \frac{\left(u_{x_{I,J+1}} - u_{x_{I,J}}\right) A_{i,j+1}}{|\mathbf{x}_{I,J+1} - \mathbf{x}_{I,J}|} + \frac{\left(u_{x_{I-1,J}} - u_{x_{I,J}}\right) A_{i-1,j}}{|\mathbf{x}_{I-1,J} - \mathbf{x}_{I,J}|} + \frac{\left(u_{x_{I,J-1}} - u_{x_{I,J}}\right) A_{i,j-1}}{|\mathbf{x}_{I,J-1} - \mathbf{x}_{I,J}|} \right]$$

In this discretisation, it is seen that the diffusive term at point C is contributed to by the x-component of the neighbouring E, N, W, S nodes. The fractions in each term of the

discretisation are a linear approximation of the gradient using the two nodal values adjacent to each face.

In OpenFOAM, the "Gauss linear limited 1" discretisation was used. This method uses Gauss integration for discretisation and a linear interpolation scheme between nodes. It includes a non-orthogonal cell correction using the "limited 1" entry [80].

3.5.1.3 ***Pressure Gradient***

The discretisation of the gradient term in the momentum equation follows the same general approach as in previous discretisation. The strong form is approximated by the weak form which, after applying the divergence theorem results in

Eq 3.17. $$\boldsymbol{\nabla} P \approx \frac{1}{V_{I,J}} \int_{V_{I,J}} \boldsymbol{\nabla} P|_{I,J} dV = \frac{1}{V_{I,J}} \sum_{f \in A_{I,J}} (P\boldsymbol{c})|_{\boldsymbol{f}}$$

In OpenFOAM, a "*cellMDLimited Gauss linear 0.5*" discretisation was used. This method can be multi-dimensional and extrapolates the gradient of the pressure, P, at the centre node, C, to the relevant cell face (for example, e). To control the extrapolation, a coefficient between 0 and 1 is used where 1 does not allow the extrapolated value to exceed the neighbouring cell node (for example node E) value. A value lower than one allows the extrapolated value to exceed the neighbouring node value by a scale of the difference between the nodal values [81].

3.5.1.4 ***Continuity Equation Discretisation***

The divergence of the velocity field is discretised in a similar manner to the convective term because it involves a divergence operator. The only difference is that there is no need for upwinding.

Eq 3.18. $$\boldsymbol{\nabla} \cdot \boldsymbol{u}|_{I,J} \approx \frac{1}{V_{I,J}} \int_{V_{I,J}} \boldsymbol{\nabla} \cdot \boldsymbol{u}|_{I,J} dV = \frac{1}{V_{I,J}} \sum_{f \in A_{I,J}} \boldsymbol{u} \cdot \boldsymbol{c}|_{\boldsymbol{f}}$$

3.5.1.5 ***Temporal Discretisation***

Temporal discretisation or numerical time-stepping can be explicit or implicit. The key difference is that, in an explicit scheme, the next time step data is evaluated by using current time-step data (for example a Forward Euler Method) whereas an implicit scheme rather evaluates the temporal terms by using the data in the next time step (for example, the Backward Euler Method).

In explicit schemes, it is key to calculate the limit on the time-step size so that the propagation of flow information through each cell in the mesh is able to be captured within one time-step. The Courant-Friedrichs-Lewy (CFL) condition says that

Eq 3.19. $$\Delta t < \min \left\{ \frac{\Delta x_{eff_i}}{u_{diff_i}} \right\}$$

Or

Eq 3.20. $$\Delta t_{simulation} = \Delta t_{min} CFL$$

Where

- $0 < CFL \leq 1$
- Δx_{eff_i} is the effective cell size centred around node i, for which the calculation is specific to the cell type under inspection
- $u_{diff_i} = |\boldsymbol{u_i}| + \frac{\mu}{\rho \sigma_{VN} \Delta x_{eff_i}}$

  u_{diff_i} is the diffusive velocity at a specific time step, and σ_{VN} is the Von Neumann number

In OpenFOAM model, the "Backward Euler" temporal discretisation scheme was applied. This is a transient, second order, implicit time-stepping scheme. The discretisation of the x-component of the temporal term is thus simply

Eq 3.21. $$\frac{\partial}{\partial t}(\rho u_x) = \frac{1}{\Delta t}\left(\frac{3}{2}\rho u_x^{n+1} - 2\rho u_x^{n} + \frac{1}{2}\rho u_x^{n-1}\right)$$

Where n refers to the current time-step, $n+1$ the next time step and $n-1$ the previous time step [82].

3.5.2 PISO and SIMPLE Algorithms

Following discretisation, the final step of the finite volume method is to solve the Navier-Stokes equations to yield the pressure and velocity fields. One method is the Semi-Implicit Method for Pressure-Linked Equations (SIMPLE) Algorithm, which is an iterative pressure-based solver that uses a staggered grid to store scalar values at cell nodes and velocity values at cell faces. The SIMPLE algorithm begins by substituting an initial guess of a pressure field and an initial guess of a velocity field into the discretised momentum equations. The corrected pressure field can then be calculated and substituted back into the momentum equations to solve for the corrected velocity field. It is common to use a relaxation factor so that the corrected pressure and velocity fields progress in smaller increments. This can benefit the simulation stability, however, decreases the simulation speed.

This loop may be iterated more than once in a time-step to improve the accuracy of the pressure and velocity fields. In a steady-state case, convergence criteria can be defined such that the iteration stops once the solution does not change beyond a defined threshold. In a transient case, a numerical time-step method would be applied to find the first guess of the pressure field at the next time step and the SIMPLE algorithm started again.

The PISO algorithm (Pressure Implicit Split-Operator) is based on the SIMPLE algorithm and differs by introducing more than one corrector step before testing convergence [76].

The reader is directed to Appendix 2 for detail on the mathematical procedures as well as algorithm schematics of the SIMPLE and PISO algorithms.

3.6 HAEMODYNAMIC FLOW

3.6.1 Pressure Units

Incompressible flow conditions enforce constant fluid density and so the Navier-Stokes equations can be divided through by the density. Subsequently, each fluid property is converted to its kinematic relative as well as the pressure field being scaled by the density. The result of dividing the scalar pressure field by the fluid density is referred to as the kinematic pressure which has the units:

Eq 3.22. $$\frac{P}{\rho} = \frac{kg.m^{-1}.s^{-2}}{kg.m^{-3}} = m^2.s^{-2}$$

Without adapting the default solvers, OpenFOAM requires that pressure for a problem be defined in these units and consequently will output the pressure solution in these units [83]. Thus, during post-processing, the kinematic pressure field will need to be multiplied by the fluid density to obtain the field in the unit of Pascals.

The pressure unit which is used in a clinical setting for blood flow is millimetre mercury ($mmHg$). The relationship between $mmHg$ and Pascal is

Eq 3.23. $$1\ mmHg = 133.32\ Pa$$

Thus, in an OpenFOAM simulation of blood flow, the output pressure data must first be multiplied by the fluid density and then divided by 133.32 to obtain clinically relevant pressure values.

3.6.2 Reynolds Number (Re)

The Reynolds number is a dimensionless number that effectively quantifies the ratio of inertial and viscous forces as a result of flow. The Reynolds number can be calculated using Eq 3.24

Eq 3.24. $$Re = \frac{\rho v l}{\mu}$$

Where:

ρ = fluid density $[kg.m^{-3}]$

v = average fluid velocity over a cross-section $[m.s^{-1}]$

l = characteristic length of conduit $[m]$

μ = fluid dynamic viscosity $[Pa.s]$

Reynolds numbers indicate whether the flow regime is likely to be laminar ($Re < 2000$), turbulent ($Re > 4000$) or in transitional state between the two ($2000 < Re < 4000$) [84].

3.6.3 Womersley Number (Wo)

The Womersley number is used in pulsatile flow to indicate whether the flow can be considered quasi-steady or if the pulsatility would impact the ability for flow velocity to respond to the changing pressure gradient. The Wormersley number can be calculated by Eq 3.25

Eq 3.25. $$Wo = \frac{L}{2}\sqrt{\frac{2\pi fr}{\nu}}$$

Where:

L = Characteristic length $[m]$

fr = frequency $[cycles/s]$

ν = kinematic viscosity $[m^2/s]$

In the event that $Wo > 1$ it can be said that flow is longer quasi-steady and as a result a phase shift will occur between fluid flow and the driving, pulsatile pressure gradient. High Womersley number flow also indicates that a flow profile may never fully develop and, in fact, may lead to complex velocity profiles with both forward and backward flow occurring on the same plane [85].

4. EXPERIMENTAL APPROACH

The breakdown of the pipeline methodology that was used to conduct a patient-specific CFD study of blood flow in vascular structures is presented in Figure 4-1. The process which was followed at each step is hence discussed in a way that the results should be reproducible.

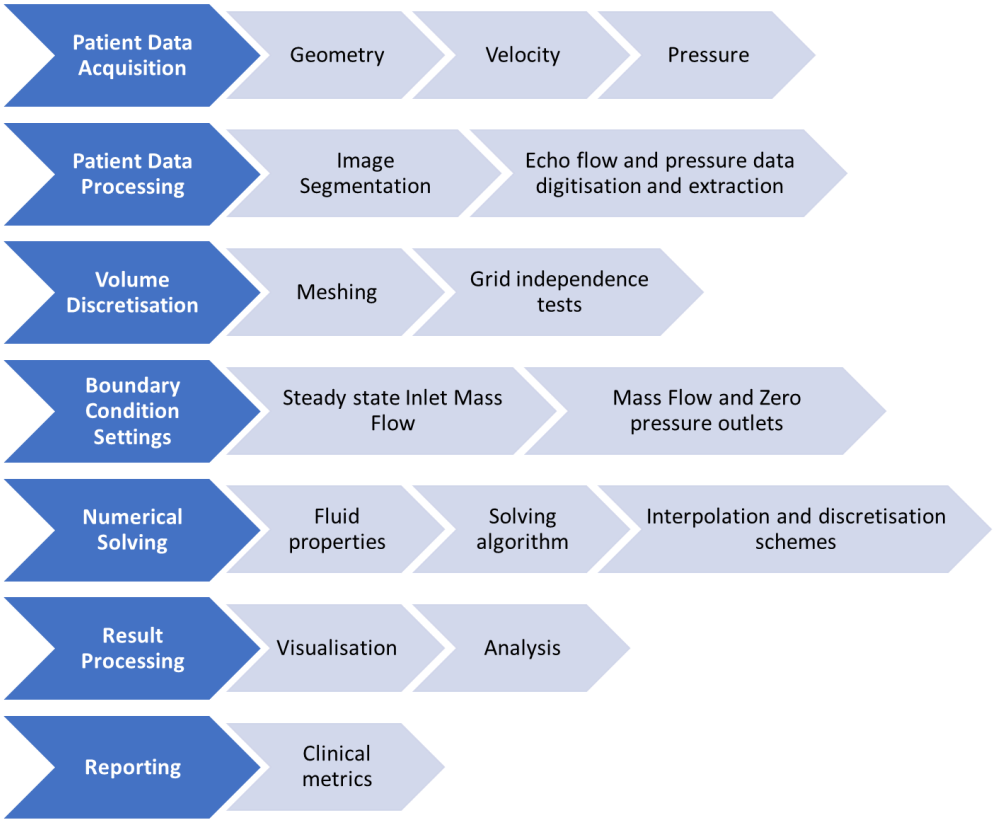

Figure 4-1: Breakdown of the methodology for a patient-specific CFD haemodynamic modelling pipeline for coarctation of the aorta.

4.1 PATIENT DATA ACQUISITION

The development of the patient data collection protocol was important in initialising and defining the velocity, pressure and geometry of the case. Data was collected retrospectively and in-line with the Red-Cross War Memorial Children's Hospital and University of Cape Town's research and ethical practices. Ethical clearance was provided by the University of Cape Town Ethics Committee under ethics number HREC Ref R017/2014. Over the course of the pipeline development, the overarching consideration was its clinical applicability. In this regard, the collaboration with clinicians and technical staff was of utmost importance.

4.1.1 Clinical Facilities

RXH is a state funded paediatric hospital which serves 250 000 patients each year from the greater Cape Town area and Africa [86]. Discussions and planning sessions were held between engineers and the clinical team to determine the possible approach towards patient data collection based on the equipment which was available and the protocol of standard clinical practice. In discussion with the clinical team the following was determined:

- Imaging modalities were realistically restricted to CTA. Although there was an MRI facility at RXH, the software required updating and there were no human resources able to conduct cardiac MRI or phase contrasted MRI.
- Standard clinical procedure at RXH for a paediatric CoA patient may include catheter pressure measurements, x-ray angiography and or doppler echocardiography. CTA would only be conducted where further investigation was needed to confirm or rule out a CoA or co-morbidity diagnosis. This was in consideration of the added exposure to ionising radiation of a CTA and the health risks it poses to the patient.
- Data collection for the study was constrained to what could be obtained during standard procedures for diagnosis and care. As a result, there were no ethical grounds for conducting invasive or potentially harmful investigations for the sole purpose of this study. It was however permitted for the engineering team to request specific measurements to be taken during standard procedures that would otherwise not have been obtained for clinical purposes. These requested measurements were agreed to be taken at the discretion of the clinician and with the highest regard for safety of the patient.

4.1.2 Patient Selection Criteria

As per the ethics approval for the project, patient data was allowed to be collected retrospectively. Initially, it was proposed that a set of criteria would be established to isolate appropriate cases from the RXH database. The inclusion criteria, in order of priority were:

1. Diagnosis of typical coarctation of the aorta
2. The worklist for the patient must include a pre-repair CTA DICOM stack.
3. The patient must have had an accompanying doppler echocardiography study which should at least have included:
    a. Colour doppler and flow velocity measurements at the inlet to the aorta over at least four cardiac cycles
    b. Colour doppler and flow velocity measurements at the site of the coarctation over at least four cardiac cycles
    c. ECG heart rate data during each measurement

It was consequently recognised that the overlap between the data required for clinical decision making and data required for patient-specific haemodynamic models was small. A specialised protocol for data collection for the purposes of patient-specific CFD models was hence developed such that it would align with the clinical and ethical considerations described above.

4.1.3 Patient Data Collection Protocol and Considerations

4.1.3.1 ***Geometry***

Considering the available facilities that were described in section 4.1.1, the study would make use of CTA scans of the patient that were acquired during standard clinical protocol to segment the diseased vessel geometry. The properties of the CTA scan that was conducted are summarised in Table 4-1.

Table 4-1: Acquired CTA scan and DICOM image properties

Scan Time:	**714** $[ms]$
Number of Slices:	256
Spacing between slices:	0.5 $[mm]$
Slice Array dimension:	$512\ x\ 512\ pixels$
Pixel dimension:	$0.3691 \times\ 0.3691\ [mm\ x\ mm]$

A CTA was not conducted following the repair of the coarctation and thus transthoracic echocardiography was used to obtain indications of the new vessel geometry dimension, albeit in 2D.

4.1.3.2 ***Velocity Data***

Doppler transthoracic echocardiography (TTE) was used to obtain flow data at several locations in the aorta. Transthoracic echocardiography was chosen due to its non-invasive nature, low risk to the patient and ready availability at RXH and more broadly across resource constrained hospitals.

The velocity-time profiles and doppler colour maps were obtained using either continuous or pulse wave echocardiography as decided by the clinician for the best result. The acquired data was first used to define the velocity boundary conditions at the inlet and outlet patches. Secondly, the velocity data and pressure gradient information at the site of the coarctation was obtained for the comparison with the CFD results.

The locations where the data was intended to be collected before and after the surgical intervention is shown schematically by green triangles in Figure 4-2 with full location descriptions detailed in the clinical protocol forms in Appendix 3. Ideally, the locations of the

measurements were to remain consistent with their descriptions, however, it was accepted that there would inevitably be variation due to the changes in the clinical setting and how restless the patient was during the investigation.

4.1.3.3 ***Pressure Data***

Due to the assimilation of the project methodology with standard clinical practice, it was not feasible to have catheter pressure measurements taken for this case. There was no clinical benefit in conducting a catheterisation procedure given the added risk to the patient and, pragmatically, the cost. It was thus decided that it would not be prudent or responsible to conduct a catheterisation procedure for the sake of obtaining data for this project only and so the model would be based on echo derived measurements only.

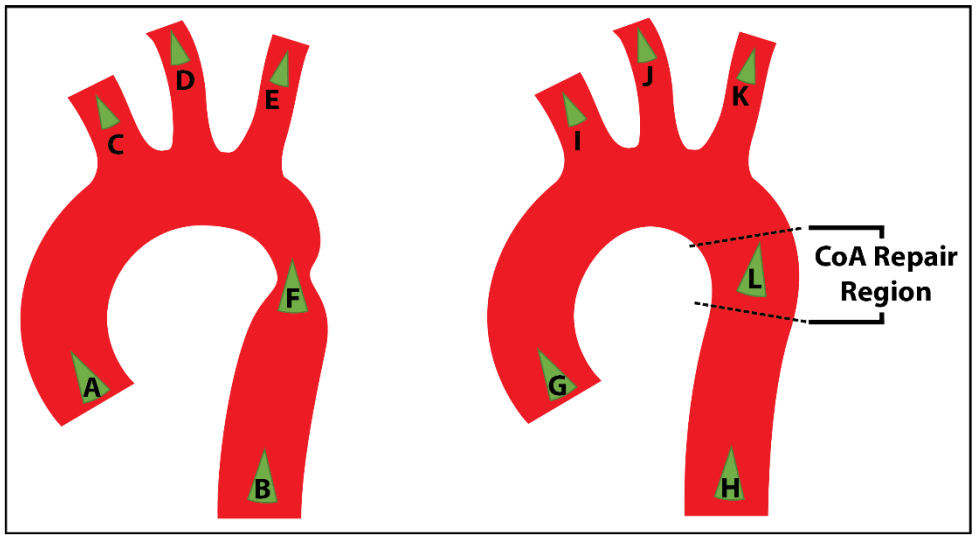

Figure 4-2: Schematic representation of the location of doppler transthoracic echocardiographic measurement sites before (left) and after (right) intervention. Each site labelled A – L relates to the description in Appendix 2 for the use in defining boundary conditions or verifying results.

4.2 GEOMETRY EXTRACTION AND DESIGN

One of the fundamental aspects of a patient-specific CFD study is the unique geometry of the patient's vascular system, or, in other words, the region of interest (ROI) which must be segmented. The ROI, schematically shown in Figure 4-3 was chosen to be the portion of the aorta which started at the aortic sinus and terminated at the descending aorta at the level of the diaphragm. The innominate artery (innominate), left common carotid artery (LCCA) and left subclavian artery (LSCA), collectively referred to as the supra-aortic branches, were included in the ROI but were purposefully terminated prior to any bifurcation. Furthermore, coronary arteries and intercostal arteries were excluded.

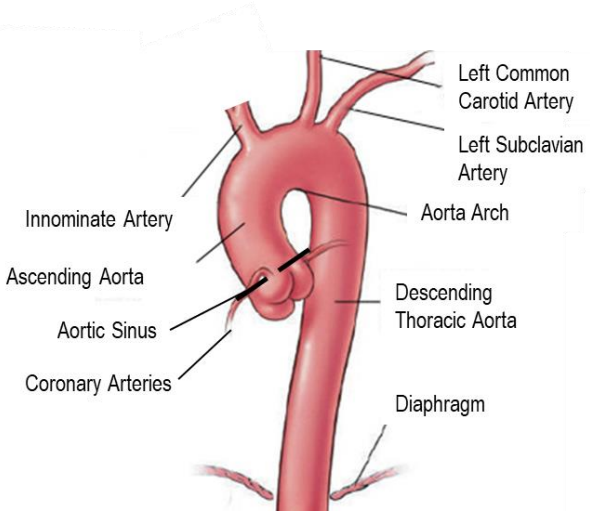

Figure 4-3: Schematic diagram of region of interest (ROI) to be segmented. Image adapted from Cleveland Clinic: https://my.clevelandclinic.org/health/treatments/17527-thoracic-aortic-aneurysm-surgery

The segmentation of the ROI from the patient's CTA DICOM data was translated into the pre-repair surface geometry (referred to as case 1). This surface was used as the baseline geometry for the *in silico* design of the two geometries which approximated the coarctation site post-repair (referred to as case 2) and if it were a healthy aorta (referred to as case 3).

4.2.1 CTA Image Segmentation and ROI Modelling

The open source modelling toolkit, SimVascular [12], was used for segmentation. The vessel path and wall at each slice in the DICOM image stack was identified using a combination of manual and pixel intensity-based thresholding techniques. Due to the impact that image noise had on the ability to delineate the aorta (shown in Figure 4-5), the use of less labour-intensive methods was limited [61] and, as a result of taking a manual approach, it was also unnecessary to apply any image filters.

Manual segmentation was accepted to be highly subjective, however, for the sake of consistency, measures were taken to identify the aorta lumen as consistently as possible. Knowledge of the aorta anatomy and expected pathophysiology made it possible to identify the aorta blood pool and the centre point of the vessel in each DICOM slice. To judge the centre point, the sagittal, coronal and axial planes of the DICOM image stack were adjusted so that they intersected at the centre of the vessel. Each intersection is shown by blue and red cross hair markers in Figure 4-4. SimVascular interpolated a vessel pathway between each point which was smoothed using a Fourier smoothing function of order 10.

For segmentation, a plane was generated, whose origin was a point on the vessel pathway and the normal was tangent to the path at that point. Figure 4-6(C) shows how the intensity values of the voxels that were intersected by the plane were displayed and used in segmentation. SimVascular's "Threshold" method with a value of 250 was used to first approximate the location of the vessel wall on the plane. This approximation was converted to a five-point spline with Fourier smoothing of order 5 using the "SplinePoly" tool. The final segmentation was made by adjusting the control points until the spline better matched the ROI. Figure 4-6 (A) and (B) shows the result of this segmentation procedure at a slice in the descending aorta. As can be seen in Figure 4-6 (C), the segmentation spacing was reduced in regions of sudden geometry changes such as the arch and coarctation site. The process was then repeated for each vessel for which the resulting segmentation contours are shown in Figure 4-7.

To avoid an outlet patch being in a region where there may be flow recirculation, the outlet patches were extruded by approximately ten times their hydraulic diameter to allow flow to develop before reaching the outlet. This is particularly important in short vessel segments such as the innominate artery where the vortices and chaotic flows are still present at the non-extended outlet patch. Following the extension, all segmented vessels were merged and smoothed using the process shown schematically in Figure 4-8 in order to reduce the sharp angles at the intersection of each vessel. The inlet, outlet and wall patches were then labelled. The entire process results in the geometry shown in Figure 4-9.

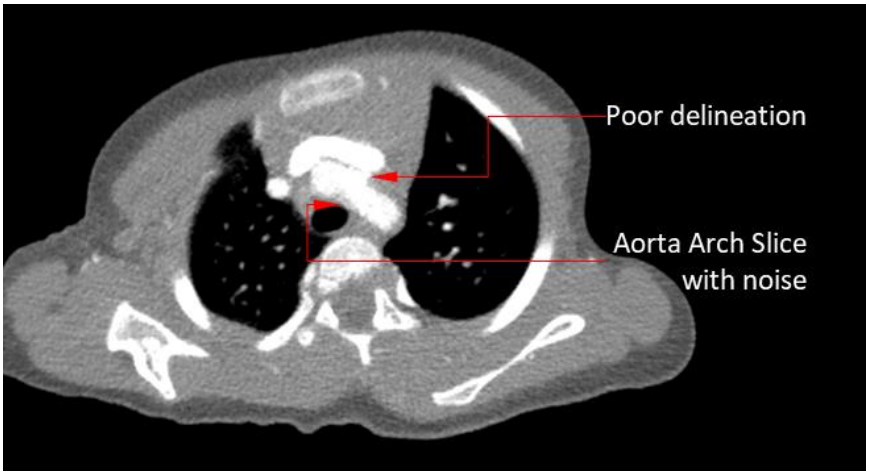

Figure 4-5: Example slice from the CTA DICOM stack which illustrates a case of image noise and the poor delineation of the aorta from other features. These contributed to the limitations of implementing advanced segmentation techniques such as level-set approaches

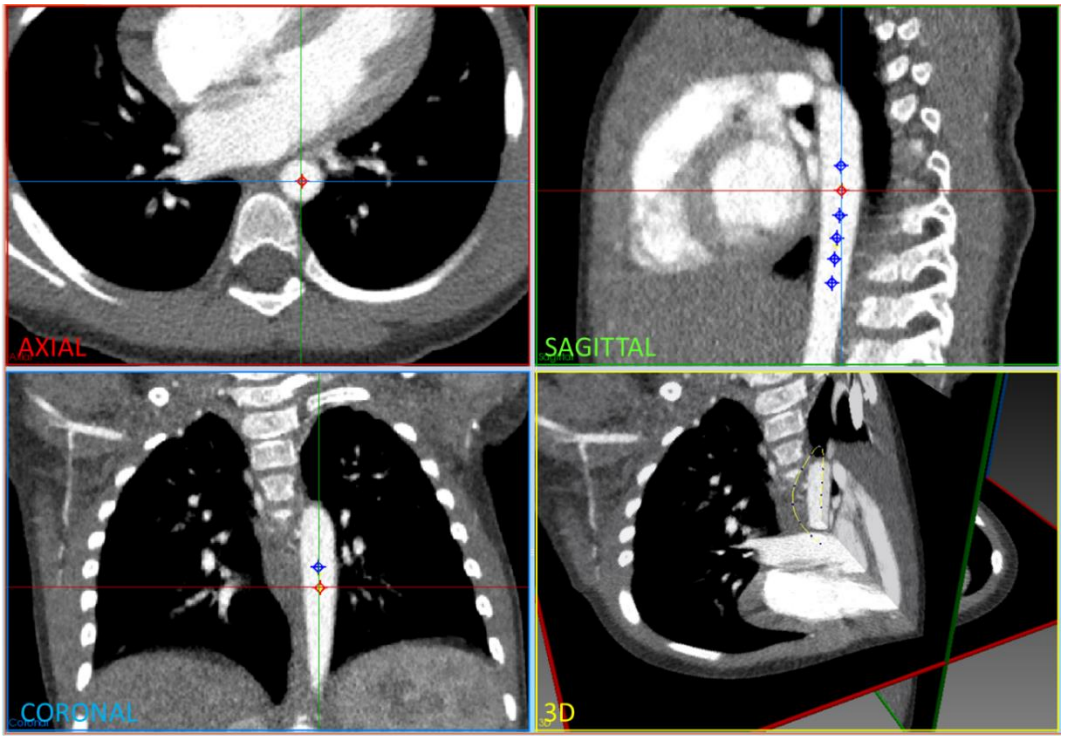

Figure 4-4: A point was placed, to the best of the operator's subjective knowledge, at the centre of the aorta as it was shown in the sagittal, coronal and axial views.

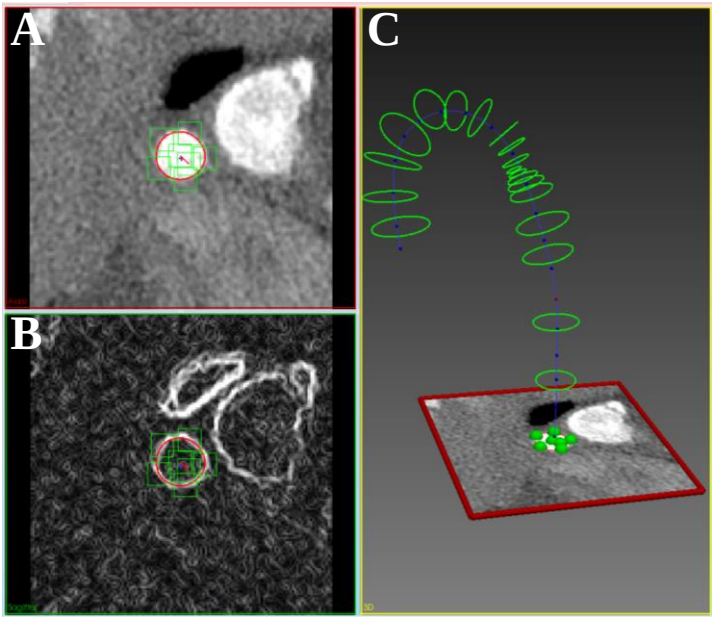

Figure 4-6: (A) shows an example of a PolySpline which was adjusted to follow the vessel wall. (B) shows how the edge detector kernel filter highlights the edge of the blood pool to guide the placement of the spline control point (green squares). In this case there was a clear edge, but this was not generally the case at other location. (C) shows how the plane followed the centreline and visualised the cross section of voxel data.

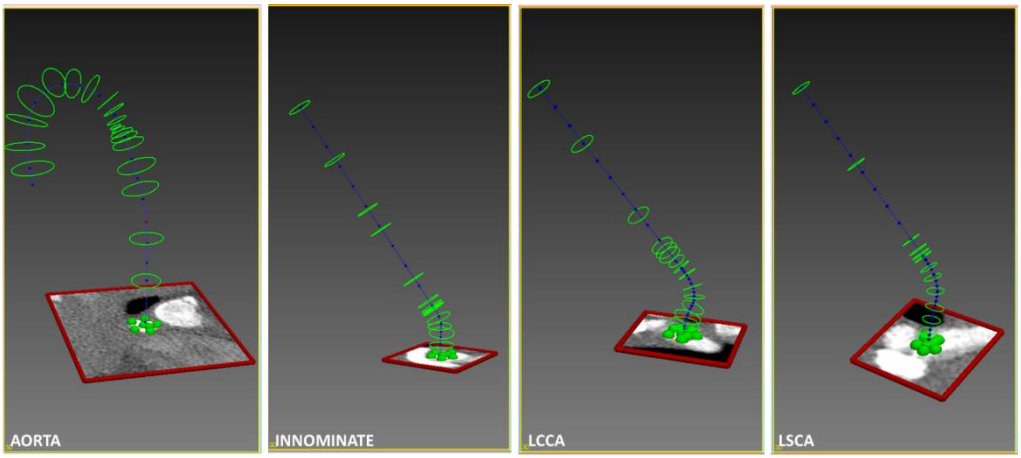

Figure 4-7: Segmentation contours of each constituent vessel of the final model with extended outlets. From left to right is the Aorta, Innominate, LCCA and LSCA.

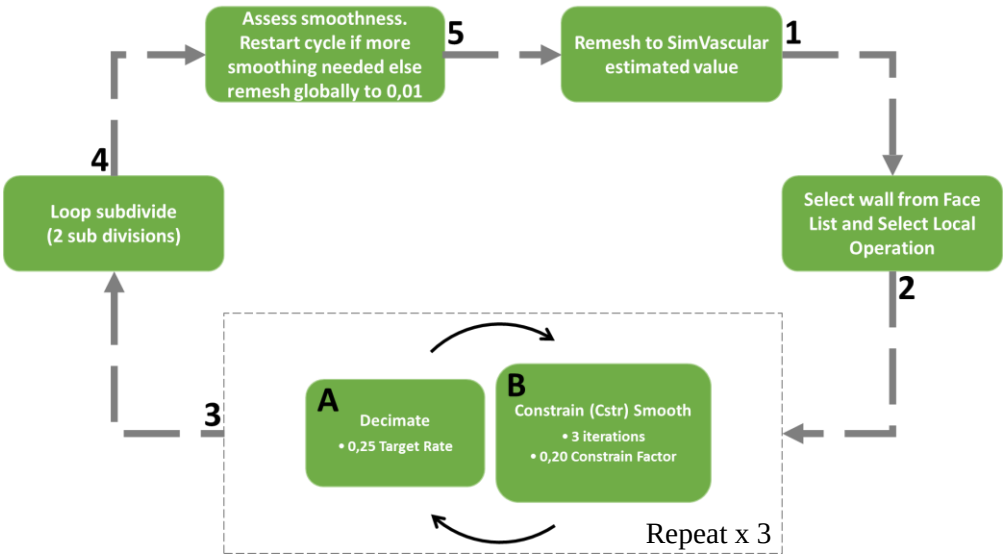

Figure 4-8: Surface meshing and corner smoothing cycle starting at 1 and following the arrows with sub cycle at phase 3.

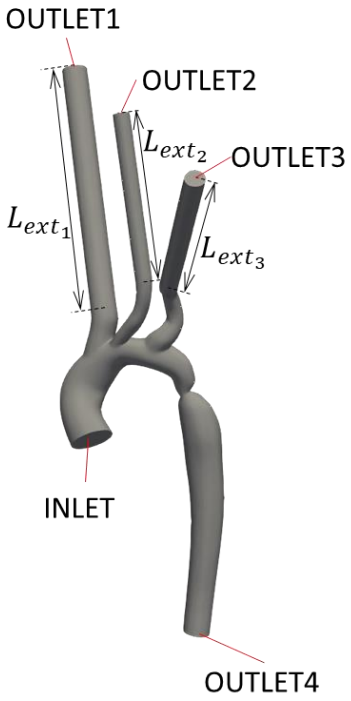

Figure 4-9: Segmented pre-repair model with labelling after merging each vessel segmentation and extending each supra-aortic branch outlet

4.2.2 Intermediate and Final Geometry Design

The design for the two artificially generated geometries was based on expanding the segmentation contours in the region of the coarctation to approximate the post-repair and an idealised healthy aorta coarctation ratio. While the idealised geometry was hypothetical, the post-repair coarctation diameter was set based on diameter measurements taken during a post-repair echocardiography investigation. Furthermore, the assumption was made that, in this affected region, the segmentation contour would be circular.

It is important to note that these cases were created to show a trend in relevant haemodynamic properties as a result of the coarctation expanding and not to accurately represent the expansion of the geometry itself as may be found using FSI or direct clinical data such as CTA image dataset. The coarctation ratio was defined as the ratio between the diameter at the narrowest point of the coarctation site and the diameter of the descending aorta at the level of the diaphragm as expressed in Eq 4.1.

Eq 4.1. $$R = \frac{D_{Co_i}}{D_{DAo}}$$

where D_{Co_i} is the diameter of the site of the narrowing and i refers to the case number of the geometry in question. D_{DAo} refers to the diameter of the descending aorta.

The resulting coarctation geometries for the unrepaired, post-repair and healthy geometries, henceforth referred to as case 1, case 2 and case 3 respectively, are shown in Figure 4-10.

Figure 4-10: Manual methods were used to model the change in coarctation modelling resulting in the three test cases shown.

4.3 VOLUME DISCRETISATION

The chosen mesh generation package was the commercial ANSYS ICEM CFD (version 19.2). It is recognised that the use of a commercial meshing package contradicts the aim of the project to develop an open source based CFD pipeline. However, this choice was justified by the priority to be able to develop the complete approach for the pipeline as far as possible with open source packages and using commercial packages if necessary, to speed up development. To this end, results were generated with all but the meshing component of the pipeline ultimately being open source. In addition, the quality of the mesh was prioritised to give the numerical solver a good foundation and so, ICEM-CFD continued to be used for meshing to avoid committing lengthy periods of time refining results of unfamiliar meshing packages.

The bearing that the mesh quality carries on the efficacy of the numerical solver is significant and so the design of the mesh was required to appropriately discretise the complex organic geometries of each case. As has been described, there are several types of finite volume cells that could be used in the generation of a mesh. In addition, due to corners and changes in vessel diameter, it is expected that, in some locations, complex or high velocity flow regions may occur which would require regional mesh refinement.

In this case the meshing strategy was to use the automatic meshing capabilities of ICEM-CFD to generate tetrahedral cells for the volume mesh and triangular prism cells for the boundary layers at the wall. The size of the tetrahedral cells was bounded by the specified maximum and minimum cell size while the prism cells were, in addition, defined by the total prism layer height, prism layer growth ratio and first prism layer cell height. In this case, five layers of prism cells constituted the boundary layer. Investigating the optimal number of boundary layers was not in the scope of the research and so this was assumed to be sufficient.

It should also be noted that, although boundary layers are less crucial for laminar flow modelling, the point in this case was to add flexibility to the pipeline so that the meshing constituent is applicable in future cases. In future cases it is expected that surface topology will vary, haemodynamic properties such as wall shear stress will be analysed and turbulence models may be included and it is in these cases where boundary layers will be important. In this single, exploratory case these considerations are out of scope, however the meshing constituent of the pipeline at least has included consideration for its future application.

4.3.1 Regions of Refinement

The results presented by previous studies in literature showed the typical flow features of CoA haemodynamics such as helicity and recirculation zones. In these regions, the mesh would need to be refined to be able to capture this detail.

ICEM-CFD curvature-based refinement was used to automatically adjust the cell size based on the curvature of the geometry. This had the benefit of significantly reducing labour and total meshing time and so was a more reproducible method across each case. In addition, the refinement of the mesh where curvature was high helped to better conform the mesh to the geometry by using smaller cells.

A cross section of the resulting mesh for case 1 is shown in Figure 4-11 as an example of curvature-based refinement of tetrahedral and boundary layer prism cells. This method refined the mesh at the coarctation zone and junctions of the supra-aortic branches, where important flow features were expected to develop. These cells globally conformed to the bounds defined by the maximum and minimum cell sizes. To ascertain the appropriate bounds and the other meshing parameters, a grid independence test was conducted.

4.3.2 Grid Independence Test

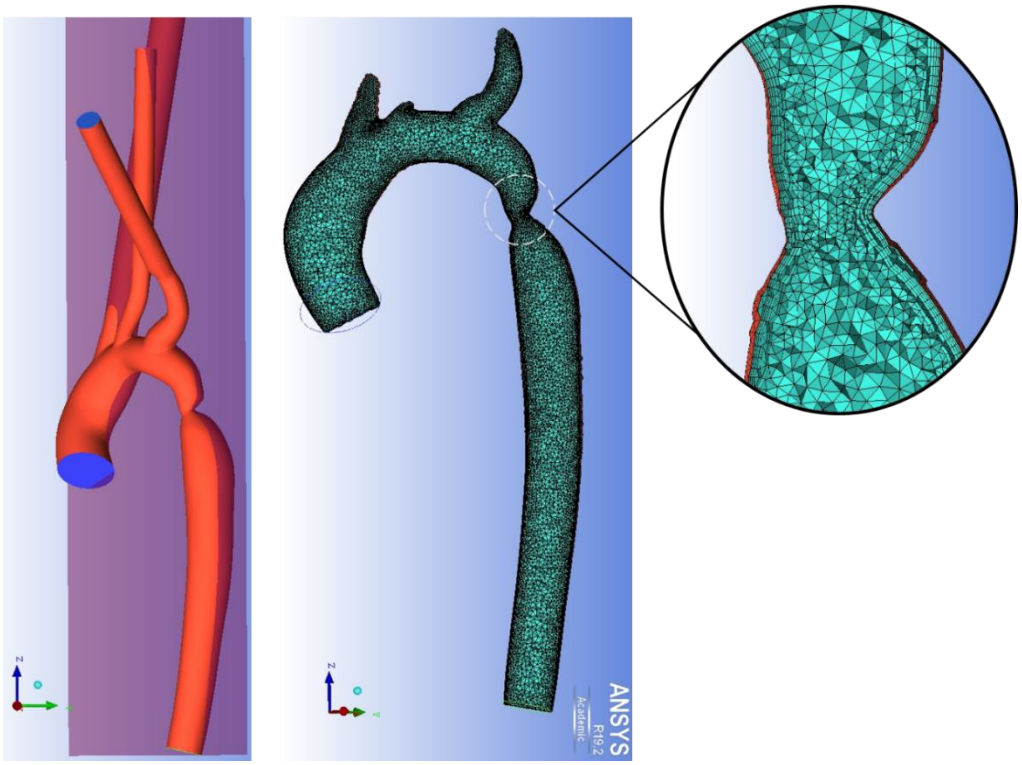

Figure 4-11: The effect of curvature-based refinement is shown on the cross section illustrating the composition of the computational mesh for the unrepaired coarctation case.

A grid independence study using 3 levels of mesh refinement was conducted to ensure that the results that were obtained were sufficiently independent from the resolution of the mesh. To do so, the open source software package, OpenFOAM (version 6), was used. Complete detail and the results are provided in Appendix 4, but the overview of the testing methodology was to assess the changes based on mesh refinement for the following parameters:

- Velocity magnitude across diameter lines in Figure 4-12 corresponding to the ascending aorta and coarctation cross sections indicated in Figure 4-12 as (1) and (7) respectively. The velocity magnitude plots at all other lines are presented but, because the velocity is primarily assessed at the coarctation, this was prioritised for independence
- Average of 25 pressure points sample at the centre of each cross section indicated in Figure 4-12

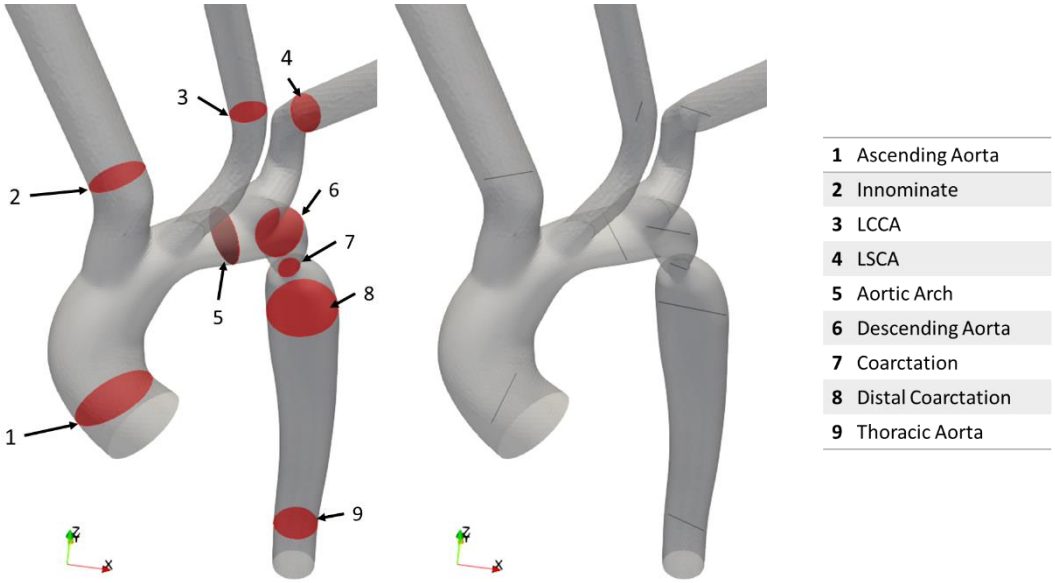

Figure 4-12: Left: Planes of interest in the grid independence study. Right: Position of sample lines which lie on each plane indicated in picture A

Figure 4-12 illustrates the locations sampled in the grid independence test of case 1. It should be noted that the grid independence tests for case 2 and case 3 were conducted in a similar fashion but their detail is not illustrated for brevity.

Each case of the grid independence test used a zero-pressure outlet boundary condition and volumetric flow rate of $7.92e-5\ m^3.s^{-1}$ inlet boundary condition. This volumetric flow rate was calculated by assuming a parabolic velocity profile at the inlet which had a maximum velocity of $1.3\ m.s^{-1}$as measured by this patient's pre- and post-repair doppler echocardiography investigations. These investigations are presented and discussed further in Chapter 5. These are known to be simplified boundary conditions but were seen as adequate for assessing grid independence so that outlet boundary conditions could be studied on an adequate mesh. The open source software package, ParaView (version 5.6), was used to post-process results and python scripts were coded to analyse the data. Eq 4.2 was used to assess

the percentage change of a given metric of interest, between meshes and relative to the coarser mesh value. Based on common practice, it was decided that a value change of less than 5% could be considered grid independent. The mesh sizing and parameters for each case which were found to produce grid independent results are summarised in Table 4-2 and supported by the sensitivity analysis results in Table 4-3.

Eq 4.2. $$\% \, Change = \frac{|\phi_{i-1} - \phi_i|}{\phi_{i-1}} \times 100$$

where ϕ is the sampled property, i refers to the current level of refinement and $i - 1$ refers to the coarser mesh.

Table 4-2: The mesh parameters that were used for each case in the grid independence study and the corresponding number of cells which were generated as a result

	Maximum Cell Size (mm)	Minimum Cell Size (mm)	No. Prism Layers	Total Prism Layer height (mm)	No. Cells Generated
Case 1	0,7	0,5	5	0,5	1 874 947
Case 2	0,7	0,5	5	0,5	1 861 212
Case 3	0,7	0,5	5	0,5	1 885 936

Table 4-3: Tabulation of grid independence data from figures above where percentage errors are colour coded according to how they relate to the 5% threshold

CASE 1																	
		1		2	3	4	5	6	7		8		9				
		$V_{ave_{line}}$	$P_{Ave_{probe}}$	$P_{Ave_{probe}}$	$P_{Ave_{probe}}$	$P_{Ave_{probe}}$	$P_{Ave_{probe}}$	$P_{Ave_{probe}}$	$V_{ave_{line}}$	$P_{Ave_{probe}}$	$P_{Ave_{probe}}$		$P_{Ave_{probe}}$				
MESH 1		0.7687	3.712	0.905	2.650	1.119	0.974	0.9703	0.4467	0.9045	0.8901		0.3408				
MESH 2		0.7680	3.734	0.874	2.684	1.105	0.984	0.941	0.4491	0.889	0.885		0.341				
MESH 3		0.7677	3.745	0.851	2.704	1.106	0.999	0.929	0.4504	0.888	0.873		0.337				
	% Changes																
1st Refinement		0,091	0,59	3,42	1,28	1,25	1,02	3,02	0,53	1,71	0,57		0,058				
2nd Refinement		0,039	0,29	2,63	0,74	0,09	1,52	1,27	0,28	0,11	1,35		1,17				

4.4 DOPPLER ECHOCARDIOGRAPHY DATA PROCESSING

As has been discussed in previous chapters, there are several choices for the specification of boundary conditions which are especially important at the outlet patches. The data collection protocol that was implemented in this case would provide 2D doppler echocardiography flow velocity measurements at the boundaries of the ROI for the pre- and post-repair cases. Although colour doppler echo could, to some extent, visualise the velocities in the scan plane, the interpretation of the 2D data into 3D velocity flow profiles was non-trivial and not within scope. Thus, the velocity time plot which was measured in the investigation would be used to define the volumetric flow rate at each boundary following data processing.

4.4.1 Digitising and Smoothing Doppler Echocardiography Data

The velocity plots in each echo dataset were developed by the clinicians after the study was completed. These plots required digitising and smoothing such that a plot could be generated from which a velocity at any point in time could be determined. The echocardiography DICOM data was viewed, measured and exported to .JPEG files using the freely available Phillips DICOM Viewer (version R3.0 SP14) [87]. The .JPEG images were imported into and digitized using the open source Plot Digitizer package [13].

When digitising the data, it was recognised that the heart rate of the patient was likely to have differed between measurements. During the post-repair investigation, the ECG monitors showed that the patient's heart rate ranged from $115 - 128\ BPM$. Thus, for consistency, the period of the heart rate for all echo data was scaled to $0.5\ s$ which represented a heart rate of $120\ BPM$. This simplifying assumption was necessary for consistency but was recognised to have discounted the physiological effect that a different heart rate would have on the cardiac output and velocities in the aorta and branch vessels.

To digitise the data, the origin, maximum time value and maximum velocity value had to be identified on the image to set the time and velocity axes and the plot domain. Following this, control points were placed on the line of the velocity plot in the image. Plot Digitiser connected each control point to its adjacent one with a straight line. This guided their placement so that they tracked the velocity plot adequately. The time and velocity value at each control point was calculated based on the position of the pixel relative to the specified origin pixel. The time and velocity co-ordinates of each control point in their *(time, velocity)* pairs were exported in a .csv file format.

This .csv file was processed using a Python script developed for this study, which conducted the following steps:

1. Insert or correct a $(0,0)$ and $(0.5, 0.0)$ *(time, velocity)* pair at the start and end of the control point list
2. Linearly interpolate points between each control point and use a moving average to smooth the data
3. Scale the velocity data such that the peak velocity of the dataset is equal to the maximum velocity value measured by the doppler echocardiography study
4. Linearly interpolate between each data point and express the velocity plot as a set of velocity values which are at equal time steps apart and export this new data to a .csv file

The final dataset for a single cardiac cycle was exported as a .csv file. The process is shown graphically in Figure 4-13 using the ascending aorta dataset as an example and the resulting smooth plot is shown in Figure 4-14.

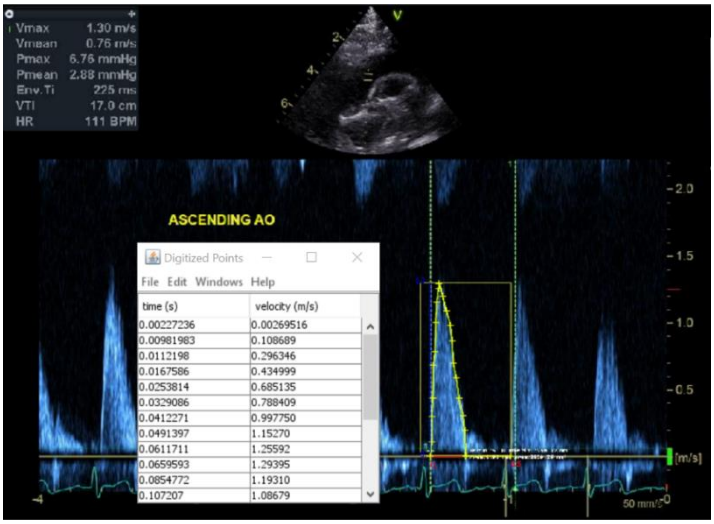

Figure 4-13: Example digitisation of the velocity data extracted from the doppler echocardiography study. The yellow crosshairs are manually placed and are joined by a straight line. The output data format which is exported to .csv is shown in the window.

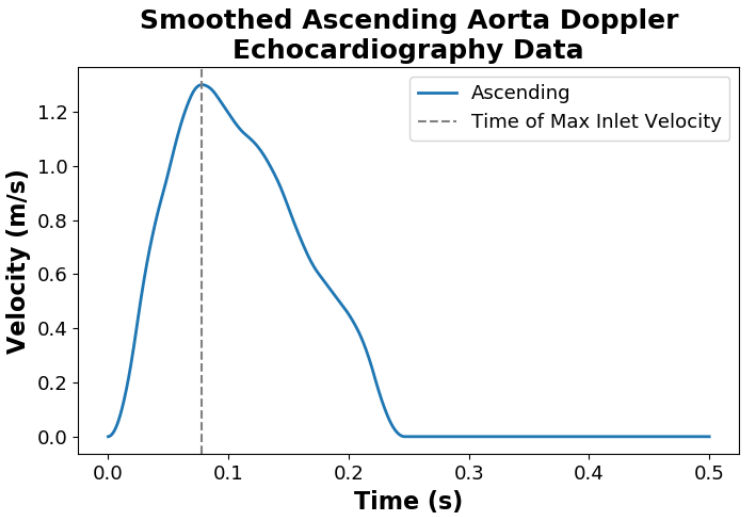

Figure 4-14: Example of the smoothed velocity plot for the ascending post-repair echo data

4.5 COMPUTATIONAL FLUID DYNAMICS STUDIES

4.5.1 Overview of CFD Studies

The CFD package, OpenFOAM (version 6), was used for each simulation. First, a study was conducted on case 1 to assess different approaches to aligning the smoothed echocardiography velocity data after being digitised (referred to as study 1). In this study, the validity of the zero-pressure outlet boundary condition was assessed. After finding the best echocardiography alignment strategy from the first study, the relevant boundary conditions were applied to each case and the effect that expanding the coarctation had on the haemodynamics was studied (referred to as study 2).

Different alignment strategies would define different volumetric flow rates through the inlet and each outlet patch and thus impact the resulting haemodynamics. The tested alignment strategies were:

1. Making no adjustments to data
2. Adjusting the amplitude of the outlet volumetric flow rates so that their sum equalled the specified inlet volumetric flow rate
3. Adjusting the phase of each outlet such that the peaks of each outlet volumetric flow rate (except the descending aorta) aligned. The descending aorta profile was phase shifted such that flow through this outlet began after the LSCA outlet flow began
4. Adjusting the phase of each outlet in the same way as method 3 as well as scaling the amplitude in the same way as method 2

The alignment strategy which resulted in the least error in the pressure gradient and maximum velocity at the coarctation site, compared to those measured from echocardiography, would be chosen as the method to proceed with. Literature denounces the use of zero-pressure outlet boundary conditions and so, in conjunction with the echocardiography data alignment study, the zero-pressure outlet boundary condition is also simulated to investigate the discrepancies in the coarctation pressure gradient and maximum velocity through the coarctation zone.

In the second study, a steady state simulation would be conducted by using the values from each profile at the peak systolic inlet volumetric flow rate. This would be used to assess the impact that expanding the coarctation zone has on the haemodynamic features such as the coarctation pressure gradient and the maximum velocity in the region of the coarctation. Furthermore, the changes to the distribution of the volumetric flow rates through each outlet as a percentage of the total volumetric flow would be shown. This would be complemented by showing the alterations to the velocity magnitude contours at each outlet patch. Considering these comparisons in ensemble would give a broad picture of how the repair of the coarctation altered haemodynamics and could serve as an example to clinical personnel as to the kind of data that could be obtained through CFD.

4.5.2 Boundary Conditions

In OpenFOAM the velocity and pressure boundary conditions were defined in the "0/U" and "0/p" directories respectively. The boundary conditions that were implemented for different simulations were zero pressure outlet, inlet or outlet volumetric flow rates and zero gradient pressure or velocity boundary in the appropriate combinations. The OpenFOAM boundary conditions were defined using the keywords "fixedValue", "flowRateOutletVelocity" or "flowRateInletVelocity" and "zeroGradient*"* respectively.

4.5.2.1 ***zeroGradient BC***

In the finite volume method, it is impossible for both pressure and velocity to be defined at the same boundary due to the implicit link between them. When one parameter (pressure or velocity) is defined at a boundary, the other (velocity or pressure) must be set to have a zero gradient using this boundary condition.

4.5.2.2 ***fixedValue Pressure BC***

OpenFOAM's built in *fixedValue* pressure condition was set to zero at all of the outlet patches and the corresponding velocity boundary condition for each outlet patch needed to be set to *zeroGradient*.

4.5.2.3 ***flowRateOutletVelocity and flowRateInletVelocity Velocity BC***

A volumetric flow rate boundary condition was implemented in OpenFOAM using the built in *flowRateOutletVelocity* or *flowRateInletVelocity* boundary condition. Although both imposed a volumetric flow rate condition, they operated in fundamentally difference ways.

The *flowRateOutletVelocity* BC imposed the volumetric flow rate by extrapolating the internal field profile to the outlet patch and correcting the velocities to meet the specified volumetric flow rate. In contrast, the *flowRateInletVelocity* boundary condition applied a plug velocity profile, based on a volumetric flow rate derived from patient-specific doppler echocardiography measurements taken during the clinical investigation of the patient involved in this study. The velocities applied to the inlet patch overruled any potential for variations in the flow profile at the inlet. The boundary layer mesh at the inlet was import for handling the sudden changes to the flow velocity profile once the no slip condition at the wall just distal to the inlet was applied.

In each of these cases, the corresponding pressure boundary condition had to be set to *zeroGradient.*

4.5.2.4 ***noSlip Wall Boundary Condition***

The wall of the geometry was simply taken as being rigid and OpenFOAM's *noSlip* velocity boundary condition and a *zeroGradient* pressure boundary was specified for the wall patch. This enforced a zero velocity to the fluid which was adjacent to the walls.

4.5.3 Numerical Solving Parameters

An OpenFOAM case directory comprises several specific scripts that define the simulation. In each script, one could select different options of fluid viscosity models, turbulence models or numerical solvers and their finite volume schemes.

4.5.3.1 ***Transport and Turbulence Models***

This script defines the fluid viscosity model. It is commonly acknowledged that blood is a non-Newtonian, shear-thinning fluid [44] and that the viscosity model for blood should reflect this behaviours However, in large vessels such as the aorta it is generally seen that the viscosity remains constant and that the Newtonian assumption holds [44], [88], [89]. The kinematic viscosity was set to $3.7736 \times 10^{-6}\, m^2.s^{-1}$, density to $1060\, kg.m^{-3}$ and a laminar model for fluid flow was used.

4.5.3.2 ***Discretisation and Interpolation Schemes***

The OpenFOAM finite volume interpolation and discretisation schemes that were set in each equation are collated in Table 4-4.

Table 4-4: OpenFOAM interpolation and discretisation schemes that were implemented

Discretization Scheme	**Method**
Temporal Discretisation:	Backward Euler
Gradient Discretisation:	cellMDLimited Gauss linear 0.5
Divergence Discretisation:	Gauss linearUpwind grad(U)
Laplacian Discretisation:	Gauss linear limited 1
Interpolation:	Linear
Surface Normal Gradient:	Limited 1

4.5.3.3 ***Solver Methods***

A geometric-algebraic multi-grid solver (GAMG) was used for the pressure fields and OpenFOAM's *smoothSolver* was used for the velocity fields. Both used *GaussSeidel* smoothers and were considered to be converged at residuals less than 1×10^{-5}. Three non-orthogonal correctors were used for the SIMPLE algorithm on which the *icoFoam* executable is based. Underrelaxation factors were set to 0.3 and 0.7 for pressure and velocity respectively.

4.5.3.4 ***Simulation Control***

For peak systolic volumetric flow studies, the *icoFoam* incompressible, laminar, transient and Newtonian fluid solver was used.

The key simulation control parameters were the time step and the length of real time being simulated. For the steady-state cases the flow would be simulated for $1\ s$ of real time flow to allow start up pressure wave reflection and propagation effects to dampen out. The solver time step size was manually adjusted such that the CFL number remained below 1.

4.6 CASE HPC JOB SUBMISSION

The CSIR Lengau HPC Cluster was utilised for running simulations. Due to OpenFOAM being open source, this facility was free to use.

A typical HPC job submission file is included in Appendix 5 and the job process flow is shown in Figure 4-15. After uploading a case file to the HPC cluster, a specific job was submitted after which it would be decomposed for parallel computing, calculated and reconstructed at

specified points in simulated time to be downloaded and post-processed. The number of cores (and thus by extension, nodes) would be used in the parallelisation of the process was calculated by aiming to have ~50 000 cells per core. A compute node typically had 24 cores and so the number of nodes required for a job was calculated by equation 3 the result of which was rounded to the nearest integer.

Eq 4.3. $$number\ compute\ nodes = \frac{total\ mesh\ cells}{50000\ cells.core^{-1} \times 24 cores.node^{-1}}$$

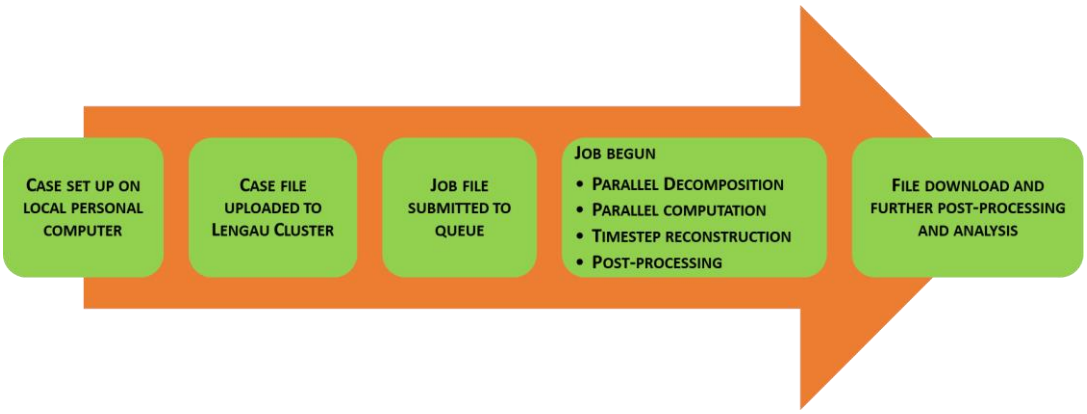

Figure 4-15: Typical HPC OpenFOAM simulation job flow chart

4.7 RESULTS PROCESSING AND ANALYSIS APPROACH

At first, the data which was collected through the patient data collection protocol was analysed. This was done to give an assessment of the data collection protocol and provide recommendations for any future iterations that would be developed. The segmentation of the geometry from this data was compared to the CTA data to confirm its alignment to the vessel wall. Following the assessment of the segmentation, the *in silico* designs of the post-repair and healthy case geometries were presented and the coarctation ratio calculated. The analysis of the CFD results for each study was centred around velocity and pressure metrics and their comparison to doppler echocardiography measurements. Finally, the overall pipeline performance was assessed based on the timeframe in which the simulation was able to be conducted, the type of results that were retrieved and their accuracy. Together, this creates an assessment of the clinical applicability and the validity of the pipeline as a CFD tool.

The bulk of analysis was based on the methodical approach towards data extraction and presentation of the haemodynamic results for pressure and velocity and using the open source software, ParaView (version 5.6). Both a qualitative and quantitative approach to analysis was taken. The visual comparison of the results through a qualitative analysis was valuable for quickly assessing the variations in the fields as a consequence of either the different boundary

conditions in study 1 or the expansion of the coarctation ratios in study 2. In contrast, the quantitative analysis could calculate specific metrics for different simulations which were compared to one another but also, importantly, to the echocardiography derived pressure measurement for verification.

4.7.1 Pressure Analysis Approach

Figure 4-16 (A) shows a slice which was generated using ParaView's "Polyslice" filter to approximately follow the centreline of the aorta. Due to restrictions by the polyslice functionality, the orientation of each portion of the polyslice in the z-axis was fixed and so could not slice the beginning of the ascending aorta as well as the supra-aortic branch vessels which curved out of the plane. However, the focus of the study was around the transverse arch, coarctation and descending aorta which were adequately captured in the slice to communicate the flow field detail. The pressure on this polyslice was visualised for qualitative comparisons between studies.

The quantitative analysis required the extraction of pressure data using the "Probe Location" tool in ParaView. Figure 4-16 (B) shows spherical probes of radius $1\ mm$ placed proximal to the coarctation and in the descending aorta, proximal to the outlet patch. The average of 25 data points within the probe sphere was calculated and used to calculate the coarctation pressure drop. It is important to note that the pressure which was being analysed was relative to a defined reference pressure, however, the pressure drop is independent of the pressure values being relative or absolute.

The pressure gradients which were calculated in the first study were compared to the echocardiography measured pressure gradient to ascertain the most accurate boundary condition. In the second study, the changes to this pressure gradient as the coarctation was expanded was of interest. All pressure results were reported in the clinically appropriate unit of $mmHg$ (millimetre mercury) which required the OpenFOAM output kinematic pressures to be multiplied by the density, $1060\ kg.m^{-3}$, and divided by the conversion factor for Pascal to $mmHg$, 133.32.

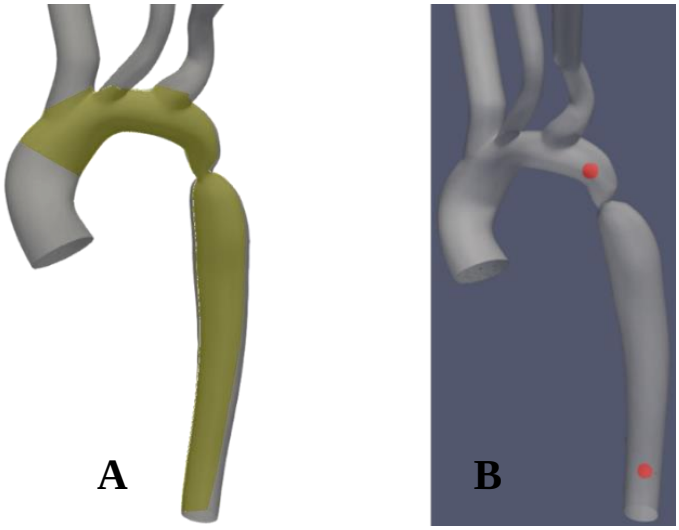

Figure 4-16: (A) shows the polyslice plane in relation to the geometry of case 1. The composition of the polyslice plane remains constant for each case geometry. (B) shows the probe locations where the average pressure at 25 points within the sphere would be calculated. These locations are kept constant for each case.

4.7.2 Velocity Analysis Approach

The velocity measurement which was important for the quantitative analysis of each case's results was the maximum magnitude of velocity through the coarctation region. This was the value which could be compared to the doppler echocardiograph measurement. The magnitude of the velocity vectors which existed on the cross section with the minimum area in the coarctation region was hence calculated.

In addition to the maximum velocity in the coarctation zone, normalised velocity vectors which were coloured by their non-normalised magnitude were plotted on the same polyslice plane in Figure 4-16 which was created previously. In the same regard as the pressure analysis, a qualitative comparison of the flow field on this slice gave an indication of the flow features which were present in the aorta as a consequence of the coarctation and its various repaired states.

The volumetric flow rate percentage splits were calculated and visualised. By viewing the volumetric flow rate percentage splits, the trend for the expected flow recovery through the descending aorta was shown. This comparison is useful, but it is recognised that by defining volumetric flow rate as a boundary condition, these are not incidental. Thus, these were not considered beyond being noteworthy.

Finally, the resulting velocity magnitude contour plots at each real outlet (prior to any extension) are of interest in study 2 to understand the effect that expanding the coarctation has on the flow regimes seen in each vessel.

5. RESULTS AND DISCUSSION

Each phase of the pipeline output a dataset that was passed on to the next step from data acquisition through geometry modelling, volume discretisation, boundary condition application, CFD simulation and finally post-processing. The outcomes of each step will be described and discussed. This gives a holistic view of the toolchain and highlights model capability. A brief discussion of the clinical collaboration with the specialists at the Red Cross hospital is conducted prior to analysing results in order to give context to the pipeline, its development and subsequently, its results.

5.1 CLINICAL COLLABORATION

The close collaboration between the engineers and clinical team of cardiologists and technical staff at the Red Cross Memorial Children's Hospital ensured the clinical realism of the process. The clinical team consisted of 6 cardiologists, 2 technical clinical staff and 1 medical officer. Cardiologists were important at all times but especially during the patient data collection protocol development, the *in silico* design of case geometries and the verification and interpretation of results. Clinical technicians were key in the physical collection of data and the medical officer was particularly useful in identifying and monitoring those patients who would meet criteria for the study.

5.2 IMAGE SEGMENTATION AND *IN SILICO* REPAIR GEOMETRY DESIGN

5.2.1 Segmentation and Design Results

The three test geometries of case 1, case 2 and case 3 that were used in demonstrating the capability of the CFD component of the toolchain are shown in Figure 5-1 (A), (B) and (C) respectively. The segmentation and subsequent geometries are presented and assessed due to their fundamental role in establishing the downstream components of the pipeline.

The importance of the segmentation accuracy is emphasised due to the high degree of subjectivity that is introduced through manual segmentation of the vessel and the role this has in defining flow dynamics. There is no gold standard for quantifying segmentation error, hence this evaluation of segmentation is also noted to be subjective. However, by superimposing the segmented surface onto the source CTA dataset, the quality of the surface's alignment with the region of interest was evident and obvious errors were able to be addressed.

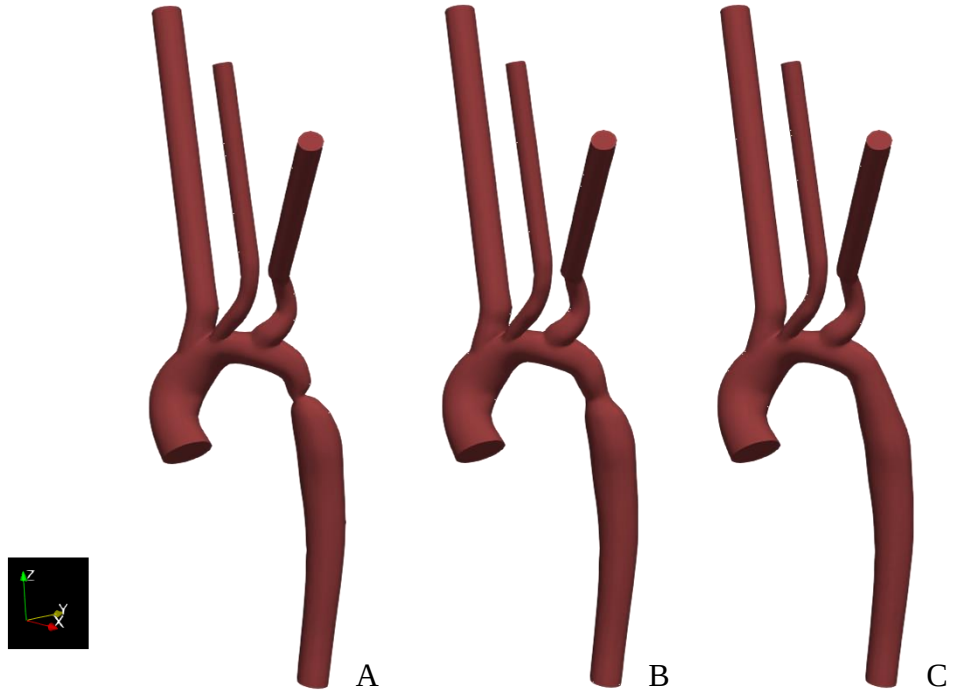

Figure 5-1: Resulting geometries of segmentation and subsequent adaptation to represent the geometry of the pre-intervention state (case 1) as extracted from CT data (A), as well as an approximation of the post-intervention state (case 2) (B) and a healthy or totally repaired aorta (case 3) (C). Geometries include the extended outlets which were artificially generated for numerical stability.

5.2.1.1 ***Segmentation Accuracy***

Ascending Aorta: The incorporation of detail of the aortic root and valves was deemed unnecessary and was not segmented as is evident from Figure 5-1. Figure 5-3 shows that, from the coronal and sagittal perspectives, the alignment of the segmented surface with the highlighted blood pool is seen to be a fair representation of the ascending aorta. It is possible that the geometry inlet patch of the ascending aorta does not lie at the level of the aortic sinus but it is thought to be adequately within the region.

Aortic Arch and Supra Aortic Vessels: The segmentation of the aortic arch can be seen in its ascending, transverse and descending segments in Figure 5-2 (B), (C) and (D) respectively. Note that, for optimising the view of the blood pool, the window level and contrast differs from those of Figure 5-3.

The general profile and path of each head and neck vessel aligned well with the blood pools in the CT slices as shown in Figure 5-2 (A-D). It was found that unification of each vessel segmentation led to physically unrealistic sharp corners at each vessel junction. Despite surface smoothing, the portion of the surface displayed in Figure 5-4 shows how the junctions remained abrupt relative to the colour rendered view in Figure 5-5 that was delivered with the CTA data.

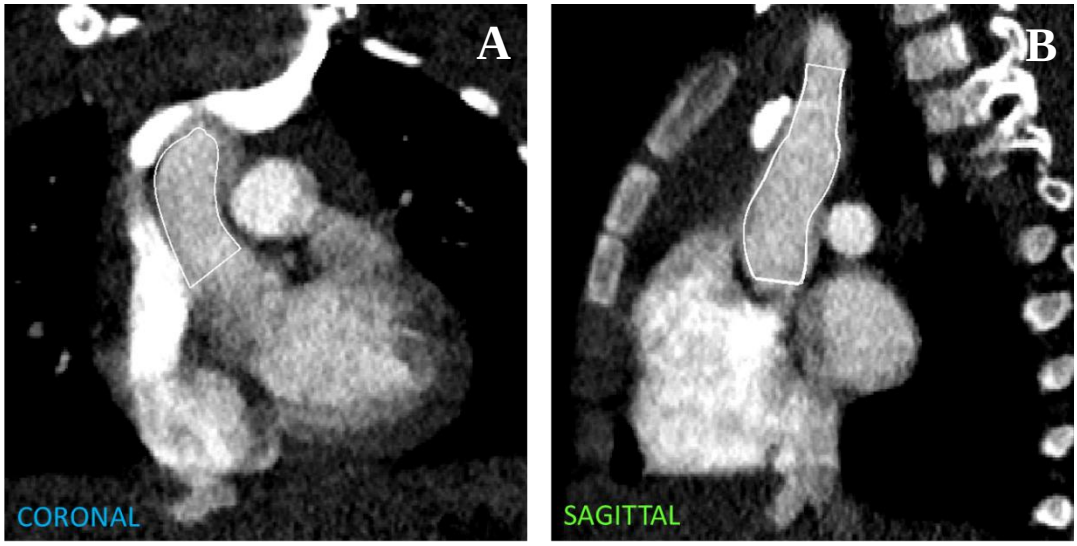

Figure 5-3: Superposition of the ascending aorta segmented surface onto the CTA images showing the inlet boundary from both the sagittal and coronal view.

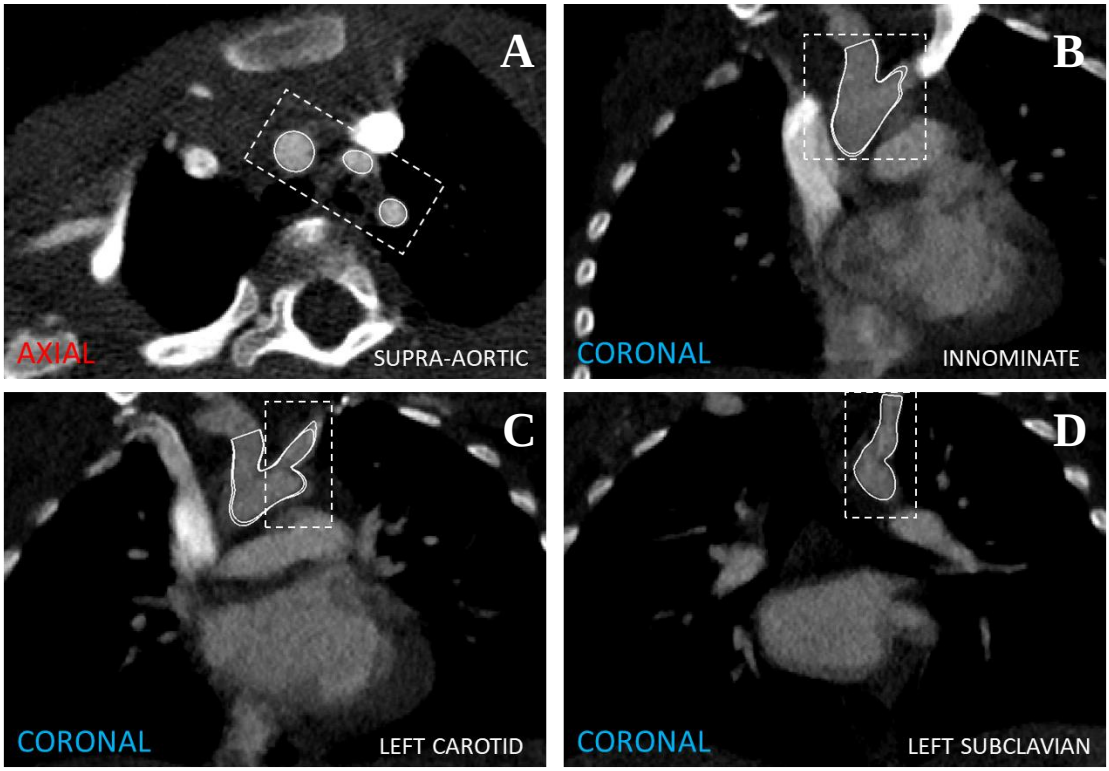

Figure 5-2: Superposition of the segmented surfaces of the supra-aortic vessels and the transverse aortic arch onto the CTA images showing the surface from a coronal and axial view

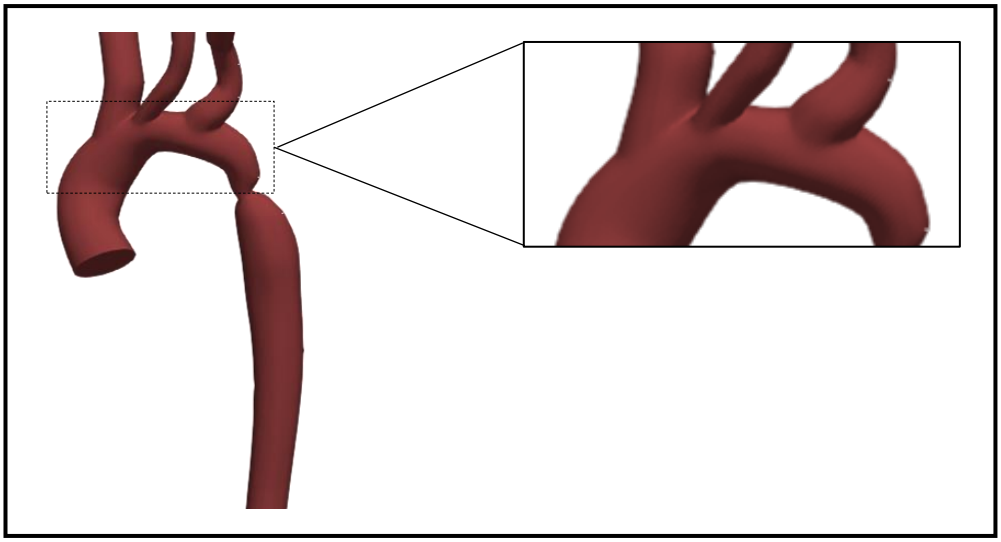

Figure 5-4: Magnification of the supra-aortic arch vessel junctions with the aortic arch which shows the abrupt and seemingly non-physical vessel junction corners.

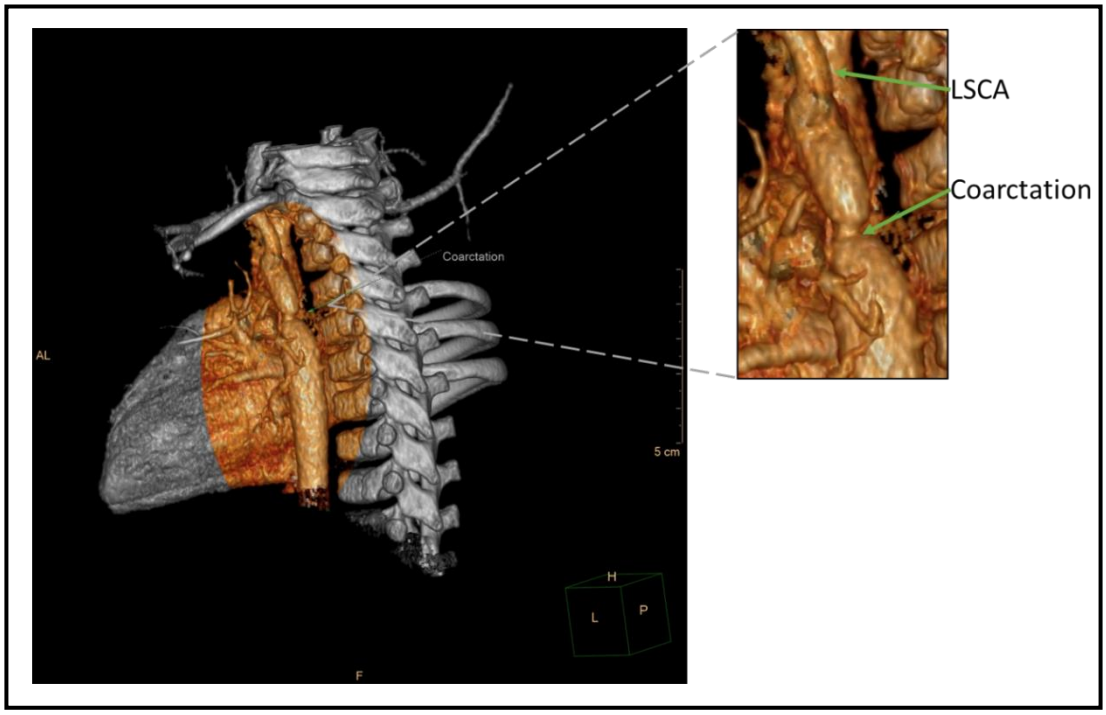

Figure 5-5: The colour rendering of the aorta with view of the coarctation, shows the shape of the coarctation in relation to the descending aorta. In addition, the left subclavian artery also shows a smooth transition onto the aortic arch.

Coarctation Segmentation: The coarctation zone is shown from the sagittal and coronal perspective in Figure 5-6. By considering Figure 5-5, it was thought that the profile detail of the coarctation as well as the distal and proximal portion of the descending aorta were captured well. Particularly in this region, manual segmentation was found to be a challenge due to the coarctation, at its narrowest, being only 10 pixels wide as found in the gradient filter of the CT slice at the coarctation in Figure 5-6 (C). The same figure also shows an example of how poor the delineation of the blood pool was in this region, by the lack of a definitive edge line in the edge detection filtered Figure 5-6 (C).

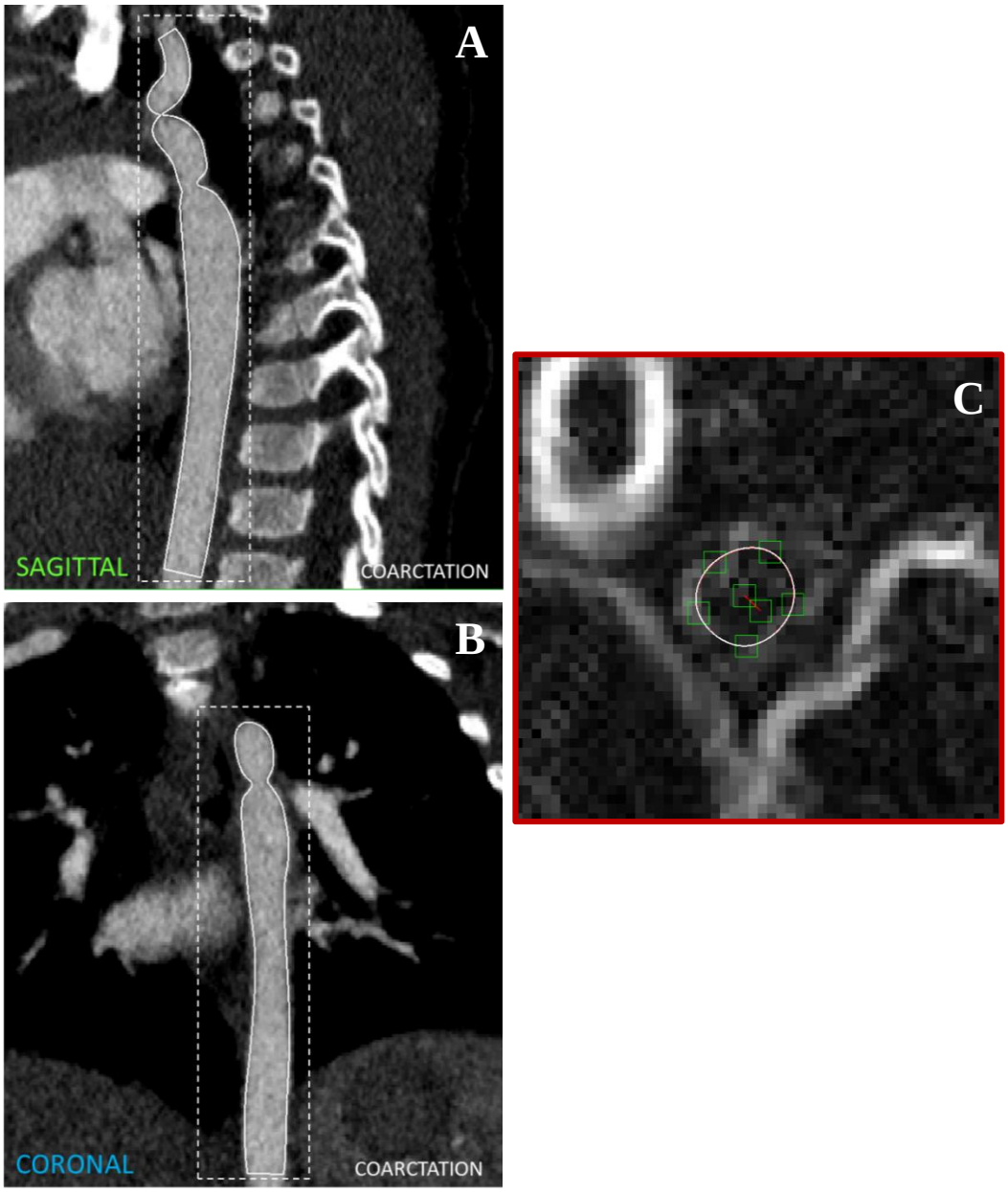

Figure 5-6: Superimposing the segmented surface of the descending aorta and coarctation shows good agreement with the blood pool when considering the sagittal (A) and coronal (B) perspectives. Image C shows an edge detection filtered CTA slice along the aorta path line at the region where the coarctation was most constricted and illustrates the lack of definitive edge lines as a result of low resolution.

5.2.1.2 ***Coarctation Zone Geometries***

As stated, the coarctation region was the only part of the surface which was modified *in silico* for the purpose of generating the repair design cases. The coarctation zone of each case geometry is shown in detail in Figure 5-7. Further, the dashed line indicates the location of the cross section whose area was used to calculate the coarctation ratios in Table 5-1 for each geometry. The location of the coarctation plane indicated by the dashed line coincided with the location and orientation of the segmentation contour which had the lowest area when generating the geometry. These locations were convenient to use due to the location and tangent data of the aorta path line at each segmentation being generated by SimVascular and stored in case files. It should be noted that geometry at the descending aorta was not impacted by the alterations made in the coarctation region. Thus, the descending aorta measurement was constant for each coarctation ratio calculation.

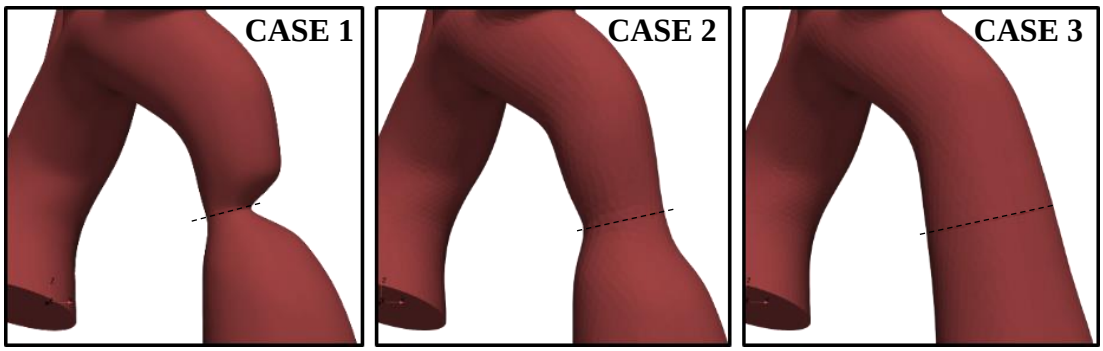

Figure 5-7: Magnification of each case's coarctation repair design. The dotted black line indicates the location of the plane with the minimum cross-sectional area that was used firstly to define the size of the coarctation and consequently calculate the coarctation ratio.

Table 5-1: Coarctation ratios calculated for each repair case by the standard set by Forbes et al. [90]

Geometry	Coarctation Area (mm^2)	Perimeter (mm)	Hydraulic Diameter (mm)	D_{Coarct}: D_{DAo}
Case 1	8.08	9.59	3.37	0.43
Case 2	25.91	17.99	5.76	0.74
Case 3	61.82	27.61	8.96	1.14
Descending Aorta	48.25	24.66	7.83	-

5.2.1.3 ***Geometry Data***

Table 5-2 collates the geometry information of each outlet and inlet patch. The hydraulic diameter could be calculated from the outlet patch area and perimeter and used to calculate the required length of the outlet extrusions. These can be seen to follow the commonly applied rule of thumb such that $L_{ext} = 10D_{Hydraulic}$.

The resulting segmentation showed that the innominate vessel was large and comparable in cross-sectional area to the outlet patch of the descending aorta. The length of each extension according to the labelling in Figure 4-9 is summarised in Table 5-2. Owing to the descending aorta having a regular cross section and being positioned far from sudden geometry changes such as junctions, this outlet was not extended in order to save computational time. Each extension length is approximately ten times the hydraulic diameter of the respective outlet patch

Table 5-2: Table collating cross-sectional areas at each inlet and outlet patch. Areas were extracted from ParaView, perimeters from SimVascular and both were used to calculate the hydraulic diameter which was used to calculate the required length of outlet extrusions

Patch ID	Area (mm^2)	Perimeter (mm)	Hydraulic Diameter (mm)	L_{ext} (mm)
Ascending Aorta (INLET)	121.80	39.14	12.45	-
Innominate (OUTLET1)	40.69	22.68	7.18	73.18
Left Common Carotid (OUTLET2)	16.52	14.45	4.57	46.00
Left Subclavian (OUTLET3)	19.33	15.69	4.93	49.93
Descending Aorta (OUTLET4)	48.25	24.66	7.83	-

5.2.2 Segmentation and Design Discussion

The segmentation of the vessel geometry from a dataset of medical images is recognised as an important underpinning of patient-specific haemodynamic CFD studies. It is important to bear in mind the context of these results within the overarching aim of creating a clinically applicable tool, as well as the clinical limitations on the available imaging techniques. The value in a segmentation method lies within achieving an acceptable level of accuracy based on the imaging data that is available, the speed of the entire process and avoidance of generating artificial pathophysiology. The result of using the open source SimVascular tool

for manual segmentation of the aorta for case 1 and the design of subsequent geometries of case 2 and case 3 can be assessed using these metrics.

5.2.2.1 ***Segmentation***

Manual segmentation is reliant on the overall quality of the imaging data and the outcome is susceptible to low spatial resolution, the presence of image noise and image artefacts. Overall, the segmentation of the geometry in the first case was of an acceptable accuracy when viewing its alignment with the vessel walls in each CTA slice, but the sharp junctions at the aortic arch are considered the primary regions where inaccuracies in the segmentation exist.

The image resolution, noise and motion artefacts were generally a challenge throughout segmentation, however it was particularly evident when establishing the form of the head and neck vessel junctions with the aortic arch. The surfaces at the junctions were expected to have a relatively gradual transition from the arch to each vessel, but sharp corners were generated instead. SimVascular's surface smoothing algorithms were used to relieve these corners. This smoothing remedied the sharp corners to some extent, however, these junctions were still considered to be non-physical. At this point it should be reiterated that the assessment of a coarctation of the aorta patient primarily rests in the pressure gradient measurement and so, without ruling out the potential impact that the form of the junction has on the results, priority for accurate segmentation was rather given to the coarctation region.

The segmentation of the coarctation in case 1 was found to be an adequate representation based on the comparisons with the 3-D rendering as well as the CTA image dataset in Figure 5-5 and Figure 5-6, respectively. It was seen that the proportion between the proximal descending aorta, the coarctation and the enlarged, distal descending aorta was visually similar to the rendered image. It should be noted that this was an automated rendering which was able to isolate regions of high intensity such as the radiopaque dye in the blood. Although, from the user's perspective, automated segmentation was not feasible, the software behind the rendering could achieve a good result. This software was not accessible but obtaining the rendering data, if possible, would be a benefit to the segmentation procedure. The challenges found in this process and the total time taken to manually segment this geometry adds to the body of literature which does not favour manual segmentation as a clinically feasible method.

It should also be recognised that, as shown in the MATCH challenge proposed by Berg *et al.* [32], user subjectivity contributes to the overall variation in the segmentation result. This is particularly relevant in manual segmentation and can be reduced by implementing more advanced segmentation techniques such as marching fronts that, with reduced user input, are more objective albeit more susceptible to inaccuracy when noise is present. These methods were available in SimVascular, however, the lack of definitive delineation between the aorta

blood pool and neighbouring structures as a result of image noise and artefacts was prohibitive. It would be fair to say that the approach going forward would be to address the root cause of the image quality shortfalls, however, there are justified limitations as to how much the imaging approach can be changed.

The premise of this project was to implement methodologies that could be assimilated easily into the clinical procedure of a coarctation patient at RXH. The simple proposal for improving segmentation would be to improve image quality through techniques such as ECG gated CTA or MRI scans. At RXH specifically, there was no capacity for cardiac or PC-MRI. Furthermore, these imaging methods pose a health risk to younger patients as they require increased doses of ionising radiation or sedation during long scans. To justify any technique which increases the level of risk to these vulnerable patients would be unethical.

It is clear that adjustments to the methodology need to be made at an image processing and segmentation level. The CTA image quality in this case's dataset prohibited the use of automated methods, but, in light of the target for clinical applicability, manual segmentation required an impractical period of time to complete. For example, a smooth and problem free manual segmentation of case 1 was found to take a full eight-hour day of labour to complete based on the time taken by the author for this study. The time cost of the manual segmentation step is a crucial area that should be addressed if a CFD method is to be applied within a clinical setting and within a useful timeframe. Owing to their decreased need for manual intervention, automated methodologies stand a greater chance of finding application in clinical decision-making processes. This sentiment is reflected in the results of the design of the hypothetical post-intervention states of case 2 and case 3 whereby advanced methods may be used to better design the shape of the coarctation following a repair.

5.2.2.2 ***In Silico Intervention Geometries***

The manual approach to generating the geometries for case 2 and case 3, by nature, holds the same subjectivity challenges as those that were presented in the segmentation of case 1. The key caveat in both case 2 and case 3 is that they are hypothetical due to the lack of CT data to directly segment the outcome. In case 2 specifically, the use of echocardiography diameter measurements make the design at best an educated approximation to the actual geometry, but an approximation nonetheless. The assumptions that were made in generating case 2 and case 3 were known to carry weight in impacting the outcome and accuracy of each downstream phase in the pipeline but were necessitated by the lack of patient data. To reduce the potential for generating unrealistic designs, the clinical team was consulted and both cases were deemed to be near realistic possibilities of the geometry after different aorta repairs. Although the procedure of designing hypothetical repairs was necessary to conduct a full haemodynamic

study, it also gave insight into one of the more practical clinical applications of a patient-specific CFD tool. To provide the means for planning intervention strategies *in silico* is a strength of CFD and could allow clinicians to predict the outcomes and recursively optimise the parameters of an intervention prior to committing to it.

Design is going to be intrinsic to this phase of the pipeline. However, there are existing methods that simulate the stenting and ballooning of vessels and these would be important to implement to reduce the dependency of the final aorta shape on the user's intuition which, if not experienced, may carry significant error [91], [92]. This would be especially undesirable if the outcome were to be informing the chosen intervention.

The coarctation ratios which were calculated in Table 5-1 show that each case lies within the ranges of coarctation ratios that literature describes as being indicators for whether or not there is a need for intervention or reintervention. A review by Forbes *et al.* [90] shows a correlation between the decision for intervention or reintervention, and a coarctation ratio which is less than 0.6. Furthermore, Forbes *et al.* suggests that a coarctation ratio greater than 1.2 would suggest aneurysm formation, while still accounting for the chance of post-stenotic aorta dilation which may be indicated by a coarctation ratio of greater than 1. None of the geometries in case 1 to case 3 are borderline in this regard. Case 1 has a coarctation ratio of 0.43 which would, by all metrics, suggest that intervention was necessary. Case 2 has a coarctation ratio of 0.74 which is considered mild enough to avoid reintervention. In case 3, the coarctation ratio exceeds 1, however it remains less than Forbes *et al.*'s criteria of 1.2 for indication of aneurysm formation. The segmented geometry does show signs of post-stenotic dilation and so a ratio greater than 1 is expected.

In considering the outcomes of the segmentation of case 1 and the geometries of case 2 and case 3, which were derived from the segmentation, this initial phase of the CFD pipeline was shown to be functional, albeit with a dependence on the subjective manual input by the user. There is clear demonstration that it is possible to use open source software (in this case the SimVascular package) to segment a patient-specific geometry of coarctation of the aorta. In addition, the pipeline has the provision for the user to generate test cases of different interventions to be able to simulate outcomes which point towards the capacity for surgical planning. One of the two fundamental aspects of a patient-specific CFD simulation is the geometry and the other is the patient-specific blood flow parameters that are used in defining boundary conditions.

5.3 DOPPLER ECHOCARDIOGRAPHY DATA ACQUISITION

5.3.1 Data Acquisition Results

The doppler echocardiography investigation was conducted on the patient in line with the data collection protocol that was developed and presented in Appendix 3. This provided pre- and post-intervention flow and supplementary geometry data at key regions of interest in the domain, and over several cardiac cycles. In reviewing the results of the doppler echocardiography images, it became apparent that steps would need to be taken to smooth the velocity-time plots and translate these into volumetric flow rates for each of their respective outlet or inlet patches. Four approaches to data processing were proposed and tested according to the strategy described previously in section 4.5.1.

5.3.1.1 ***Echocardiography Datasets***

Ascending Aorta

Recording echocardiography data at the ascending aorta was possible both pre- and post-intervention (i.e. for case 1 and case 2). In both instances, a pulse wave doppler study was used, thus capturing the waveforms as shown in Figure 5-8. Interestingly, the maximum velocity captured over the cardiac cycle was common in each measurement. Both cases were able to adequately capture more than four cardiac cycles of velocity data to an acceptable quality. A key factor which differed between the studies, and a point that carries throughout all the examples to follow, is the lack of ECG acquired heart rate in the pre-operative instance. Furthermore, the clinician-measured diameter, despite being at comparable locations, was 13 mm in the pre-intervention case and 11.21 mm in the post-intervention case, representing a 14% difference.

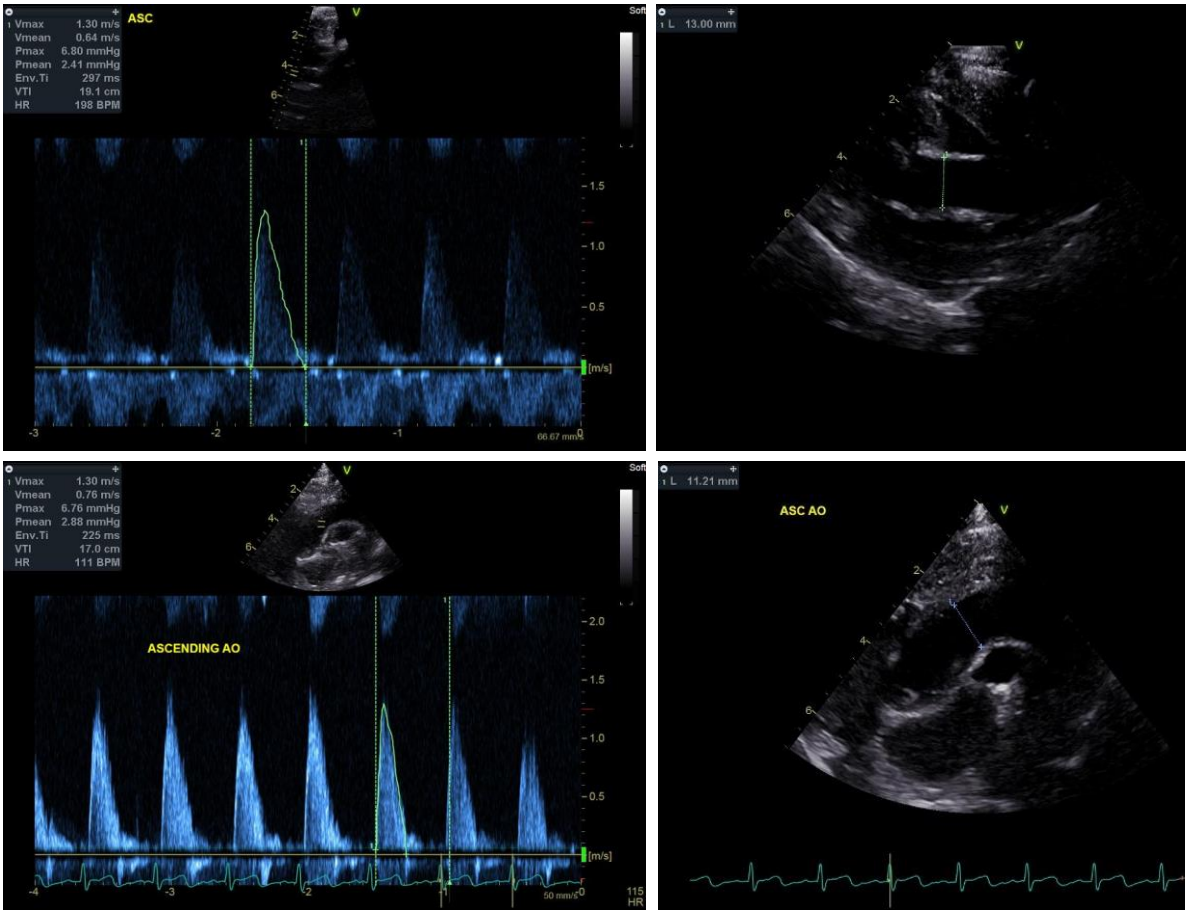

Figure 5-8: Ascending aorta echocardiography results for both pre- (top row) and post- intervention (bottom row) instances

Innominate

In both cases 1 and 2, the innominate investigation could be carried out using pulse-wave Doppler, resulting in the data shown in Figure 5-9. The pre-intervention data in Figure 5-9 lacked accompanying ECG data and illustrates the risk in using the estimated heart rate that is quoted in the information box, which reports a non-physical heart rate of $266\,BPM$. This in fact implies a severe case of cardiac fibrillation and is unrealistic. Key changes to the peak value and form of the velocity-time plot of each case are noted, which could indicate the impact of the coarctation intervention on flow in this vessel. The pre-intervention case showed a peak velocity of $1.11\,m.s^{-1}$ compared to the post-intervention $0.84\,m.s^{-1}$ representing a 24% change in peak systolic velocity. Despite some spurious peaks in each case's velocity measurements, both cases provided adequate information to the clinicians to extract velocity-time plots.

Notable differences also occur in the measured diameters of the innominate with the pre- and post-intervention diameters being $8.15\ mm$ and $6.98\ mm$, respectively, which represents a 14% change. It should be noted that the locations at which these measurements are taken, do not visually agree and so these two measurements may not be related.

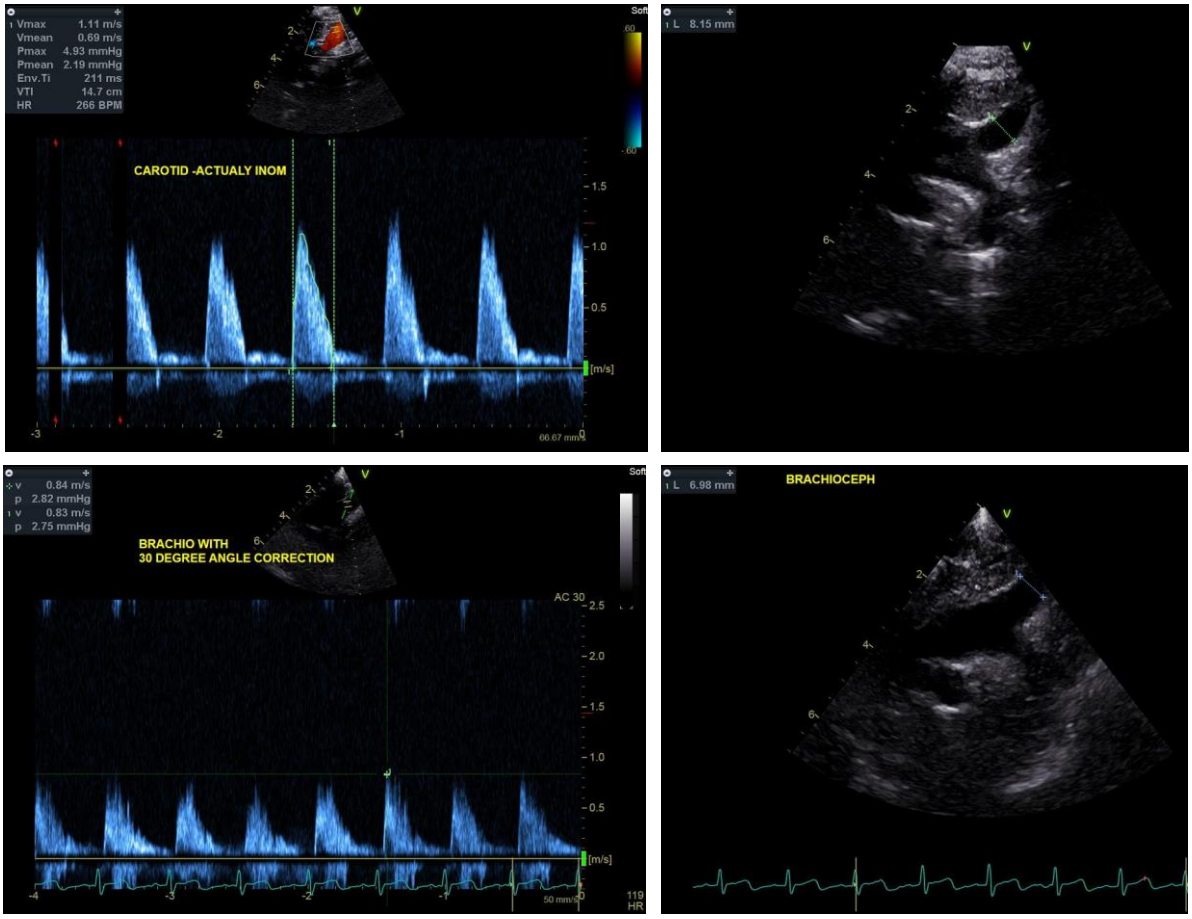

Figure 5-9: Innominate echocardiography results for both pre- (top row) and post- intervention (bottom row) instances.

Left Common Carotid

The importance of clinician feedback of the experience during the investigation is highlighted in this measurement. Although echocardiography is a non-invasive imaging modality, the probe can still cause discomfort when pressed to the skin. In small children, and indeed this case, restlessness and discomfort during the post-intervention investigation created a challenge to the clinician to obtain steady and reliable flow data. This is an important consideration when choosing whether to implement echocardiography as an imaging modality. Nevertheless, the pre-intervention study shown in Figure 5-10 yielded good velocity results which showed a peak velocity of $0.81\ m.s^{-1}$. Again, there was a lack of ECG supplemented heart rate data.

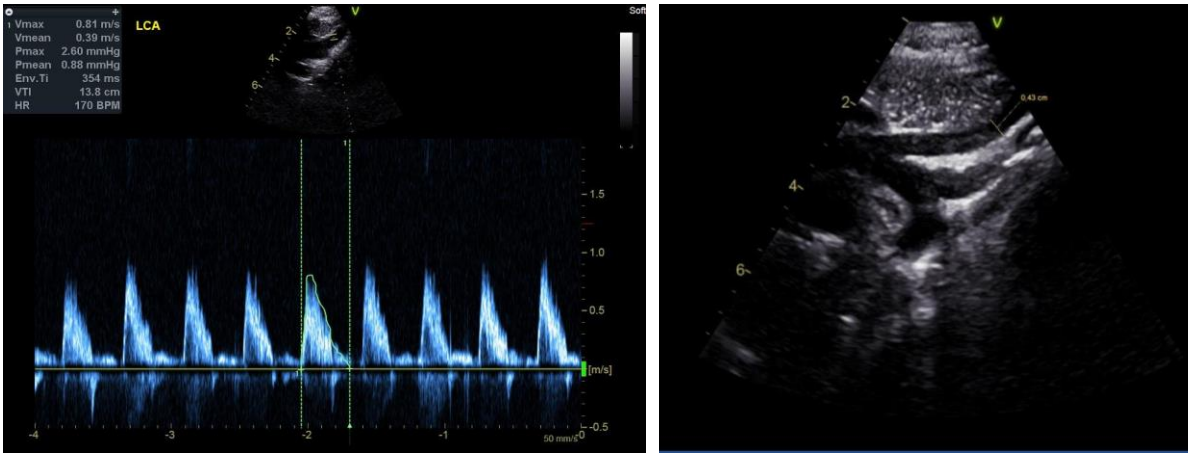

Figure 5-10: Left Common Carotid echocardiography results from a pre-intervention investigation only as a post-intervention measurement was not possible.

Left Subclavian Artery

The post-intervention velocity measurements for the LSCA vessel were not possible due to patient restlessness, hence, only pre-intervention data could be collected. The pulse wave doppler study shown in Figure 5-13 was conducted and without ECG derived heart rate information in this case. The pre-intervention measurement of the velocities in the LSCA was noisy and showed spurious intensities in some locations. However, the quality of data was sufficient for the clinician to extract a velocity-time plot over a cardiac cycle. The peak systolic velocity is reported as $0.70\ m.s^{-1}$and the diameter of the vessel was measured to be approximately $5.00\ mm$.

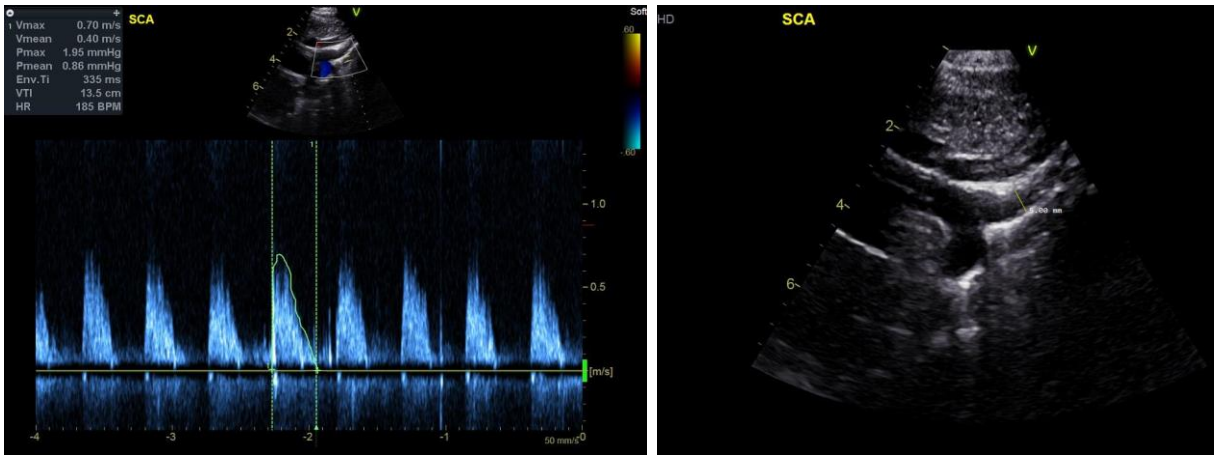

Figure 5-11: Left Subclavian echocardiography results from a pre-intervention investigation only as a post-intervention measurement was not possible.

Coarctation Zone

Coarctation flow and geometry data was obtained through continuous wave doppler echocardiography for both cases and the results are shown in Figure 5-12. In addition, the data quality was good in both cases, due to the alignment of the probe line and the direction of blood flow. This resulted in a clean velocity profile that was extracted in both cases.

The stark differences in the velocity profiles is indicative of the positive outcome of intervention. The pre-intervention waveform shows flow through the coarctation that continues through the majority of diastole. This diastolic tail is an indicator of the severity of the coarctation and in the post-intervention data, it can be seen to have completely dissapeared. Furthermore, the peak velocity through the coarctation reduces from $3.49\, m.s^{-1}$ to $2.38 m.s^{-1}$, which is a 31.8% absolute change relative the pre-intervention velocity.

It is in this region that the P_{max} pressure measurement calculated during the study was relevant. Due to the simplicity of the modified Bernoulli equation in Eq 3.1, there is likely to be error in the value, however, without catheter pressure measurements, this derived pressure gradient is the sole benchmark that was available for verification of the CFD calculated pressure gradient. The maximum pressure change which coincides with the peak velocity is reported as $48.65\, mmHg$ and $22.72\, mmHg$ in the pre- and post-intervention instances respectively. This represents a 53.2% change. The coarctation diameter was extracted for the post-intervention geometry and found to be $6\, mm$. The measurement was not taken for the pre-intervention case and so the CTA data was rather relied on for verification.

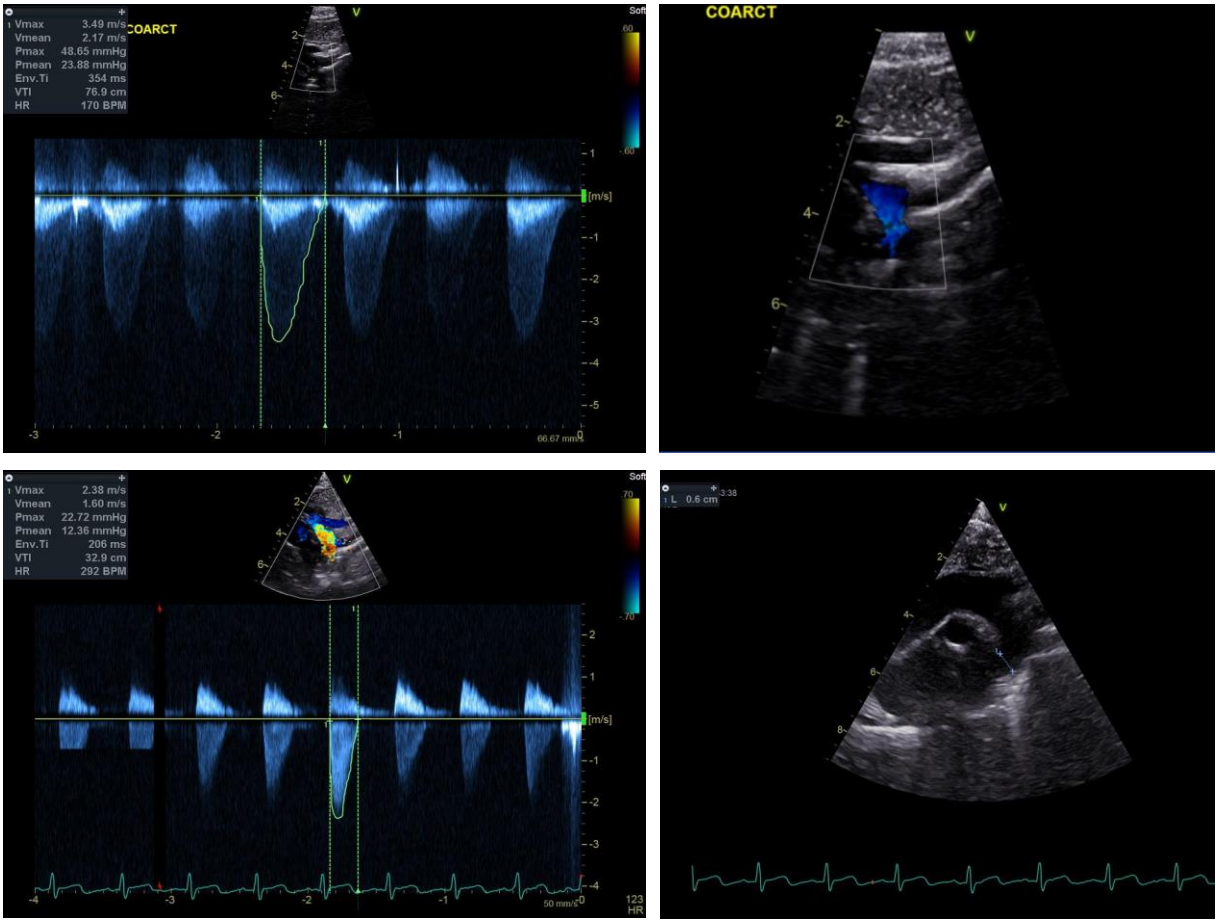

Figure 5-12: Coarctation zone echocardiography results for both pre- (top row) and post-intervention (bottom row) instances

Descending Aorta

As with previous cases, the descending aorta was another location where patient restlessness was prohibitive, resulting in pre-intervention data only, as shown in Figure 5-13. Although a plot for the velocities over the cardiac cycle was obtained, the noise levels in the profile were high, as seen by the spurious peaks seen in Figure 5-13. A profile was extracted by the clinician and the peak velocity was found to be $0.63\ m.s^{-1}$. In addition, the diameter of the descending aorta, as measured on the ultrasound image, was approximately $8.29\ mm$.

In considering the dataset as a whole, it can be seen that there are inherent challenges in the use of doppler echocardiography for the extraction of patient-specific flow data. What was extracted was suitable for posing the computational problem of case 1 completely but could only partially define the problem for case 2. At the locations where data was missing, extrapolations and/or derivations of the data would be required to define the problem completely. The key data which was taken from the echocardiography data set is summarised in Table 5-3.

The manner in which this data was processed to derive and define boundary conditions for the final flow simulations was an important part of the study, as it enabled assessment of the impact of various assumptions on the results. The approach which most closely reproduces the key metrics of maximum velocity and pressure gradient through the coarctation was considered the most suitable for the CFD model.

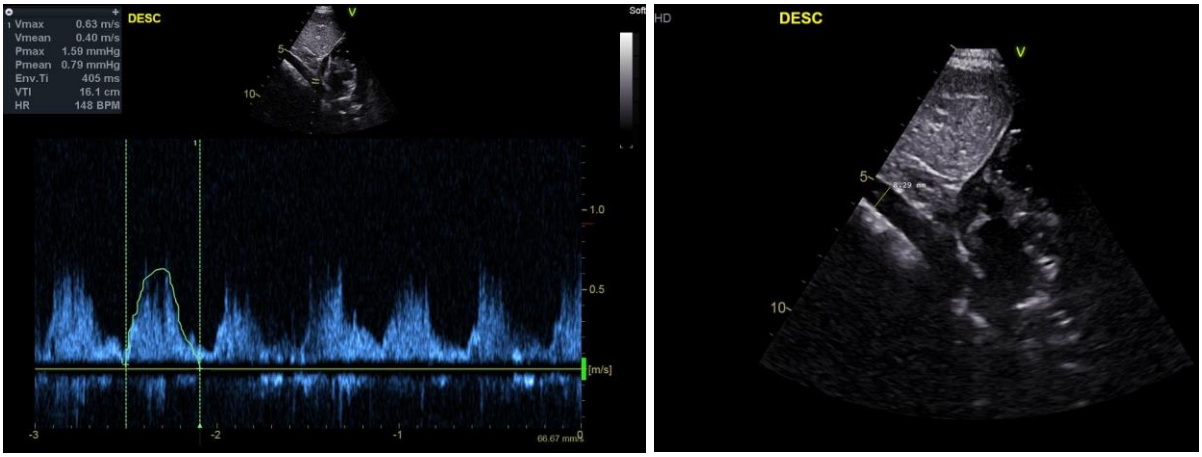

Figure 5-13: Descending aorta echocardiography results from a pre-intervention investigation only as a post-intervention measurement was not possible.

Table 5-3: Collation of relevant data that was acquired and utilised from echocardiographic imaging

Location	Max Velocity (m/s)	Mean Velocity (m/s)	Max Pressure (mmHg)	Measured Diameter (mm)
CASE 1				
Ascending Aorta	1.3	0.64	6.80	13.00
Innominate	1.11	0.69	4.93	8.15
LCCA	0.81	0.39	2.60	4.30
LSCA	0.70	0.40	1.95	5.00
Coarctation	3.49	2.17	48.65	-
Descending Aorta	0.63	0.40	1.59	8.29
CASE 2				
Ascending Aorta	1.3	0.76	6.76	11.21
Innominate	0.84	-	2.82	6.98
Coarctation	2.38	1.60	22.72	6.00
LCCA	-	-	-	-
LSCA	-	-	-	-
Descending Aorta	-	-	-	-

Echocardiography Derived Reynolds Numbers

Table 5-4: Table calculating mean (m) and peak (p) Reynolds numbers for each acquired doppler echocardiography measurement.

Location	Max Velocity (m/s)	Mean Velocity (m/s)	Measured Diameter (mm)	Kinematic Viscosity (m^2/s)	Re_m	Re_p
			CASE 1			
Ascending Aorta	1.3	0.64	13.00	3.77e-6	2206.90	4482.7
Innominate	1.11	0.69	8.15	3.77e-6	1491.64	2399.60
LCCA	0.81	0.39	4.30	3.77e-6	444.83	923.87
LSCA	0.70	0.40	5.00	3.77e-6	530.50	928.38
Coarctation	3.49	2.17	3.37 **	3.77e-6	1939.76	3119.71
Descending Aorta	0.63	0.40	8.29	3.77e-6	879.58	1385.33
			CASE 2			
Ascending Aorta	1.3	0.76	11.21	3.77e-6	2259.84	3865.52
Innominate	0.84		6.98	3.77e-6		1555.23
Coarctation	2.38	1.6	6.00	3.77e-6	2546.42	3787.80

*** Note that this measurement, as described above was taken from the segmented geometry analysis in Table 5-1 as it is not available from echo measurements but necessary for the Reynolds number calculation.*

The Reynolds number as calculated in Table 5-4 can be used to estimate the flow regimes at several locations in the domain and so provide an indication of whether a turbulent model should be used or not. It can be seen here that the mean Reynolds number (Re_m) remains either within a laminar or lower transitional regime although this is juxtaposed with the peak Reynolds number (Re_p) which are predominantly in the region of being transitional according to the ranges indicated in [84].

The mean and peak Reynolds numbers at the coarctation, in case 2 seems to be an outlier given that the flow would not be expected to become more turbulent after an expansion of the stenosis. This should be investigated further as it could be a measurement error or the result of a non-trivial physiological response of cardiac output to the relieved stenosis.

Given that mean Reynolds numbers are predominantly laminar or lower-transient, this study proceeded to implement a laminar model in order to give a first approximation and to complete the pipeline prototype. At a later stage it was aimed for studies to build on the model by incorporating a turbulence model.

Echocardiography Derived Womersley Numbers

Table 5-5: Womersley number analysis using post-repair data each case.

Location	Measured Diameter (mm)	Kinematic Viscosity (m^2/s)	*fr* (cycles/s)	Wo
Ascending Aorta	11.21	3.77e-6	1.92	10.02
Innominate	6.98	3.77e-6	1.98	6.35
Coarctation	6.00	3.77e-6	2.05	5.55

Table 5-5 calculates the Womersley numbers from the post-repair doppler echocardiography measurements at the ascending aorta, innominate artery and site of the coarctation repair shown in Figure 5-8, Figure 5-9 and Figure 5-12 respectively. Only this data could be used due to the inclusion of reliable ECG measurements of heart rate. This was adequate due to the relative consistency of the measured heart rates which deviate minorly above or below 120 BPM. As can be seen, the Womersley number in each case is greater than 1 which indicates that there is a deviation from a quasi-steady state as discussed in section 3.6.3.

The Womersley number in this case indicates that the pulsatility of the flow in the case of the patient in this study contributes to a higher complexity of flow which may not be adequately captured in a steady-state simulation. However, the drive towards clinically feasible data output timeframes motivated the decision to conduct a steady-state simulation. In addition there was an overarching intention for this study to act as a pilot study that would be able to lay out a basic pipeline for future development and so one would start with a steady inflow simulation before adding the complexity of transient simulations.

5.4 DOPPLER ECHOCARDIOGRAPHY DATA PROCESSING STUDY

A potential drawback of the doppler echocardiography modality is generated by three factors:

- The discontinuity in time of measurements at each site
- Restriction to velocity magnitudes with binary direction indications in the plane of the probes field of view
- Variation in heart rate for each measurement

These factors translate to difficulties in extracting accurate volumetric flow rate data. Assumptions had to be made in the following processing methods to account for the variations in the patient's heart rate at the time of each measurement. It must be noted that these do not account for physiological effects that variations in heart rate have on the velocity waveforms.

Four methods of data processing were implemented, and the results compared to assess accuracy. These adjustment schemes were driven firstly by the logic that the peak inlet volumetric flowrate and the peak sum of outlet volumetric flowrates should match, since mass would otherwise be generated artificially. Secondly, because of an incompressible fluid and rigid wall assumption, there was the need for peak flow at each outlet to occur at the same time as the peak inlet flow rate. After data smoothing and the application of the relevant adjustment scheme, each volume flow rate and velocity profile was plotted on the same axis for comparison and analysed below. It should be noted that by the fact that these methods are only implemented on a single case, the author does not recommend these as generally applicable but, it suggests the need for further investigation so that a general approach can be derived.

5.4.1 Data Processing Study Results

5.4.1.1 No Data Adjustment

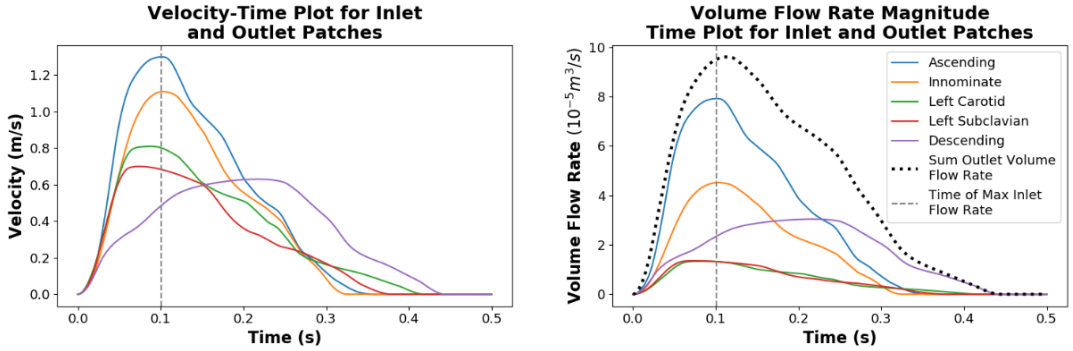

Figure 5-14: Plot showing velocity vs time (left) and volume flow rate vs time (right) for the inlet and each outlet patch over one cardiac cycle. The peak systolic volumetric flow rates were taken at the vertical dotted line.

Figure 5-14 shows the first approach to data processing which directly implemented the echocardiography data after being digitised, scaled in time to match a heart rate of $120\ BPM$ and smoothed. It is important to note that in the plot of volumetric flow rate vs. time, the sum of the volumetric flow rates at the outlet patches is not equivalent to the inlet volumetric flow rate based on an assumption that the average velocity at the inlet would be half of the maximum velocity and that the average velocity at the outlet is the same as the maximum velocity. The sum of the outlet profiles, although exceeding the inlet plot, seems to have an equivalent form to the inlet volumetric flow rate profile. The misalignment of amplitudes justifies the investigation into the adjustment of each outlet profile through scaling the volumetric flow rate component.

The volumetric flow rate through the LCCA and LSCA outlet patches was found to be similar in magnitude and systolic flow duration. Finally, by adjusting each profile's period to that relating to $120\ BPM$, all the profiles, besides the descending aorta outlet, followed a similar cycle of flow where flow begins and ends at about the same time point. This begins as the valve opens in systole and ends with the inlet flow profile as the valve closes during diastole.

Although each outlet plot starts with systole and ends at approximately the same time at the start of diastole, the peak flow rates for the LSCA and LCCA lead and the innominate lags the inlet plot. In addition, the flow rate through the innominate outlet patch ceases prior to the end of systole as indicated by the inlet flow rate profile. This justifies investigating the adjustment of the phase of each profile relative to the inlet flow rate profile. Furthermore, the inconsistency in the phase between the supra-aortic branches points to the possibility that, through digitising or by not accounting for the physiological effect of different heart rates, error was introduced.

5.4.1.2 Amplitude Adjusted Data

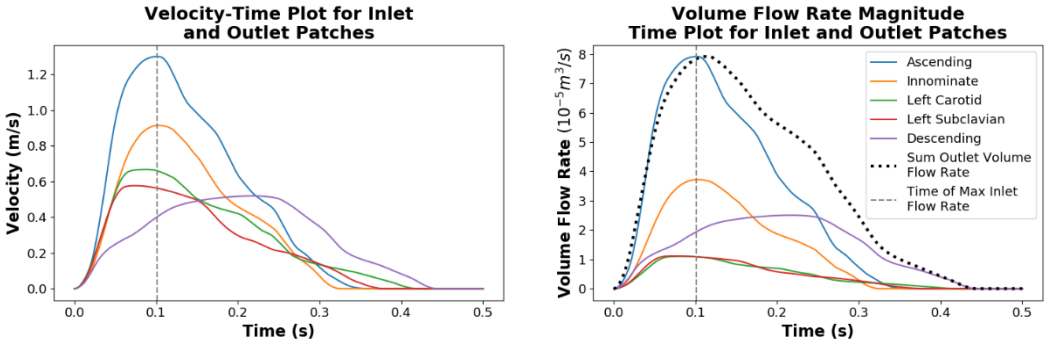

Figure 5-15: Plot showing velocity vs time (left) and volume flow rate vs time (right) for the inlet and each outlet patch over one cardiac cycle. The peak systolic volumetric flow rates were taken at the vertical dotted line.

By scaling the amplitude of each outlet by the same factor, it was possible to avoid the paradox whereby the peak volumetric outflow was higher than inflow, as seen in the previous case. This was seen to be an important approach so that mass conservation was not violated at the time where peak systolic inlet flow occurred. It was found that a scale factor of 0.8243 for each outlet patch was required for each outlet, so that the peak value of the sum of the volumetric flow rate outflows and the inflow were equal as can be seen in Figure 5-15.

One can see that during systolic acceleration of flow, the profiles were similar however in the late acceleration phase and onwards through diastole the sum of outflow lags the inflow profile. This indicates that, although the peak values were the same, it is possible that, over a cardiac cycle, mass conservation is not followed.

5.4.1.3 Phase Adjusted Data

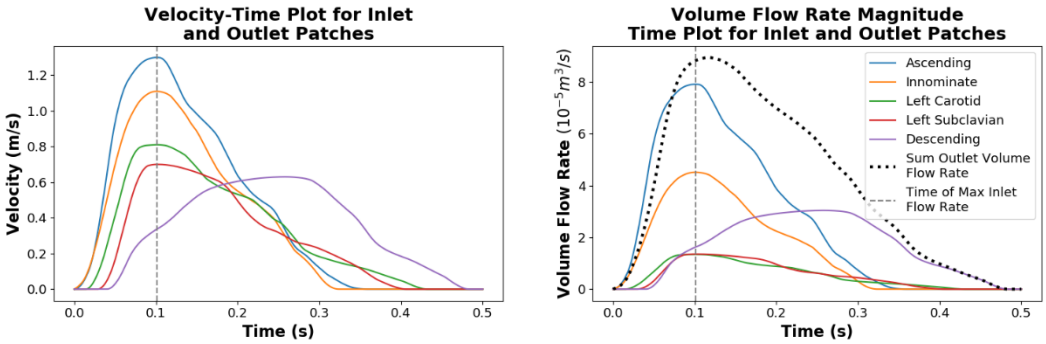

Figure 5-16: Plot showing velocity vs time (left) and volumetric flow rate vs time (right) for the inlet and each outlet patch over one cardiac cycle. The peak systolic volumetric flow rates were taken at the vertical dotted line.

In digitising the echocardiography velocity-time plots over a cardiac cycle, it was found that the peak volumetric flow rates at the supra-aortic vessel outlets were not in phase with the peak inlet volume flow rate. Due to the coarctation, the flow through the descending aorta outlet was understandably not aligned with the inlet. However, it seemed unrealistic that the flow through the LCCA and LSCA would lead the flow at the inlet, particularly in light of the capacitive effect of the artery distensibility.

The wave forms shown in Figure 5-16 of the flow through the innominate, LCCA and LSCA were phase adjusted such that the peak flow rate at the supra-aortic branch outlets aligned with the peak flow rate at the ascending aorta. Interestingly, the result was that the start of the flow of each vessel corresponded with the order in which they occurred along the centreline of the arch. To keep with this trend, the descending aorta flow profile was phase shifted so that flow began after the LSCA flow. Table 5-6 collates each flow profile's phase shift.

It is important to note that, despite the phase shifting, mass conservation violations persist in that the sum of the outflow reaches a higher peak flow rate value than the inlet flow rate. In addition, the sum of the outlet flows is lagging the inlet volumetric flow rate for the duration of the cycle.

Table 5-6: Collation of the phase shift for the flow profile at each outlet patch

Outlet Patch	Phase Shift
Innominate	-0.002
LCCA	+0.014
LSCA	+0.0285
Descending Aorta	+0.04

5.4.1.4 Amplitude and Phase Adjusted

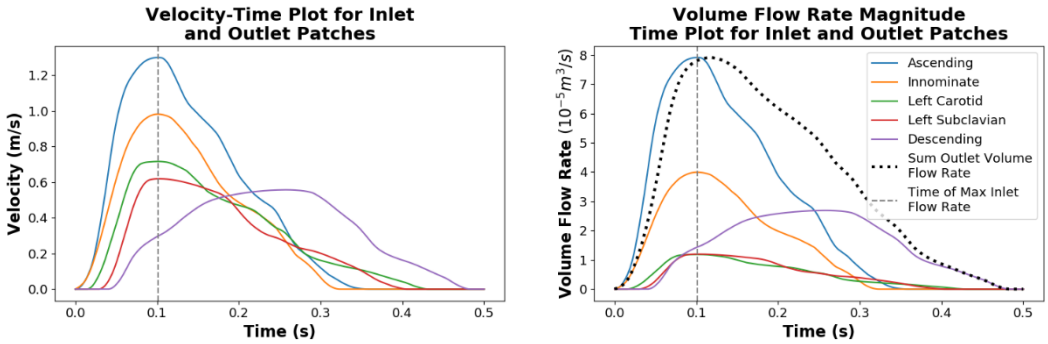

Figure 5-17: Plot showing velocity vs time (left) and volumetric flow rate vs time (right) for the inlet and each outlet patch over one cardiac cycle. The peak systolic volumetric flow rates were taken at the vertical dotted line.

To align both the phase and amplitude of the peak flow rate at each outlet as well as the peak value of the sum of outlet volumetric flow rate, the phase of each outlet flow profile in Figure 5-17 and the amplitude was shifted and scaled, respectively.

The phase shift values remained equivalent to the previous study however, due to this change in relation to the amplitude adjusted only case, the outlet amplitudes only had to be scaled by 0.8845. Again, the sum of the outlet flow rates lagged the inlet flow rate profile although the peak flow rate was equivalent.

For a steady state, peak volumetric flow rate CFD study, the values to be applied at each outlet and the inlet boundary patch were determined by selecting the values of each profile at the point in time where the peak of the inlet flow profile occurred. This time was found to be 0.101 s and the corresponding volumetric flow rates for each method of data processing and each outlet flow profile are collated in Table 5-7.

5.4.1.5 *Zero-Pressure Study*

A zero-pressure outlet boundary condition for aortic simulation flows has been used in various simulations in the past and proven to be insufficient [33]. In this study it was included so as to assess how the boundary condition performed in a stenosed aorta case. If an easy to apply boundary condition such as a zero-pressure at the outlet would be sufficient to estimate the pressure gradient, then that would vastly improve the clinical feasibility of the pipeline. It should be noted that applying non-zero pressure outlet boundary conditions is possible but, without pressure measurements for the patient studied here, it would be unfeasible to predict or guess the correct value to apply.

Table 5-7: Table collating the volumetric flow rate values for each patch at the time of peak inlet volumetric flow rate. These values were then applied as boundary conditions for CFD simulation and the inlet volumetric flow rate was set as the sum of the outlet volumetric flow rates.

Patch	Not Adjusted	Amplitude Adjusted	Phase Adjusted	Phase and Amplitude Adjusted	Zero Pressure
Inlet	9.50	7.84	8.83	7.81	7.92
Innominate	4.51	3.72	4.52	3.99	-
Left Carotid	1.32	1.09	1.34	1.18	-
Left Subclavian	1.32	1.09	1.35	1.20	-
Descending Aorta	2.35	1.94	1.62	1.44	-

5.4.1.6 ***CFD Results for Each Flow Profile Processing Approach***

The key metrics that were taken away from each study were the maximum velocity and the pressure gradient across the coarctation. A qualitative comparison can be made by comparing the pressure and velocity magnitude field plots in Figure 5-18 and Figure 5-19. Besides the zero-pressure outlet boundary condition case, the qualitative comparison of each of these studies shows that the distribution of the pressure and velocity fields stays relatively consistent with regards to the high-pressure regions in the ascending aorta and aortic arch and maximum velocities in the constricted zone of the coarctation (although with changes to global maxima and minima). A point of interest is in the flow pattern generated near the outlet of the descending aorta. In the unadjusted case, there seems to be higher levels of disorder illustrated by the green contour regions in each velocity plot.

A quantitative comparison of maximum velocity in the coarctation zone as well as the pressure gradient is presented in Figure 5-20 and Table 5-8. This allowed for the assessment of each adjustment method from which stark differences in the outcome are clearly shown. The amplitude adjusted profiles were found to result in the smallest velocity error. It is key to see at this point that, according to the metrics of the pressure gradient and velocity through the coarctation, the zero-pressure outlet boundary condition has significant error associated with it and is thus considered to have performed the worst out of all of the proposed outlet boundary condition settings. Adjusting the phase significantly affected the accuracy and adjusting both the phase and amplitude in conjunction results in the worst outcomes of the volumetric flow rate boundary conditions.

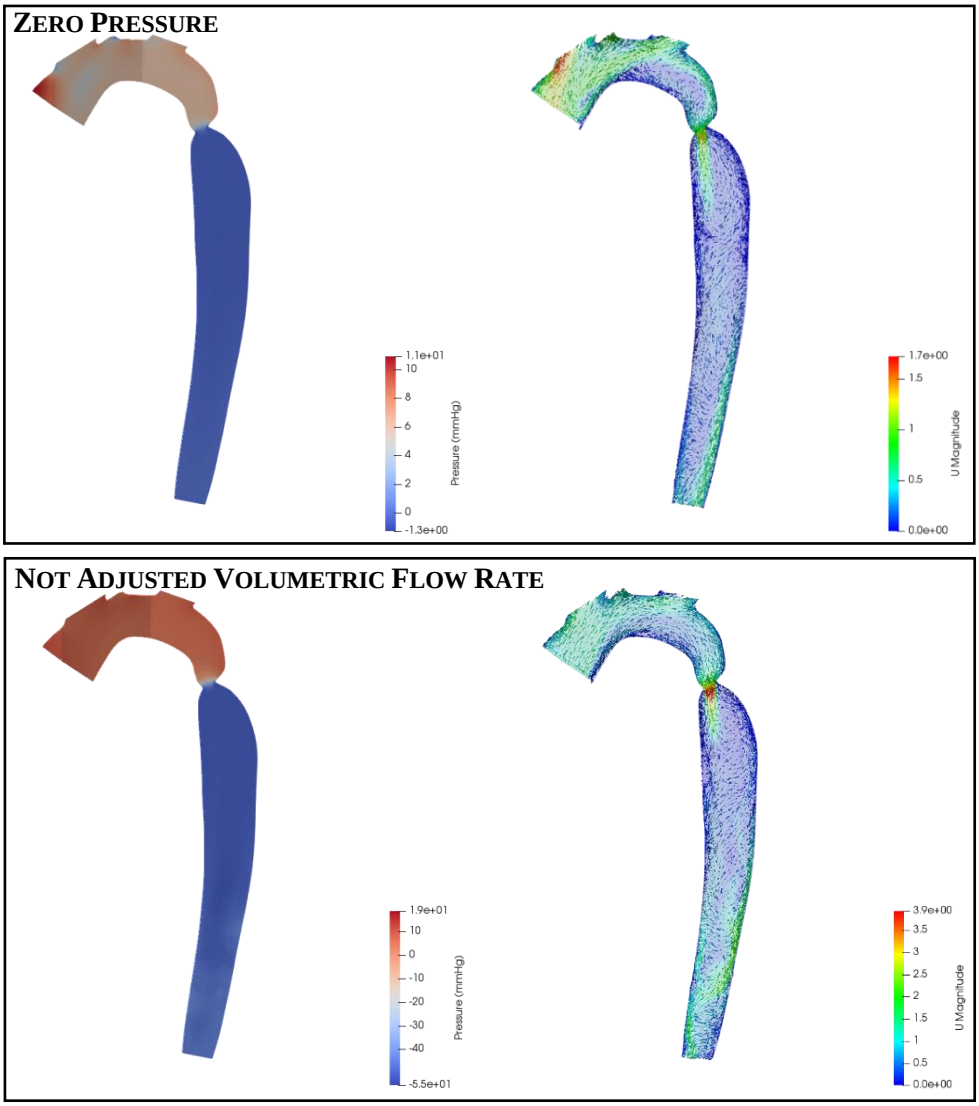

Figure 5-18: Slice to depict features of the velocity magnitude and pressure fields of the simulation where zero pressure and the no-adjustment scheme for volumetric flow rate processing was applied.

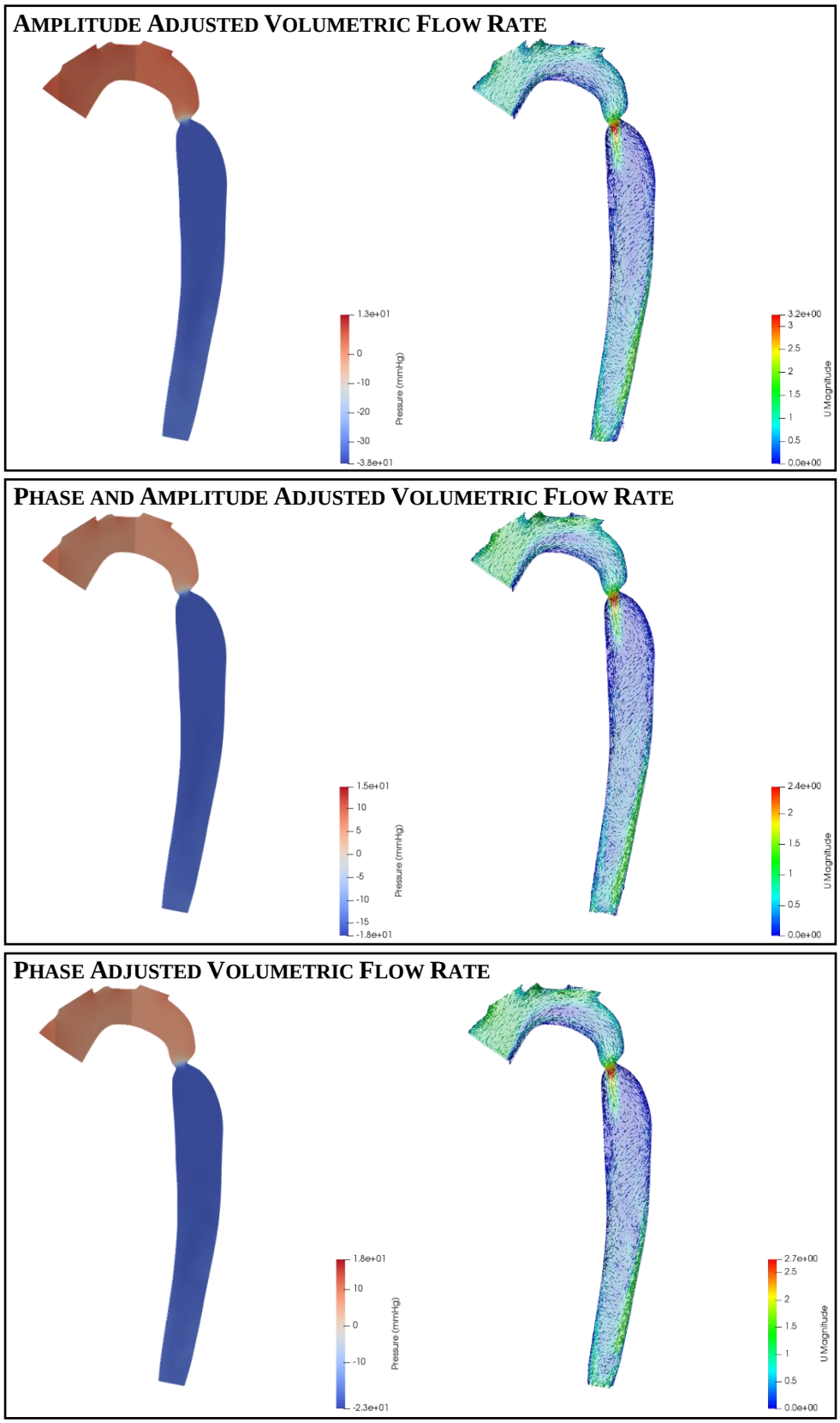

Figure 5-19: Slice to depict features of the velocity and pressure fields of the simulation where echo data was amplitude adjusted, phase and amplitude adjusted and just phase adjusted.

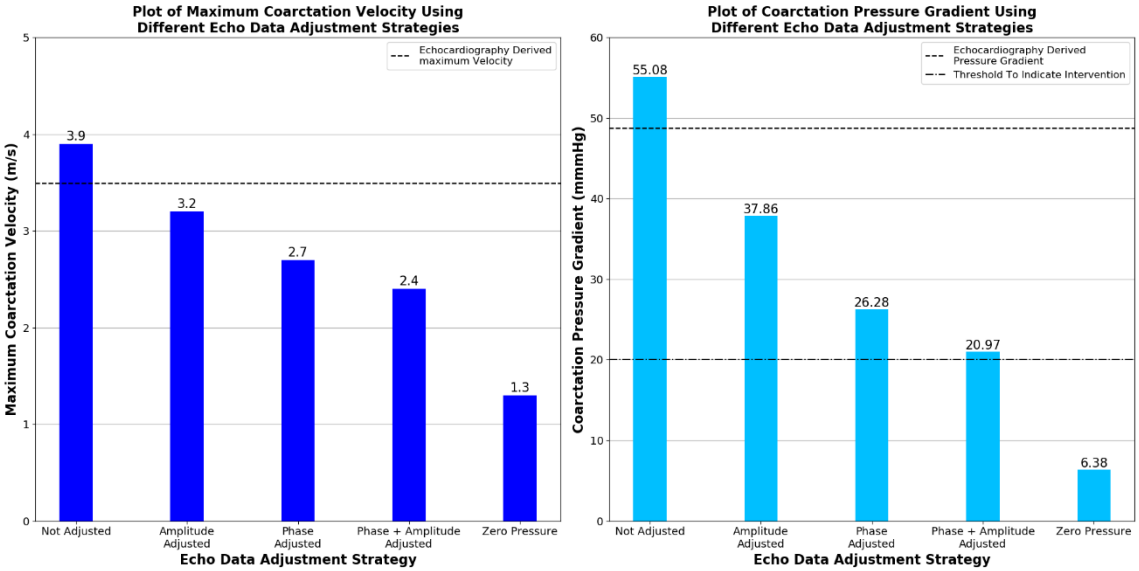

Figure 5-20: Graphical comparison of the pressure gradient (right) and peak coarctation velocity (left) with echo measurements in the pre-repair case as a result of applying the different data adjustment schemes and zero pressure boundary condition. In the pressure gradient plot, the threshold for the indication of an intervention is also shown.

Table 5-8: Tabulation of the key metrics used to compare the approach towards data processing. The baseline Doppler Echo pressure measurement is an estimate based on the modified Bernoulli's equation.

	Velocity		**Pressure**	
	Coarctation Velocity	**Velocity Error**	**CFD Coarctation ΔP**	**ΔP Error**
Doppler Echo Baseline	3.49	-	48.65	-
Not Adjusted	3.92	11.7%	55.08	13.2%
Amplitude Adjusted	3.24	-8.3%	37.86	-22.2%
Phase Adjusted	2.73	-22.6%	26.28	-46.0%
Phase + Amplitude Adjusted	2.43	-31.2%	20.97	-56.9%
Zero Pressure	1.30	-62.8%	6.38	-86.9%

5.4.2 Data Processing Study Discussion

Doppler Echocardiography Data Acquisition

The results of the process of obtaining and assessing the echocardiography data which was presented in section 5.3.1.1 served two purposes. Primarily, this data would be used for defining the boundary conditions for the CFD simulation of flow in each case. In parallel to this, the collaboration with clinicians to develop the data collection protocol, obtain the data and assess its quality allows for the evaluation of the advantages and disadvantages of using echocardiography as a modality for data collection. The data which resulted out of the developed protocol should thus be evaluated with respect to the intended use for boundary condition definition. In conjunction, there must be a constant awareness of how these results bear on determining the viability of doppler echocardiography as a flow imaging modality in low and lower-middle income countries.

The pre-intervention echocardiography data that were presented in Figure 5-8 through to Figure 5-13 proves that echocardiography was capable of obtaining flow and geometry data to be used in defining the boundary conditions at each inlet and outlet patches of an aorta model. In each pre-intervention location, it was possible to trace the velocity-time plot over a cardiac cycle. The crucial contribution from the echo data to conducting the patient-specific CFD study was this velocity data.

Echocardiography has important advantages which make it attractive as a modality for patient-specific CFD data collection protocols, as was experienced in this study. Apart from its high spatial and temporal resolution, the most important advantage that echocardiography holds over CTA and MRI is the ease with which it can be applied, and the low risk associated with it. This was a particularly important factor in developing and implementing the protocol as it would be necessary to repeat investigations at various points in time. Ethically, it was not justifiable to subject an infant to the radiation of repeated CTA scans nor to sedate them for the time required to conduct a cardiac MRI scan, only to obtain data which could be obtained from echocardiography. Echo has relatively low time constraints in terms of its scheduling. This was found to be beneficial when the time between the CTA scan and the echo investigation had be minimised. In addition, it could be easily conducted during standard clinical care and when the patient returned for follow up consultations.

It is evident that the spatial and temporal resolution of echocardiography is superior to that of the CTA data. In each example shown in Figure 5-8 through to Figure 5-13, there is a definitive boundary between the blood pool and vessel walls at each point of the aorta. Segmentation using echocardiography is possible [93], however, was out of scope of this study. Nevertheless, the measurements of vessel diameters at key locations in the domain along with

the visual aid of the ultrasound image is a useful tool to supplement, guide and verify the segmentation of the CTA data. To add to the qualitative verification of the segmentation in section 5.2.1, Table 5-9 shows the comparison between the vessel diameter measured in the echocardiograph images and the hydraulic diameters calculated from the cross sections of the segmented geometry at each outlet and inlet patch as well as the coarctation.

Table 5-9: Comparison of the geometry measured diameters from echocardiograph data and calculated hydraulic diameters from the segmented geometry

	Hydraulic Diameter	**Measured Diameter**	**% Error (Relative to Measured D)**
Ascending Aorta	12.45	13.00	-4.2
Innominate	7.18	8.15	-11.9
LCCA	4.57	4.30	6.3
LSCA	4.93	5.00	-1.4
Coarctation (Post-Intervention)	5.76	6.0	-4.0%
Descending Aorta	7.83	8.29	-5.5

The average percentage error based on the values presented in Table 5-9 was found to be 5.86%. This calculation includes the outlier of the measurement for the innominate artery diameter and if this value were not to be considered in the average error calculation, the percentage error decreases to 4.35%. The contributions to this error are expected to come from segmentation error, malalignment of the locations where the diameters were measured and in the simplifying assumption of circular cross sections of the vessels by using the diameter directly from the 2D echo view. The malalignment factor is seen to be the chief contributor to the reason the innominate error value is an outlier due to the tapering that is seen in the artery between its arch junction and outlet patch. Overall, the average error excluding the innominate outlet is within an acceptable 5% upper bound. There is reason to believe that, by adjusting the location of the echocardiograph diameter measurement, the error would be reduced.

In general, there is a lack of MRI facilities in low and lower-middle income countries. In comparison, echocardiography is a highly mobile and widespread imaging modality which makes it a key tool to use in order to unlock the implementation of patient-specific CFD studies more broadly. The use of echocardiography as the velocity investigation technique was truly indispensable in the case where CTA and MRI investigations were limited due to safety, ethical and logistical reasons. Even though echocardiography is applied in a wide range of

contexts, there are some disadvantages that necessitated further adjustment of the data to enable implementation of sensible boundary conditions.

The quality of echocardiography is widely known to be dependent on the patient restlessness, as well as the skill level of the operator. For most coarctation cases, the investigation is relatively quick with the intention to collect data at the ascending aorta and the coarctation only. However, this study required far more data in locations that were possible, albeit non-trivial, to obtain. One only needs to consider the contrast in success of collecting a full dataset from the pre-intervention to the post-intervention cases to see how the success of obtaining the required data can vary from one investigation to the next.

Clinician feedback in the pre-intervention case reported that the patient fell asleep and did not resist being positioned optimally to obtain clear views of vessels. In contrast, the patient was awake and restless during the post-intervention study, which only allowed for some of the required data to be collected. In a broader implementation of this protocol, it should be expected that several different members of staff would be carrying out the protocol and so it should be anticipated that the level of skill by different clinicians adds a variable to the protocol.

As has been noted in previous chapters, doppler studies are able to compensate, through trigonometric calculations, for the angle between the probe and blood flow. In the case where the angle between the flow direction and the probe are greater than 60^{O}, the trigonometric calculation becomes unfeasibly inaccurate. In most of the cases shown in Figure 5-8 through to Figure 5-13, it was not possible to perfectly align the probe to the flow and so angle correction was necessary, however, in none of the cases was this angle found to be greater than 60^{0} which would invalidate the results. The assessment of the measurements by the clinical team was important to judge the quality of the resulting data. The velocity data that was obtained was deemed adequate and so proceeded to be applied as boundary conditions, but a healthy level of scepticism was maintained regarding the pressure gradient metrics that were measured through echocardiography.

The pressure gradient metric is based on a modified Bernoulli equation described in section 3.1.1 and described by Eq 3.1. In contrast, CFD calculates pressure through the more accurate Navier-Stokes equations. This is not to say that the pressure drops calculated by echocardiography (particularly in the region of the coarctation) were not useful. These values were important in giving a benchmark for the CFD derived pressure gradient.

In the finite volume method, pressure and velocity cannot be prescribed at the same point. One must be calculated as a consequence of the other and so, in this study where echocardiograph

gave reliable velocity data and only an estimation of the pressure gradient, the assessment of the CFD result was rather based on the velocity achieved and, as a secondary but non-driving assessment, the pressure gradient.

In this case, where the cardiac structures were normal and the skill of the echocardiographers were high, the issue of probe and flow alignment was surmountable. However, variations in patient geometry, patient amicability and operator skill would be expected in forthcoming cases, which could contribute to inconsistency of resulting data in both quality and availability. This inconsistency has been one of the driving factors for researchers with more advanced facilities to move towards PC-MRI. However, dealing with this inconsistency should be seen as an important aspect of developing an appropriate methodology, especially because of the importance that echocardiography would hold in applying this protocol in other countries with limited clinical resources.

Doppler Echocardiography Data Processing

The velocity data that was generated in the previous section required processing in order to be applied as volumetric flow rates at each outlet and the inlet patch. The two primary drivers for conducting this study were based on the fact that each echo dataset showed evidence of other velocity signals (by way of intensities being shown below the velocity-time plot) over the cardiac cycle. These appeared as intensities below the velocity-time plot line. In addition, it was unlikely that the heart rate for each study was the same. Thus, on the former point, it was first seen as improbable that the maximum velocity which constituted the velocity-time plot was equivalent to the average velocity at that cross section. In addition, the profiles may vary with heart rate despite their period being scaled to a common value. Without ECG, one could not be certain of how each profile started and ended relative to the others. Thus, four approaches to processing the velocity data were tested. The results illustrate the drastic effect that the choice of method can have on haemodynamics, even when judged solely on the coarctation velocity and pressure gradient information drawn from the corresponding echo study.

The quantitative comparison was based on the doppler echocardiography measurements of the maximum velocity in the coarctation region as well as the pressure gradient across the coarctation. It can be seen in the error analysis shown in Table 5-8, the best performing processing protocol in terms of the peak velocity in the coarctation region was the amplitude adjusted volume flow rates scheme (Figure 5-15). The simulation predicted a maximum velocity of 8.3% less than the echo measured value. In considering the pressure gradient calculation, however, the best approach was the processing scheme which did not adjust the flow profiles at all. This resulted in an error of 13.2% greater than that calculated by the

doppler study. The amplitude study underestimated the pressure by a margin of 22.2%. However, Table 5-4 shows that flow may enter a transitional turbulent regime at the site of the coarctation. The laminar model may, in this case, underestimate the true pressure drop which indicates the importance of later work to explore the addition of a turbulence model.

As stated previously, the strength of an echocardiography study is in the velocity measurements. Thus, the comparisons that were made between the maximum velocity found in the simulation and those obtained in the doppler study carried more weight than the comparison between the pressure gradients. It should be emphasised that the CFD calculated pressure gradient was still required to reflect a pressure gradient that was indicative of the severity of this coarctation as well as result in the same clinical decision to intervene or not. Each of the CFD studies did indicate that intervention was required, by showing a pressure gradient that was greater than the clinically established $20\ mmHg$ standard. However, the amplitude and phase adjusted scheme cleared this benchmark by a small margin which would significantly decrease the perception of the severity of this coarctation. For a severe coarctation, such as the one seen in case 1, this result could not be accepted as being adequately representative.

In considering the top performing adjustment scheme as well as the criteria which may dismiss an adjustment scheme, it is evident that the adjustments to the phases of each outlet profile relative to the inlet profile did not serve as an adequate approach towards processing the echo velocity data. In fact, the amplitude adjusted plots gave the most accurate velocity value while still giving a pressure gradient which indicated that intervention was required. Not adjusting the data at all overestimated the velocity through the coarctation and thus also overestimated the pressure gradient. By considering the data summarised in Table 5-7 in conjunction with the data presented in Table 5-8, it can be seen that there is a correlation between the volumetric flow rate through the descending aorta outlet patch and the values calculated for pressure gradient and maximum coarctation velocity. This agrees with Bernoulli's equations that show the direct correlation between fluid velocity (and so volumetric flow rate) and the driving pressure gradient. This indicates that, if using the echocardiography value as the standard for velocity measurements, it would be possible to scale and tune the outlet volumetric flow rates to achieve the required velocity at the coarctation zone.

The need to scale and adjust each profile was driven by the fact that there was a violation of continuity at each time-step. It is known that aorta distensibility inherently violates instantaneous continuity laws, however, this is not enough of a contributing factor to explain the extent to which continuity violations occur. It has been noted in section 5.4.1.1 that by using the maximum velocity trace from the doppler echocardiography measurements at each

location to derive volumetric flow rates, one assumes a plug velocity profile at that location. This is evidently not the case and so the error in this assumption is evident by the need to scale all of the velocities by a factor less than one to achieve a closer state of continuity as well as generating the velocity of the jet through the stenosis and the pressure gradient across it. The amplitude adjusted approach was found to perform the best and this indicated that, because each outlet volumetric flow rate needed to be adjusted by 0.8243, then, on average, the method used to derive volumetric flow rates from doppler echocardiography over-estimated the volumetric flow rate by ~18% (relative to the first estimation).

The qualitative variations in flow and pressure fields can be seen in Figure 5-18 and Figure 5-19. These images are helpful to see that, macroscopically, the flow distributions are largely similar if considering the recirculation zones and helical nature of the flow. Although slight variations occur near the descending aorta outlet, this could be associated with the fact that the velocity of the jet through the coarctation varies which may be tending towards or away from a more turbulent flow regime.

5.5 COARCTATION OF THE AORTA *IN SILICO* INTERVENTION STUDIES

5.5.1 *In Silico* Intervention Results

5.5.1.1 ***Outlet Volumetric Flow Rate Plots***

As a result of the amplitude adjustment protocol of echo data processing showing the best performance, the same assumption was carried through for both case 2 and case 3. The incomplete and absent pieces of data for case 2 and case 3 respectively necessitated assumptions to be made to create sensible volumetric flow rate plots for each case.

In case 2, it was assumed that, because the flow through the innominate was known, that the same scaling factor used to adjust the amplitudes in case 1 would apply to account for the relationship between the average and peak velocity magnitudes at the cross section. In addition, it was also assumed that the flow split ratio in the supra-aortic branch vessels would be kept the same. To ensure that the peak value of the sum of the outlet volumetric flow rates was kept equal to the peak inlet volumetric flow rate, the inlet volumetric flow rate plot was applied to the descending aorta patch but scaled by a factor of 0.5108.

The absence of any echocardiography data for the hypothetical repair in case 3 meant that there was no outlet data that would allow for the protocols from case 1 and case 2 to be followed. Literature has shown that in healthy cases, 70-80% of the flow driven through the aorta is distributed to the descending aorta outlet [33], [52]. In conjunction, it was expected

that, as the coarctation region is expanded, the perfusion of the lower body would improve. Thus, in case 3 it was presumed that 70% of the flow entering the healthy aorta would flow through the descending aorta and the remaining 30% would be divided based on area ratios of the supra-aortic branch vessel outlet patches. Furthermore, the ascending aorta velocity-time plot was shared between case 2 and case 3. The resulting waveforms based on the above assumptions are presented in Figure 5-21 and the peak systolic volumetric flow rates at each patch which were extracted are collated in Table 5-10.

Table 5-10: Volumetric flow rate values extracted from Figure 5-21and applied as outlet boundary conditions for each case

	Volumetric Flow Rates ($10^{-5}\frac{m^3}{s}$)		
	Case 1	**Case 2**	**Case 3**
Inlet	7.84	7.92	7.92
Innominate	3.72	2.94	1.26
LCCA	1.09	0.72	0.51
LSCA	1.09	0.72	0.60
Descending Aorta	1.94	4.04	5.54

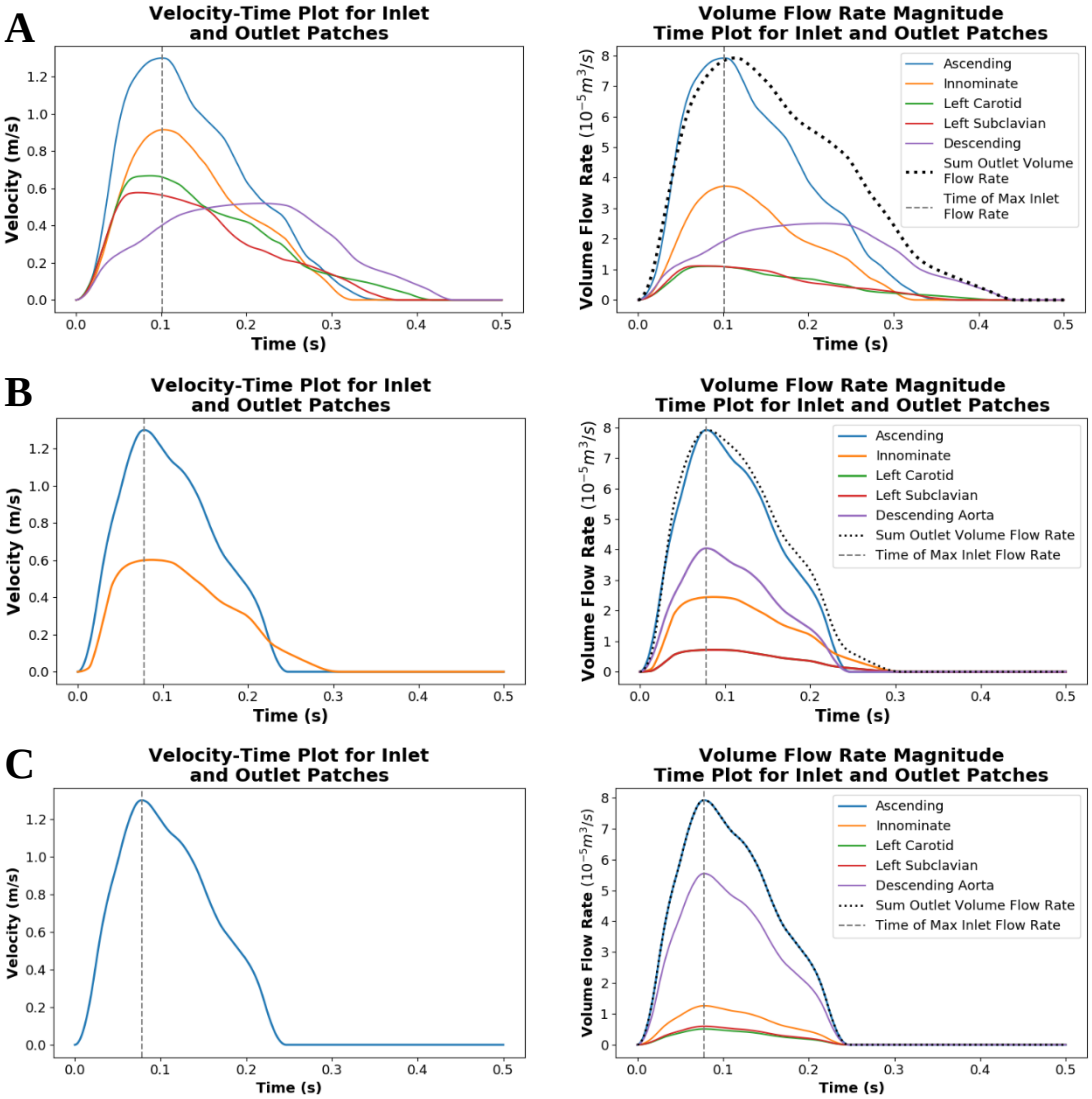

Figure 5-21: Plots showing a single cardiac cycle of available velocity data for each case and the result of data processing to create volumetric flow rate plots at each outlet for case 1 (A), case 2(B) and case 3 (C).

5.5.1.2 ***Haemodynamic Results***

The effects of interventions which improve the coarctation can be analysed through a qualitative and quantitative study of the velocity and pressure data of each case. Qualitative results of the flow and pressure fields are shown in Figure 5-22 as well as the velocity contours at each outlet in Table 5-11. It should be noted that the colour scales are purposefully made to be specific to the case to preserve flow profile detail that would be lost due to the large variation in maximums. Quantitative comparisons are shown by the outlet volumetric flow

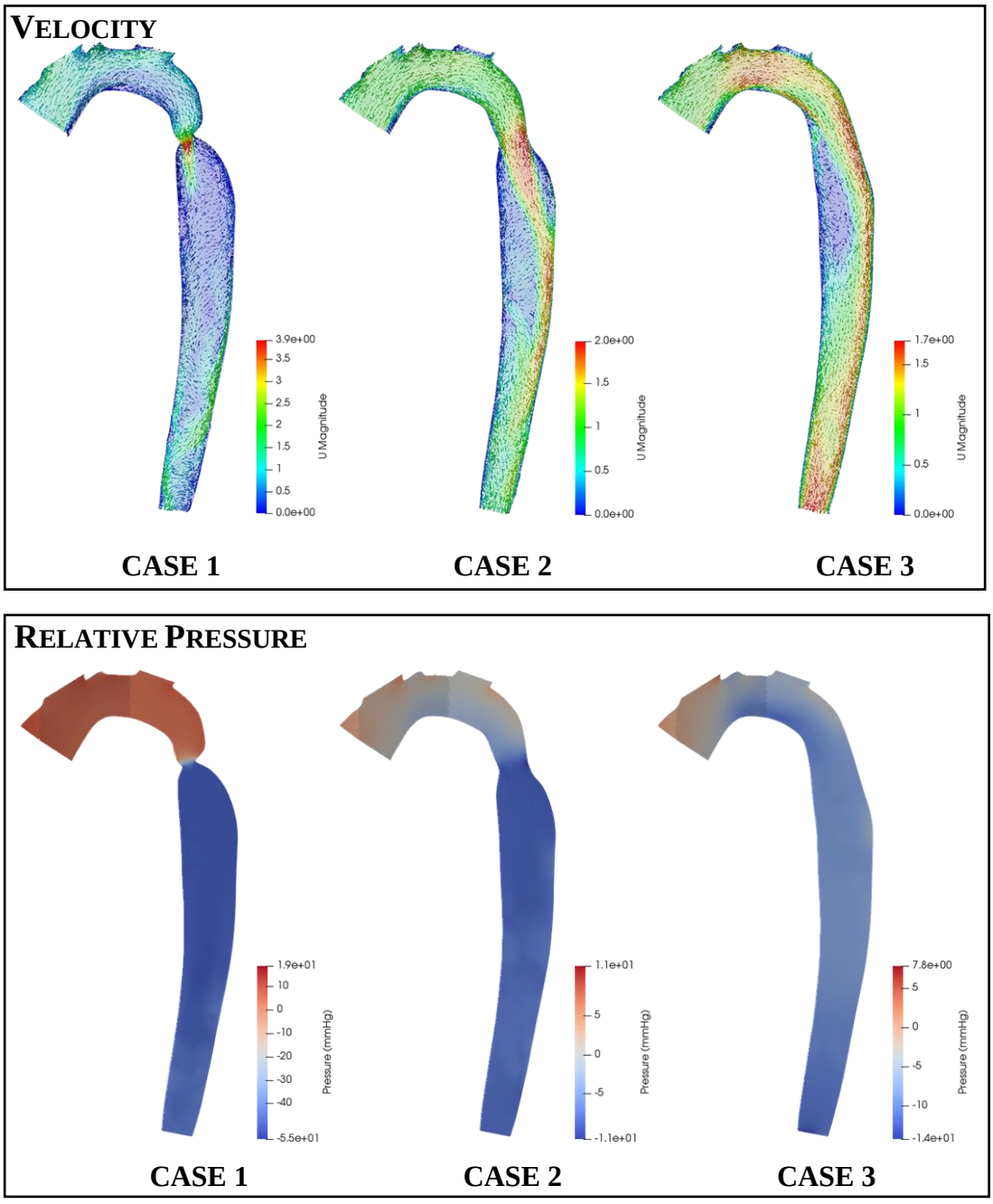

Figure 5-22: Contour and vector plots along a slice through the aortic arch and descending aorta of the velocity (top row) and pressure (bottom row) fields for each repair case. Note the unique scale bar for each case to accentuate flow distribution detail.

rate percentage compositions and maximum coarctation velocities and pressure gradient comparisons in Figure 5-23, Figure 5-24 and Figure 5-25 respectively.

Table 5-11: A qualitative comparison of the velocity magnitude contours between the different repair cases at each major outlet.

COLOUR BAR	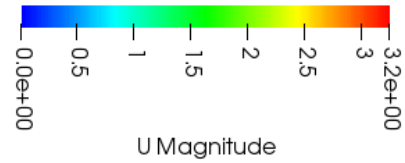		
	CASE 1	**CASE 2**	**CASE 3**
INNOMINATE	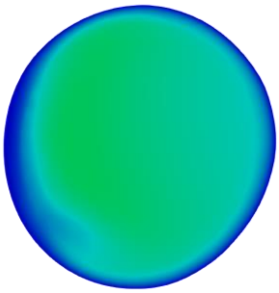	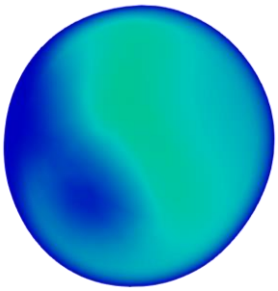	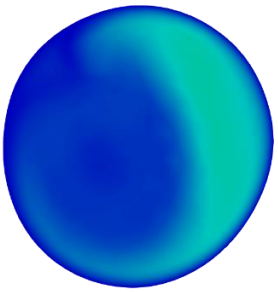
LCCA	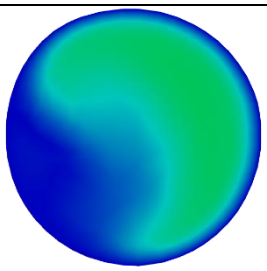	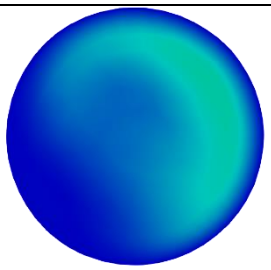	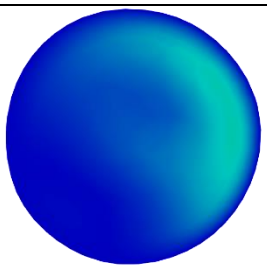
LSCA	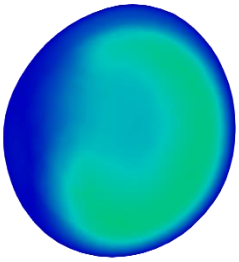	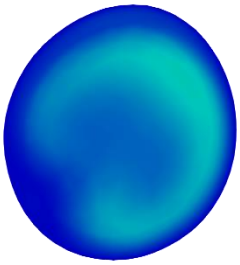	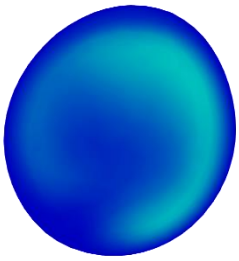
THORACIC AORTA	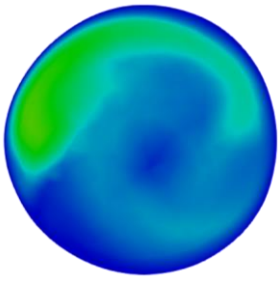	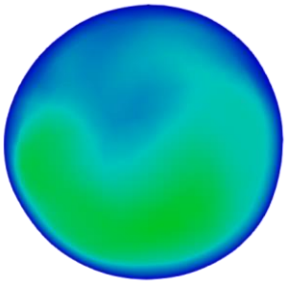	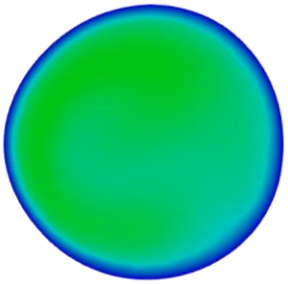

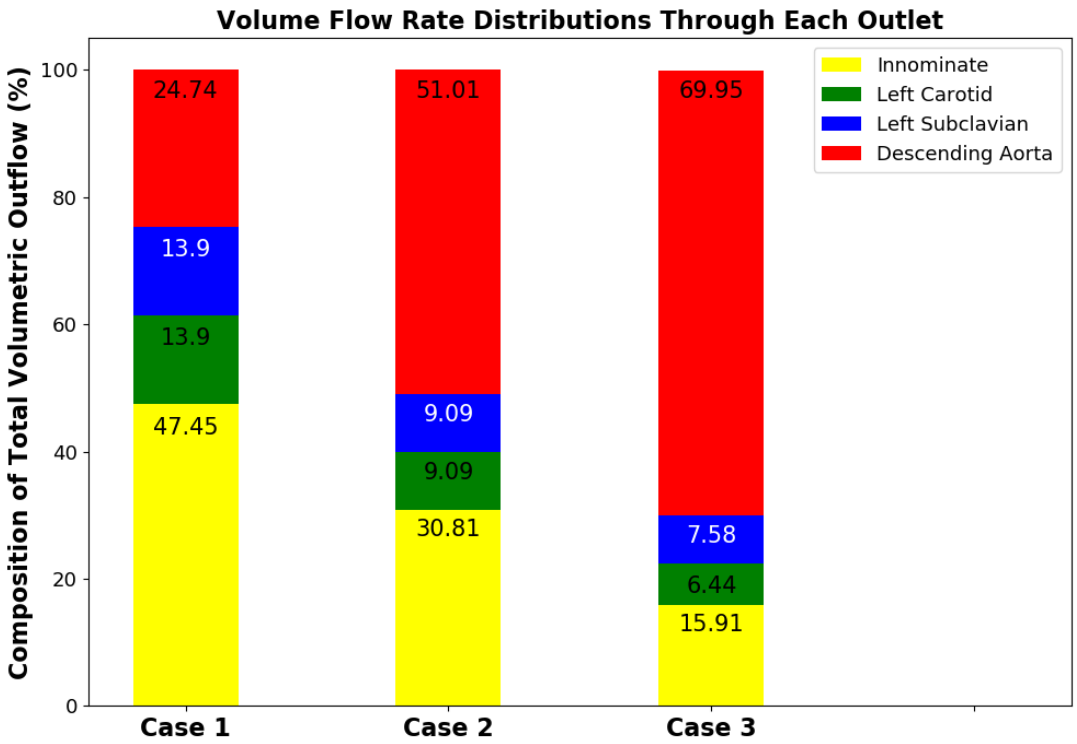

Figure 5-23: Figure showing the percentage composition of each outlet volumetric flow as a proportion to the total flow through the outlets. These values are represented as a stacked bar graph to compare the changes between each case.

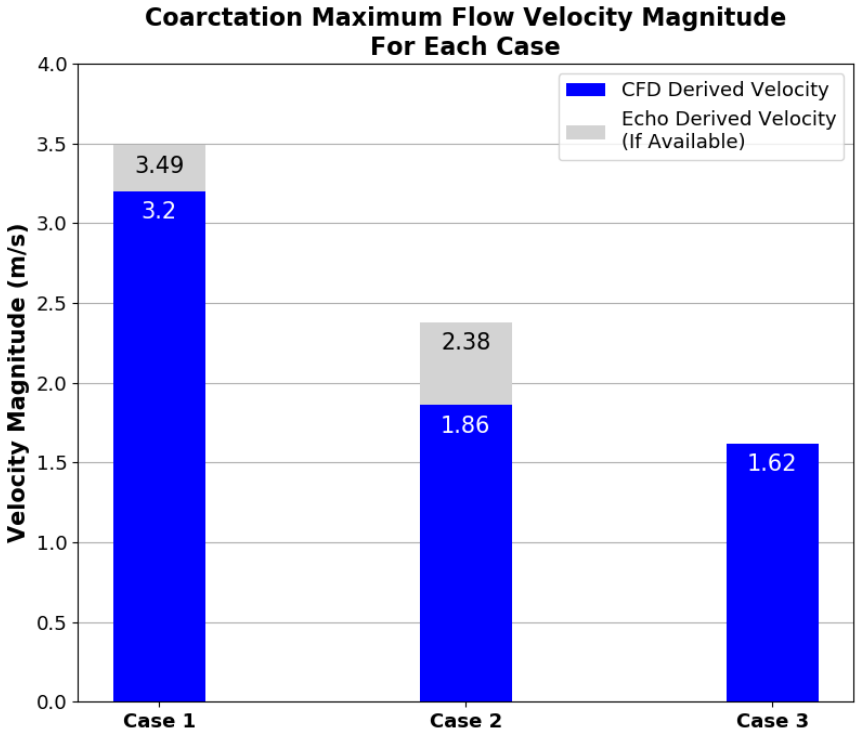

Figure 5-24: Plot showing the maximum velocity through the coarctation derived from CFD in comparison to echocardiography measurements for each case of coarctation repair. Note that echocardiography data was not available for case 3.

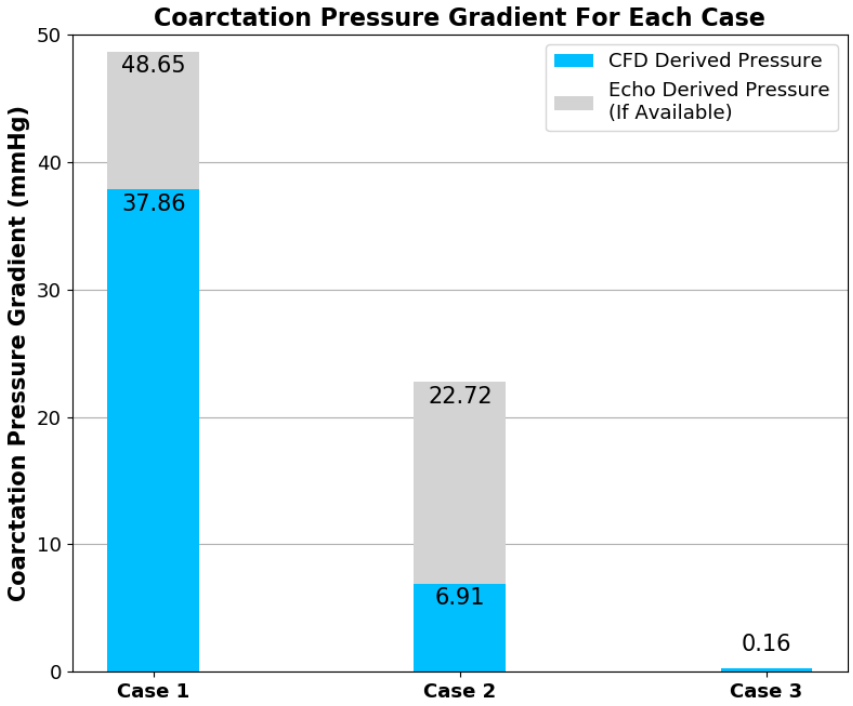

Figure 5-25: Plot showing the pressure gradient across the coarctation derived from CFD in comparison to echocardiography measurements for each case of coarctation repair. Note that echocardiography data was not available for case 3.

Velocity Results

As in previous analyses, the key velocity features which should be noted are the maximum velocity magnitude and its location, as well as flow features which are present.

Figure 5-22 shows that, in case 1 and case 2, the velocity magnitude is very clearly a maximum in the region of the coarctation constriction. This changes when the coarctation is fully expanded in case 3, where these peak velocity locations shift instead to where the fluid accelerates at the supra-aortic branch vessels. In addition, Figure 5-24 shows that the magnitude of these peak velocities in the region of the coarctation reduces from $3.24\, m.s^{-1}$ in case 1 to $1.62\, m.s^{-1}$ in case 3. Considering the echocardiography data, the maximum coarctation velocity in case 2 is found to be significantly lower than expected.

The qualitative impact of the intervention on the flow field distribution is also apparent in Figure 5-22. The high flow rate through the coarctation in case 1 is seen to create large recirculation zones, particularly in the region of post-stenotic aortic dilation. Furthermore, the flow in the rest of the descending aorta shows evidence of multiple helical flows which remain relatively chaotic and undeveloped by the time it reaches the descending aorta outlet. In contrast, the fluid flow in case 2 and case 3 shows fewer recirculation zones, more ordered helical flow and better developed flow at the outlet of the descending aorta. The recirculation

zone on the right-hand side wall, distal to the coarctation zone, reduces and disappears as the coarctation is expanded in each case.

The volumetric flow rate splits and velocity magnitude distribution at each outlet shown in Table 5-11 and Figure 5-23 provide key insights into the effect of the coarctation expansion on haemodynamics. In Table 5-11, it is evident that the contours of flow qualitatively retain a similar profile at each of the supra-aortic vessel outlets despite the mass flow splits differing. However, this trend is not seen at the descending aorta outlet where the distributions are vastly different for each instance of repair.

Granted, the volumetric flow rate split at each outlet was defined, but it is important to note that, by achieving a relative accuracy in coarctation velocities and pressure gradient compared to echo, the proportional volumetric flow splits begin to favour supply to the lower limbs through the descending aorta. Figure 5-23 indicates this by showing the higher percentage contribution to the outflow by the descending aorta outlet patch volumetric flow rate.

Due to the constriction to flow and the velocity jet created by the stenosis, it is also relevant to analyse the Reynold's number as shown in **Error! Reference source not found.** at the stenosis site to assess whether the laminar assumption is valid. From **Error! Reference source not found.** it can be seen that flow through the stenosis has a Reynold's number (Re) which indicates a laminar and lower limit transitional flow state in case 1 and case 2 respectively. Case 3 is indicated as being well within a laminar flow regime by the time flow reaches the descending aorta.

In all cases, the Womersley number is greater than 1, which indicates that flow may not be quasi-steady and as a result the pulsatile effect of flow is not necessarily negligible.

Pressure Results

The pressure gradient across the coarctation area is an important metric because this is the measurement that is so closely tied to the clinical assessment of a coarctation of the aorta patient, and the subsequent repair decision. The CFD calculated pressure gradients are shown in Figure 5-25 and correlate well with what would be expected before and after a repair as discussed from a quantitative and qualitative perspective below.

From a quantitative perspective, the pressure gradient in case 1 is shown to be in the region of the echo derived pressure gradient. As was previously discussed, this echo pressure value was not taken as a gold standard but rather as a guide for the results due to known simplifying assumptions in the modified Bernoulli equation and the consequent error in the echo measurement. Cases 2 and 3 show how the pressure gradient reduces as the coarctation is expanded, as expected. It should be noted that the CFD pressure gradient calculation in case 2

is low relative to the echo measured value. With no data to verify the results of case 3, it is assumed that the pressure gradient, which is close to zero, is realistic.

The pressure fields shown in Figure 5-22 show that there is a qualitative difference between the pressure fields in each case. As the coarctation is expanded from case 1 through to case 3, there is an evident dissipation of pressure difference upstream and downstream from the coarctation. There is, however, a residual high-pressure zone in the aortic arch despite adequate restoration to flow.

5.5.2 *In Silico* Intervention Discussion

There are key observations regarding the velocity and pressure results of each case which have been noted, but these should be assessed in light of current literature and clinical value-add. Velocity and pressure are the two fundamental fluid flow properties which are solved for by the Navier-stokes equations. These fluid metrics provide insight for clinicians in diagnosis and intervention planning of a patient. In addition, the safety of any tool is of utmost importance within the healthcare technology industry. The accuracy of the calculated values is thus of vital importance.

5.5.2.1 ***Velocity Discussion***

With the data that was available, the toolchain was able to, within 10% in case 1, recreate the peak velocity value through the coarctation zone. While an abnormally high peak velocity value will indicate that there is a constriction in the line of the vessel, it is not necessarily the diagnostic metric that clinicians use. However, in considering the data that could be collected within the bounds of what was feasible at RXH, this metric was key to ascertaining whether the simulation was generating realistic results. This was especially important from an engineering perspective, due to the relationship between the velocity of blood flow through the constriction and the pressure gradient across that coarctation, which is one of the focal points of this research. The rationale was to say that if the velocity value was accurate then the driving pressure gradient measure would also be reliable.

The methods that were used to obtain the volumetric flow rates through each outlet patch of case 1 were a result of a study which analysed four generalised schemes for processing the echocardiography velocity data. These methods were primarily developed to ensure that the flow rates were consistent with the law of mass conservation, particularly at the peak systolic flow rate. Current literature regarding the three element Windkessel boundary condition often discusses the concept of ‘tuning’ outlet boundary condition parameters to obtain the appropriate systemic flow conditions [38]. These parameters could be seen to ultimately translate to impacting the volumetric flow rate through each patch and so, in this steady state study, the concept of tuning the volumetric flow rate at each outlet boundary would be the next

logical step to improve the accuracy of the methodology. At this conceptual point of the project, however, generalised methods were implemented to demonstrate the application of CFD in a clinical setting.

The method used to calculate the outlet volumetric flow rates for case 2 was primarily based on the flow split ratios that were found in the data from case 1. Although this method did result in a redistribution of volumetric flow splits to allow more flow through the descending aorta, the maximum velocity CFD measurement at the coarctation zone fell within the region of the echocardiography measurement. Despite this, the pressure measurement was significantly different. An earlier section of the results has already demonstrated that there is a dependency between the value of the volumetric flow rate through the descending outlet, and the pressure gradient and peak velocities through the coarctation region.

The boundary conditions are crucial in the outcome of each simulation. The varying results from the testing done in section 5.4 are clear evidence of this. When relying on echocardiography as the sole modality for obtaining boundary condition data, there is likely to be a need for a higher degree of data pre-processing than what has been shown in current literature for cardiac MRI derived boundary conditions [33]. Aside from the difference in processing the clinical data to convert velocity data into volume flow rate, 2D colour doppler scans can only show the magnitude of the velocity in a single plane. Thus, assumptions need to be made regarding the profile of the velocity at its respective cross section, be it at the inlet to the ascending aorta or any outlet patch. Various studies have shown that the choice of velocity profile can have a significant impact on haemodynamics [34], [35], [59]. Oversimplifications such as plug flows can alter the haemodynamics, but in this study it was not seen to be a priority to develop a methodology to extract profiles from 2D echocardiography and validate that approach. Studies such as those by Goubergrits *et al.* [11] show that there can still be valuable insight despite making simplifications to the velocity profiles at the inlets and outlets.

The results above show the impact that assumptions relating to the use echocardiography imposes on obtaining accurate boundary conditions as discussed in section 5.4. However, the challenges of implementing echocardiography should be addressed, rather than abandoning the modality for more advanced imaging such as cardiac MRI. This is for the sole reason that it is the modality that is heavily relied on in many low and lower-middle income countries.

5.5.2.2 ***Pressure Discussion***

The unhealthy pressure distributions that are present in the aorta of patients with CoA is the chief concern that clinicians address. In general, any coarctation which generates a pressure gradient that is greater than $20\ mmHg$ will require surgery or intervention, with the goal to

reduce the gradient to close to zero [1]. The contribution that CFD can make as a tool in intervention planning and patient management can be seen through the qualitative and quantitative assessment of the pressure results for all the cases.

The relative pressure fields that are shown in Figure 5-22 for each case clearly show the improvement to the pressure distribution across the coarctation as it is expanded. This result makes sense based on the simple fact that the expansion of the coarctation reduces the resistance to flow through it which, additionally, correlates to the reduction in the speed of the velocity jet discussed previously. The relatively high pressures in the aortic arch of case 1 serve as affirmation of the risks to the patient that are associated with hypertension such as aortic rupture, cardiac failure or cerebral haemorrhage [94]. It can also be seen that, in case 2, there remains a residual pressure elevation in the aortic arch, while the pressure distribution in case 3 is seen to be relatively consistent. Qualitative comparisons of results are visually impactful but the quantification of the effect of the coarctation expansion shown in Figure 5-25 is important for the assessment of the CFD model.

The trend which is seen from case 1 to case 3 in Figure 5-25 is a result of the effect that expanding the coarctation has on the difference between the relative pressure proximal and distal to the coarctation. The coarctation pressure gradient improved after the expansion from case 1 to case 2 and was abolished in case 3. The implication of the results between case 1 and case 2 is that the pressure gradient has been reduced to a safe level without the need to expand the aorta to a degree where significant damage to the wall is caused. However, the resulting residual elevated pressure in the aortic arch in case 2 would be beneficial information for assessing the risk of the patient developing other morbidities later in life and consequently, planning the management strategy. These kind of insights are in fact the general potential that is described in much of cardiovascular CFD literature, however it is important to highlight that, in many cases and indeed in this study itself, validation of results is crucial for the safe implementation of any tool [10], [28], [52].

While the results of the pressure study were considered to show promise for what the toolchain was able to contribute to the clinical process, there is a paucity of data that would be important to verify the results and therefore make definitive assessment of the accuracy. For example, the accuracy of the pressure gradient in case 1 is found to be within 10% of the value calculated by the echocardiography however, in case 2 the difference is large. It should be noted that the echo derived value relative to the gold standard catheterisation only shows a moderate correlation and debate about its reliability as a replacement modality remains [95], [96]. However, in this instance, the paucity of patient-specific pressure data via cuff or catheter

measurements restricted any comparison of results to what was provided by the echocardiography study.

A crucial measure of success for clinical CFD tools is the judgement as to whether the result would alter a clinical decision. In case 2, feedback from clinicians was that the intervention was a success however, if the CFD result were to be the only data informing the clinicians, the significantly lower pressure gradient than that measured by the echo study could lead to an indication that risk to the patient were artificially low. The patient may, consequently, develop unexpected morbidities which may be dangerous. Thus, particularly in these early stages of development, the pressure results above should be considered with a healthy combination of scepticism and optimism based on their accuracy relative to the available data. This accuracy should be addressed in future iterations of the model.

5.6 TOOLCHAIN REVIEW

Each part of the toolchain has been discussed in detail to assess their results and bring to the reader's attention both the advantages and current challenges that are faced in the method. Above all else, the motivation for developing this process was to create a clinically applicable tool within the bounds of available methods in an emerging economy healthcare centre such as Red Cross. While paying attention to the results of each constituent of the toolchain, the toolchain as a whole should be assessed based on the required timeframe from start to finish, the infrastructure demands and the usability.

At this developmental stage the result turnaround time was not prioritised as highly as the development of the methodology. Developing the pipeline on OpenFOAM meant that the use of the CSIR Lengau HPC resources did not incur any fees, which took away the fiscal necessity to be prudent with computing resource demands as well as commercial licencing. What can be seen from the data in Table 5-12 of the total time taken for each case is that the pipeline result turn-around time, from a clinical perspective, is potentially too long. In case 1 specifically, the small cell size in the coarctation region in conjunction with the high velocity through that region, necessitated an incredibly small time-step size of $5 \times 10^{-6}\ s$ to maintain a CFL number less than 1. In comparison, the time step size for case 2 and case 3 was $1 \times 10^{-5}\ s$ which, to simulate the same amount of flow time of $1\ s$, would require half as many time steps to be calculated. The translational cardiovascular CFD community repeatedly emphasises the importance of clinically applicable results turn-around times which are in the order of minutes [43] as opposed to hours or days which has led to the implementation of reduced order CFD models and automation [43]. This pipeline should then aim to improve its turn-around time to become more applicable in a clinical environment such as RXH. This may not be in the order of minutes but could certainly improve from taking days.

Table 5-12: Table collating the approximate time taken to conduct each phase of the pipeline. Note that, in each case, only the simulation time was able to be accurately recorded as opposed to the values for segmentation, meshing and post-processing which were estimated.

Phase	Case 1	Case 2	Case 3
Echo Data Processing	00h30m	00h30m	00h30m
Segmentation	08h00m	00h30m	00h30m
Meshing	01h00m	01h00m	01h00m
Simulation	17h00m	08h30m	08h30m
Post-Processing	00h30m	00h30m	00h30m
TOTAL	**27h00m**	**11h00m**	**11h00m**

The emphasis of this study was to remain relevant and applicable across various low and lower-middle income countries. The consequence of this is that the pipeline should remain low-cost and require broadly available infrastructure. The use of CT and echocardiography for data collection and, for the most part, open-source software works towards approaching this goal. However, each simulation still depended on the ANSYS ICEM-CFD meshing software as well as 48 CPU cores on the CSIR HPC cluster. Many open source meshing packages exist and, although not implemented in this project, should be incorporated in following studies. However, the dependence on large computing resources would restrict the use of the toolchain to those healthcare facilities who have access in some way or form to large computing clusters. With the advent of cloud computing such as Google Cloud Platform [97] or Amazon Web Services [98], remote access to large computing resources has become readily accessible but computing efficiency would be of paramount importance to reduce the costs associated with the scale of the use in these systems.

A final judgement of the tool should be its usability within a non-technical clinical setting. In this regard, the rather raw and foundational work that this study presents did not find the scope to create a pipeline that was user-friendly to non-technical staff. It should be noted that there is no objective measure of this performance metric but from a clinical perspective, to truly succeed in removing the technical engineering aspects, the clinical user would require a “black box” style tool with high levels of process automation. These are non-trivial problems. For trained engineers with an existing knowledge of the packages and anatomy, this tool is thought to be well defined, however, as the technology improves so should the application for clinician usability.

6. CONCLUSION AND RECOMMENDATIONS

This chapter summarises the motivations of the project as well as the process and results of the computational pipeline that was developed. It goes further to recommend the areas that should be focussed on in the next iterations of the pipeline as well to suggest interesting lines of study based on this pipeline.

6.1 CONCLUSION

Coarctation of the aorta is one of the most prevalent forms of congenital heart disease with a global average prevalence of approximately 7% of CHD cases [1]. CHD is suspected to be poorly accounted for in low and lower-middle income countries where data is sparse, diagnoses are often delayed and consequently prognosis is negative [4]. Part of the problem with coarctation of the aorta is that, even after a repair, the patient has a high chance of recoarctation or developing secondary hypertension [6]. To address this need, CFD techniques has seen a surge in this field of research [9], [16].

The application of CFD in the clinical pipeline has the potential to provide clinicians with a tool which can complement the diagnostic mix of modalities, allow for the test and optimisation of interventions *in silico* and further understand the haemodynamic drivers for the morbidities that may develop after a repair. To prove that such a technology could fill these roles in limited resource clinical settings, a cost effective, open source CFD pipeline was developed while considering the feasibility of clinical application from a human resources, infrastructure and fiscal perspective.

In collaboration with the clinical team at Red Cross, this project was able to achieve the objective of developing a patient-specific, CFD focussed data collection protocol. The patient's diseased aorta geometry was segmented from CTA data and, in conjunction with clinicians, was able to design two hypothetical states of repair using the open source SimVascular (release 19.01.27) package. Echocardiography data was digitised using python scripting and the open source Plot Digitizer application. The university licenced ANSYS ICEM CFD (19.2) meshing package was used for volume discretisation of each geometry but was noted to be prioritised for replacement by an open source alternative. The patient data was interpreted into steady-state volumetric flow rate boundary conditions and applied to the open source OpenFOAM finite volume solver package. Following a successful grid independence study, several studies were conducted and results were visualised using the open source ParaView package. From these studies the following insights were obtained

- Within the bounds of the clinical resources that were available, it was possible to develop a patient-specific computational fluid dynamics pipeline that could successfully obtain patient data and translate it into simulated interventions as well as clinical metrics for diagnosis, planning and understanding of haemodynamics in CoA. Furthermore, the consideration for cost by using open source software packages (albeit for all except the meshing tool) was shown not to be a prohibitive decision in acquiring the necessary results.
- The standard clinical CTA imaging modality was adequate for the manual segmentation of geometries, but the noise that was present in the image prohibited the application of more automatic methods.
- The translation of echocardiography data into boundary conditions carries many variables that one needs to consider and is, in fact, a non-trivial problem. A simplified study of different approaches to this translation was conducted. A reasonable degree of accuracy in the pressure gradient and maximum velocity in the site of the coarctation was obtained by scaling the amplitude of the inlet and each outlet flow profile. Although a similar approach was taken for the post-repair coarctation data, significant error relative to the echo dataset was found in these results
- A trend in recovering pressure gradients and lower limb perfusion was found by simulating three different phases of coarctation repair. In the unrepaired simulation, a coarctation pressure gradient of $37.86\ mmHg$ and a maximum coarctation velocity of $3.24\ m.s^{-1}$ was predicted by the CFD tool. In the post-repair and healthy aorta simulations, the pressure gradient was shown to reduce to $6.91\ mmHg$ and $0.16\ mmHg$ and respectively. Likewise, the maximum velocity through the coarctation reduced. These show the positive and expected outcomes of a coarctation repair.
- In case 1, the pressure and velocity metrics would pass clinical benchmarks for indicating that a repair would be needed. Although, relative to the echocardiography measurement, these represented a 22.2% and 8.3% error respectively. Error increased in the post-repair case but, due to the reduced level of data, this could be attributed to the simplifying assumptions that were introduced.

6.2 RECOMMENDATIONS

In considering the current research which is being conducted in cardiovascular CFD, the methodology that was implemented in this pipeline and the results which were obtained, it must be recognised that this research is not final and has potential for further analysis to be

conducted as well as room for various constituents to be improved. The recommendations for further investigations and pipeline development are:

1. Each constituent of the pipeline should be investigated in detail to make it more efficient, robust and user-friendly.
    a. The substitution of the commercial ANSYS ICEM-CFD package with an open source alternative is an urgent priority to achieve a totally open source CFD pipeline. The open source mesh generation library, cfMesh, is implemented within the OpenFOAM framework and should be the first to be implemented.
    b. Methods which can process echocardiography data or implement 3D echocardiography to obtain better flow detail for boundary conditions should be investigated.
    c. Implementing automated or at least less laborious image segmentation methods would reduce the turn-around time of results and so improve the clinical applicability of the pipeline.
    d. An in-depth comparison of finite volume schemes, fluid models and protocols for the development of advanced boundary conditions such as lumped parameter models should be conducted with the aim to improve efficiency and accuracy of OpenFOAM simulations.
    e. Turbulence models should be investigated for implementation
2. Apart from the development of the pipeline, there are several interesting haemodynamic studies which can be conducted to further research coarctation of the aorta
    a. Parametric studies which study the relationship between the coarctation ratio and the key haemodynamic properties such as pressure gradient, velocity, TAWSS and OSI will be an interesting contribution to the current body of knowledge
    b. Sensitivity analyses of the boundary conditions and segmentation error should be conducted to show how important accuracy in these regards are for the simulation
3. The collaboration with the clinical team at RXH gives the unique opportunity for access to a broad dataset of patient cases. This can be leveraged to develop a CFD focussed patient-specific database of coarctation to provide researchers with a volume of cases to test methodologies on. CFD techniques are seeing maturation and accreditation for use in clinical settings and thus large databases for the validation and testing of tools will have a crucial role to play in the coming years.

4. Armstrong *et al.* has shown that 3D rotational angiography (3DRA) can provide adequate data for the development of patient-specific geometries for blood flow simulation studies [43]. This development may be an important step in making the data collection protocol simpler and broadly applicable in other resource constrained countries. It should thus be investigated as a potential imaging modality.

Future development of this work should remain focussed on patient-centred translational outcomes and strive towards a broad application. This will ensure that under-resourced healthcare facilities can also benefit from technical advances and improve their patient outcomes.

Children with a congenital heart disease such as CoA will, by no fault of their own, carry the consequences of the defect. Even after a repair, there is significant impact on longevity and morbidity. These patients deserve to have every opportunity to live full lives. Collaborations such as those between the clinical and engineering teams in this research field can leverage the unique skillsets of each to make strides towards turning this goal into a reality.

7. REFERENCES

[1] J. W. Nance, R. E. Ringel, and E. K. Fishman, “Coarctation of the aorta in adolescents and adults: A review of clinical features and CT imaging,” *J. Cardiovasc. Comput. Tomogr.*, vol. 10, no. 1, pp. 1–12, 2016.

[2] D. van der Linde *et al.*, “Birth Prevalence of Congenital Heart Disease Worldwide,” *J. Am. Coll. Cardiol.*, vol. 58, no. 21, pp. 2241–2247, Nov. 2011.

[3] E. Marijon *et al.*, “Prevalence of congenital heart disease in schoolchildren of sub-Saharan Africa, Mozambique,” *Int. J. Cardiol.*, vol. 113, no. 3, pp. 440–441, 2006.

[4] L. Zühlke, M. Mirabel, and E. Marijon, “Congenital heart disease and rheumatic heart disease in Africa: Recent advances and current priorities,” *Heart*, vol. 99, no. 21, pp. 1554–1561, 2013.

[5] A. O. Mocumbi, E. Lameira, A. Yaksh, L. Paul, M. B. Ferreira, and D. Sidi, “Challenges on the management of congenital heart disease in developing countries,” *Int. J. Cardiol.*, vol. 148, no. 3, pp. 285–288, 2011.

[6] D. Kenny, J. W. Polson, R. P. Martin, J. F. R. Paton, and A. R. Wolf, “Hypertension and coarctation of the aorta: An inevitable consequence of developmental pathophysiology,” *Hypertens. Res.*, vol. 34, no. 5, pp. 543–547, 2011.

[7] C. L. Backer, “Coarctation: The search for the Holy Grail,” *J. Thorac. Cardiovasc. Surg.*, vol. 126, no. 2, pp. 329–331, 2003.

[8] E. J. Dijkema, T. Leiner, and H. B. Grotenhuis, “Diagnosis, imaging and clinical management of aortic coarctation,” *Heart*, vol. 103, no. 15, pp. 1148–1155, 2017.

[9] P. D. Morris *et al.*, “Computational fluid dynamics modelling in cardiovascular medicine,” *Heart*, vol. 102, no. 1, pp. 18–28, 2016.

[10] A. L. Marsden and J. A. Feinstein, “Computational modeling and engineering in pediatric and congenital heart disease,” *Curr. Opin. Pediatr.*, vol. 27, no. 5, pp. 587–596, 2015.

[11] L. Goubergrits *et al.*, “Is MRI-Based CFD Able to Improve Clinical Treatment of Coarctations of Aorta?,” *Ann. Biomed. Eng.*, vol. 43, no. 1, pp. 168–176, 2014.

[12] A. Updegrove, N. M. Wilson, J. Merkow, H. Lan, A. L. Marsden, and S. C. Shadden, “SimVascular: An Open Source Pipeline for Cardiovascular Simulation,” *Ann. Biomed. Eng.*, vol. 45, no. 3, pp. 525–541, 2017.

[13] “Plot Digitizer,” 2015. [Online]. Available: http://plotdigitizer.sourceforge.net/. [Accessed: 20-Feb-2019].

[14] P. Kumar and M. Clark, *Kumar and Clark’s Clinical Medicine*. 2014.

[15] H. Suradi and Z. M. Hijazi, “Current management of coarctation of the aorta,” *Glob. Cardiol. Sci. Pract.*, vol. 2015, no. 4, p. 44, 2015.

[16] C. Capelli *et al.*, “Patient-specific simulations for planning treatment in congenital heart disease,” *Interface Focus*, vol. 8, no. 1, 2018.

[17] D. Kumar, R. Vinoth, A. Raviraj, and C. S. Vijay Shankar, “Non-Newtonian and newtonian blood flow in human aorta: A transient analysis,” *Biomed. Res.*, vol. 28, no. 7, pp. 3194–3203, 2017.

[18] J. R. Cebral *et al.*, “Clinical Application of imag,” *Int. j. numer. method. biomed. eng.*, vol. 27, no. July 2011, pp. 977–992, 2011.

[19] A. Polanczyk, M. Podgorski, T. Wozniak, L. Stefanczyk, and M. Strzelecki, “Computational fluid dynamics as an engineering tool for the reconstruction of hemodynamics after carotid artery stenosis operation: A case study,” *Med.*, vol. 54, no. 3, 2018.

[20] M. Salcher, H. Naci, T. J. Law, T. Kuehne, S. Schubert, and M. Kelm, “Balloon dilatation and stenting for aortic coarctation: A systematic review and meta-analysis,” *Circ. Cardiovasc. Interv.*, vol. 9, no. 6, pp. 1–11, 2016.

[21] M. A. Padalino *et al.*, “Surgical repair of aortic coarctation in pediatric age: A single center two decades experience,” *J. Card. Surg.*, vol. 34, no. 5, pp. 256–265, 2019.

[22] Y. Wu *et al.*, “Is balloon angioplasty superior to surgery in the treatment of paediatric native coarctation of the aorta: A systematic review and meta-analysis,” *Interact. Cardiovasc. Thorac. Surg.*, vol. 28, no. 2, pp. 291–300, 2019.

[23] E. Cecchi *et al.*, “Role of hemodynamic shear stress in cardiovascular disease,” *Atherosclerosis*, vol. 214, no. 2, pp. 249–256, 2011.

[24] J. F. J. LaDisa *et al.*, “Computational Simulations Demonstrate Altered Wall ShearStress in Aortic Coarctation Patients Treated by Resection withEnd-to-end Anastomosis,” pp. 432–443, 2011.

[25] A. J. Marelli, R. Ionescu-Ittu, A. S. Mackie, L. Guo, N. Dendukuri, and M. Kaouache, “Lifetime prevalence of congenital heart disease in the general population from 2000 to 2010,” *Circulation*, vol. 130, no. 9, pp. 749–756, 2014.

[26] G. Biglino, C. Capelli, J. Bruse, G. M. Bosi, A. M. Taylor, and S. Schievano, "Computational modelling for congenital heart disease: How far are we from clinical translation?," *Heart*, vol. 103, no. 2, pp. 98–103, 2017.

[27] D. A. de Zélicourt and V. Kurtcuoglu, "Patient-Specific Surgical Planning, Where Do We Stand? The Example of the Fontan Procedure," *Ann. Biomed. Eng.*, vol. 44, no. 1, pp. 174–186, 2016.

[28] A. Rinaudo *et al.*, "Computational fluid dynamics simulation to evaluate aortic coarctation gradient with contrast-enhanced CT," *Comput. Methods Biomech. Biomed. Engin.*, vol. 18, no. 10, pp. 1066–1071, 2015.

[29] B. Melka, W. Adamczyk, M. Rojczyk, A. J. Nowak, A. Golda, and Z. Ostrowski, "Virtual Therapy Simulation for Patient with Coarctation of the Aorta Using CFD Blood Flow Modelling," in *Advances in Intelligent Systems and Computing: Innovations in Biomedical Engineering*, 2018, vol. 623.

[30] N. Wilson, K. Wang, R. W. Dutton, and C. Taylor, "A Software Framework for Creating Patient Specific Geometric Models from Medical Imaging Data for Simulation Based Medical Planning of Vascular Surgery," in *International Conference on Medical Image Computing and Computer-Assisted Intervention*, 2001, pp. 449–456.

[31] K. Dyamenahalli and R. Shandas, "Pediatric and congenital cardiology, cardiac surgery and intensive care," in *Pediatric and Congenital Cardiology, Cardiac Surgery and Intensive Care*, E. M. da Cruz, D. Ivy, and J. Jaggers, Eds. London: Springer-Verlag, 2014, pp. 3471–3490.

[32] P. Berg *et al.*, "Multiple Aneurysms AnaTomy CHallenge 2018 (MATCH): Phase I: Segmentation," *Cardiovasc. Eng. Technol.*, vol. 9, no. 4, pp. 565–581, 2018.

[33] S. Pirola *et al.*, "On the choice of outlet boundary conditions for patient-specific analysis of aortic flow using computational fluid dynamics," *J. Biomech.*, vol. 60, pp. 15–21, 2017.

[34] U. Morbiducci *et al.*, "Outflow conditions for image-based hemodynamic models of the carotid bifurcation: Implications for indicators of abnormal flow," *J. Biomech. Eng.*, vol. 132, no. 9, p. 091005, 2010.

[35] D. Gallo *et al.*, "On the use of in vivo measured flow rates as boundary conditions for image-based hemodynamic models of the human aorta: Implications for indicators of abnormal flow," *Ann. Biomed. Eng.*, vol. 40, no. 3, pp. 729–741, 2012.

[36] S. N. Doost, D. Ghista, B. Su, L. Zhong, and Y. S. Morsi, “Heart blood flow simulation: A perspective review,” *Biomed. Eng. Online*, vol. 15, no. 1, pp. 1–28, 2016.

[37] R. Mittal *et al.*, “Computational modeling of cardiac hemodynamics: Current status and future outlook,” *J. Comput. Phys.*, vol. 305, pp. 1065–1082, 2016.

[38] R. M. Romarowski, A. Lefieux, S. Morganti, A. Veneziani, and F. Auricchio, “Patient-specific CFD modelling in the thoracic aorta with PC-MRI–based boundary conditions: A least-square three-element Windkessel approach,” *Int. j. numer. method. biomed. eng.*, vol. 34, no. 11, pp. 1–21, 2018.

[39] I. E. Vignon-Clementel, A. L. Marsden, and J. A. Feinstein, “A primer on computational simulation in congenital heart disease for the clinician,” *Prog. Pediatr. Cardiol.*, vol. 30, no. 1–2, pp. 3–13, 2010.

[40] P. Reymond, P. Crosetto, S. Deparis, A. Quarteroni, and N. Stergiopulos, “Physiological simulation of blood flow in the aorta: Comparison of hemodynamic indices as predicted by 3-D FSI, 3-D rigid wall and 1-D models,” *Med. Eng. Phys.*, vol. 35, no. 6, pp. 784–791, 2013.

[41] K. Itatani *et al.*, “New imaging tools in cardiovascular medicine: computational fluid dynamics and 4D flow MRI,” *Gen. Thorac. Cardiovasc. Surg.*, vol. 65, no. 11, pp. 611–621, 2017.

[42] S. Jin, J. Oshinski, and D. P. Giddens, “Effects of Wall Motion and Compliance on Flow Patterns in the Ascending Aorta,” *J. Biomech. Eng.*, vol. 125, no. 3, p. 347, 2003.

[43] A. K. Armstrong, J. D. Zampi, L. M. Itu, and L. N. Benson, “Use of 3D rotational angiography to perform computational fluid dynamics and virtual interventions in aortic coarctation,” *Catheter Cardiovasc Interv.*, pp. 1–6, 2019.

[44] A. L. Marsden and M. Esmaily-Moghadam, “Multiscale Modeling of Cardiovascular Flows for Clinical Decision Support,” *Appl. Mech. Rev.*, vol. 67, no. 3, p. 030804, 2015.

[45] L. Cao *et al.*, “Fully automatic segmentation of type B aortic dissection from CTA images enabled by deep learning,” *Eur. J. Radiol.*, vol. 121, no. June, p. 108713, 2019.

[46] L. Antiga, M. Piccinelli, L. Botti, B. Ene-Iordache, A. Remuzzi, and D. A. Steinman, “An image-based modeling framework for patient-specific computational hemodynamics,” *Med. Biol. Eng. Comput.*, vol. 46, no. 11, pp. 1097–1112, 2008.

[47] Kitware, “ITK - Segmentation & Registration Toolkit,” *Http://Www.Itk.Org/*. 2012.

[48] “Horos Project – Free DICOM Medical Image Viewer,” 2019. [Online]. Available:

https://horosproject.org/. [Accessed: 25-Nov-2018].

[49] V. Díaz-Zuccarini *et al.*, "Adaptation and development of software simulation methodologies for cardiovascular engineering: Present and future challenges from an end-user perspective," *Philos. Trans. R. Soc. A Math. Phys. Eng. Sci.*, vol. 367, no. 1898, pp. 2655–2666, 2009.

[50] A. C. Benim, A. Nahavandi, A. Assmann, D. Schubert, P. Feindt, and S. H. Suh, "Simulation of blood flow in human aorta with emphasis on outlet boundary conditions," *Appl. Math. Model.*, vol. 35, no. 7, pp. 3175–3188, 2011.

[51] L. Goubergrits *et al.*, "Patient-specific requirements and clinical validation of MRI-based pressure mapping: A two-center study in patients with aortic coarctation," *J. Magn. Reson. Imaging*, vol. 49, no. 1, pp. 81–89, 2019.

[52] D. Cosentino *et al.*, "Patient-specific computational models to support interventional procedures: A case study of complex aortic re-coarctation," *EuroIntervention*, vol. 11, no. 6, pp. 669–672, 2015.

[53] C. M. Lawley, K. M. Broadhouse, F. M. Callaghan, D. S. Winlaw, G. A. Figtree, and S. M. Grieve, "4D flow magnetic resonance imaging: role in pediatric congenital heart disease," *Asian Cardiovasc. Thorac. Ann.*, vol. 26, no. 1, pp. 28–37, 2018.

[54] F. Donati *et al.*, "Beyond Bernoulli: Improving the Accuracy and Precision of Noninvasive Estimation of Peak Pressure Drops," *Circ. Cardiovasc. Imaging*, vol. 10, no. 1, pp. 1–9, 2017.

[55] L. Goubergrits *et al.*, "MRI-based computational fluid dynamics for diagnosis and treatment prediction: Clinical validation study in patients with coarctation of aorta," *J. Magn. Reson. Imaging*, vol. 41, no. 4, pp. 909–916, 2015.

[56] L. Goubergrits *et al.*, "The impact of MRI-based inflow for the hemodynamic evaluation of aortic coarctation," *Ann. Biomed. Eng.*, vol. 41, no. 12, pp. 2575–2587, 2013.

[57] S. Manthey *et al.*, "Comparison of pressure reconstruction approaches based on measured and simulated velocity fields," *Curr. Dir. Biomed. Eng.*, vol. 3, no. 2, p. 309, 2017.

[58] I. E. Vignon-Clementel, C. A. Figueroa, K. E. Jansen, and C. A. Taylor, "Outflow boundary conditions for 3D simulations of non-periodic blood flow and pressure fields in deformable arteries," *Comput. Methods Biomech. Biomed. Engin.*, vol. 13, no. 5, pp.

625–640, 2010.

[59] U. Morbiducci, R. Ponzini, D. Gallo, C. Bignardi, and G. Rizzo, “Inflow boundary conditions for image-based computational hemodynamics: Impact of idealized versus measured velocity profiles in the human aorta,” *J. Biomech.*, vol. 46, no. 1, pp. 102–109, 2013.

[60] A. G. Brown *et al.*, “Accuracy vs. computational time: Translating aortic simulations to the clinic,” *J. Biomech.*, vol. 45, no. 3, pp. 516–523, 2012.

[61] R. Löhner, J. Cebral, O. Soto, P. Yim, and J. E. Burgess, “Applications of patient-specific CFD in medicine and life sciences,” *Int. J. Numer. Methods Fluids*, vol. 43, no. 6–7, pp. 637–650, 2003.

[62] G. Arbia *et al.*, “Numerical blood flow simulation in surgical corrections: What do we need for an accurate analysis?,” *J. Surg. Res.*, vol. 186, no. 1, pp. 44–55, 2014.

[63] D. A. Steinman *et al.*, “Variability of Computational Fluid Dynamics Solutions for Pressure and Flow in a Giant Aneurysm: The ASME 2012 Summer Bioengineering Conference CFD Challenge,” *J. Biomech. Eng.*, vol. 135, no. 2, p. 021016, 2013.

[64] P. Youssefi, A. Gomez, C. Arthurs, R. Sharma, M. Jahangiri, and C. Alberto Figueroa, “Impact of Patient-Specific Inflow Velocity Profile on Hemodynamics of the Thoracic Aorta,” *J. Biomech. Eng.*, vol. 140, no. 1, p. 011002, 2017.

[65] S. Madhavan and E. M. C. Kemmerling, “The effect of inlet and outlet boundary conditions in image-based CFD modeling of aortic flow,” *Biomed. Eng. Online*, vol. 17, no. 1, pp. 1–20, 2018.

[66] M. McElroy and A. Keshmiri, “Impact of Using Conventional Inlet/Outlet Boundary Conditions on Haemodynamic Metrics in a Subject-Specific Rabbit Aorta,” *Proc. Inst. Mech. Eng. Part H J. Eng. Med.*, vol. 232, no. 2, pp. 103–113, 2018.

[67] I. E. Vignon-Clementel, C. Alberto Figueroa, K. E. Jansen, and C. A. Taylor, “Outflow boundary conditions for three-dimensional finite element modeling of blood flow and pressure in arteries,” *Comput. Methods Appl. Mech. Eng.*, vol. 195, no. 29–32, pp. 3776–3796, 2006.

[68] B. C. Good, S. Deutsch, and K. B. Manning, “Hemodynamics in a Pediatric Ascending Aorta Using a Viscoelastic Pediatric Blood Model,” *Ann. Biomed. Eng.*, vol. 44, no. 4, pp. 1019–1035, 2016.

[69] L. J. Olivieri, D. A. de Zélicourt, C. M. Haggerty, K. Ratnayaka, R. R. Cross, and A.

P. Yoganathan, “Hemodynamic Modeling of Surgically Repaired Coarctation of the Aorta,” *Cardiovasc. Eng. Technol.*, vol. 2, no. 4, pp. 288–295, 2011.

[70] N. S. Anavekar and J. K. Oh, “Doppler echocardiography: A contemporary review,” *J. Cardiol.*, vol. 54, no. 3, pp. 347–358, 2009.

[71] C. A. Warnes *et al.*, “ACC/AHA 2008 Guidelines for the Management of Adults with Congenital Heart Disease: a report of the American College of Cardiology/American Heart Association Task Force on Practice Guidelines (writing committee to develop guidelines on the management of a,” *Circulation*, vol. 118, no. 23, pp. 765–768, 2008.

[72] T. G. Feeman, *The Mathematics of Medical Imaging: A Beginner’s Guide*, 1st Editio. New York: Springer, 2010.

[73] E. Lin and A. Alessio, “What are the basic concepts of temporal, contrast, and spatial resolution in cardiac CT?,” *J. Cardiovasc. Comput. Tomogr.*, vol. 3, no. 6, pp. 403–408, 2009.

[74] W. D. Bidgood, S. C. Horii, F. W. Prior, and D. E. Van Syckle, “Understanding and Using DICOM, the Data Interchange Standard for Biomedical Imaging,” *J. Am. Med. Informatics Assoc.*, vol. 4, no. 3, pp. 199–212, 1997.

[75] K. Bhargavi and S. Jyothi, “A Survey on Threshold Based Segmentation Technique in Image Processing,” *Int. J. Innov. Res. Dev.*, vol. 3, no. 12, pp. 234–39, 2014.

[76] H. K. Versteeg and W. Malalasekera, *An Introduction to Computational Fluid Dynamics: The Finite Volume Method*, Second Edi. Pearson Education Limited, 2007.

[77] M. Farrashkhalvat and J. P. Miles, *Basic Structured Grid Generation With An Introduction to Unstructured Grid Generation*. Butterworth-Heinemann, 2003.

[78] ANSYS, “Fluent 19.2 | Fluent User’s Guide,” 2019. [Online]. Available: https://ansyshelp.ansys.com/account/secured?returnurl=/Views/Secured/corp/prod_page.html?pn=Fluent&prodver=19.2&lang=en. [Accessed: 22-Aug-2019].

[79] K. Piskin, Senol; Dur, Onur; Pekkan, “Blood Flow in Realistic Neonatal Aorta using Open Source Software OpenFOAM Blood Flow in Realistic Neonatal Aorta using Open Source,” *Int. OpenFOAM Work.*, no. December 2016, pp. 1–6, 2013.

[80] The OpenFOAM Foundation, “OpenFOAM v6 User Guide,” 2018. [Online]. Available: https://cfd.direct/openfoam/user-guide/v6-fvschemes/. [Accessed: 20-Nov-2019].

[81] OpenCFD and ESI, “OpenFOAM_User Guide_Cell-limited gradient scheme,” 2016.

[Online]. Available: https://www.openfoam.com/documentation/guides/latest/doc/guide-schemes-gradient-cell-limited.html. [Accessed: 20-Nov-2019].

[82] OpenCFD and ESI, "OpenFOAM_ User Guide_ Backward time scheme," 2017. [Online]. Available: https://www.openfoam.com/documentation/guides/latest/doc/guide-schemes-time-backward.html. [Accessed: 20-Nov-2019].

[83] C. J. Greenshields, "OpenFOAM user guide version 5," *OpenFOAM Found. Ltd*, no. July, p. U-94, 2017.

[84] J. F. Douglas, J. M. Gasiorek, J. A. Swaffield, and L. B. Jack, *Fluid Mechanics*, 6th ed. Pearson Education Limited, 2011.

[85] C. Loudon and A. Tordesillas, "The use of the dimensionless Womersley number to characterize the unsteady nature of internal flow," *J. Theor. Biol.*, vol. 191, no. 1, pp. 63–78, 1998.

[86] The Children's Hospital Trust, "The Hospital." [Online]. Available: https://www.childrenshospitaltrust.org.za/the-hospital/. [Accessed: 27-Jul-2019].

[87] "Philips DICOM Viewer - download version R3." [Online]. Available: http://clinical.netforum.healthcare.philips.com/us_en/Explore/Clinical-News/MRI/Philips-DICOM-Viewer-download-version-R30-SP13.

[88] F. De Vita, M. D. de Tullio, and R. Verzicco, "Numerical simulation of the non-Newtonian blood flow through a mechanical aortic valve: Non-Newtonian blood flow in the aortic root," *Theor. Comput. Fluid Dyn.*, vol. 30, no. 1–2, pp. 129–138, 2016.

[89] C. A. Taylor, T. A. Fonte, and J. K. Min, "Computational fluid dynamics applied to cardiac computed tomography for noninvasive quantification of fractional flow reserve: Scientific basis," *J. Am. Coll. Cardiol.*, vol. 61, no. 22, pp. 2233–2241, 2013.

[90] T. J. Forbes *et al.*, "Comparison of surgical, stent, and balloon angioplasty treatment of native coarctation of the aorta: An observational study by the CCISC (Congenital cardiovascular interventional study consortium)," *J. Am. Coll. Cardiol.*, vol. 58, no. 25, pp. 2664–2674, 2011.

[91] F. Gervaso, C. Capelli, L. Petrini, S. Lattanzio, L. Di Virgilio, and F. Migliavacca, "On the effects of different strategies in modelling balloon-expandable stenting by means of finite element method," *J. Biomech.*, vol. 41, no. 6, pp. 1206–1212, 2008.

[92] K. Spranger, C. Capelli, G. M. Bosi, S. Schievano, and Y. Ventikos, “Comparison and calibration of a real-time virtual stenting algorithm using Finite Element Analysis and Genetic Algorithms,” *Comput. Methods Appl. Mech. Eng.*, vol. 293, pp. 462–480, 2015.

[93] A. Noble *et al.*, “Ultrasound image segmentation : a survey To cite this version : HAL Id : hal-00338658 Ultrasound Image Segmentation : A Survey,” *IEEE Trans. Med. Imaging, Inst. Electr. Electron. Eng.*, vol. 25, no. 8, pp. 987–1010, 2006.

[94] L. M. Prisant, K. Mawulawde, D. Kapoor, and C. Joe, “Coarctation of the aorta: a secondary cause of hypertension.,” *J. Clin. Hypertens. (Greenwich).*, vol. 6, no. 6, 2004.

[95] B. L. Wisotzkey, C. P. Hornik, A. S. Green, and P. C. A. Barker, “Comparison of invasive and non-invasive pressure gradients in aortic arch obstruction,” *Cardiol. Young*, vol. 25, no. 7, pp. 1348–1357, 2014.

[96] G. R. Marx and H. D. Allen, “Accuracy and pitfalls of Doppler evaluation of the pressure gradient in aortic coarctation,” *J. Am. Coll. Cardiol.*, vol. 7, no. 6, pp. 1379–1385, 1986.

[97] Google, “Cloud Computing Services | Google Cloud,” *Cloud.Google.Com*. p. 1, 2019.

[98] “Amazon Web Services (AWS) - Cloud Computing Services.” .

8. APPENDICES

8.1 APPENDIX 1: MATHEMATICAL PRELIMINARIES

8.1.1 Fundamental Principles:

8.1.1.1 ***Reference Frames:***

When subjected to shear, no matter how small, a fluid will respond by continuously deforming. The reference frame used for deriving governing equations for fluid deformation thus becomes an important consideration. This consideration is between an Eulerian or Lagrangian frame of reference.

8.1.1.2 ***Eulerian Frame of Reference:***

An Eulerian frame of reference is one that considers a control volume which is fixed in space and the properties of fluid flow are analysed in this space as particles flow in and out of the control volume over time. That is to say that the spatio-temporal variables are considered as independent of the fluid being analysed and that a particular fluid property can be expressed as:

Eq 8.1. $$\phi = \phi(\underline{\boldsymbol{x}}, t)$$

Where:

$$\underline{\boldsymbol{x}} = \boldsymbol{x}(x, y, z)$$

(x_1, x_2, x_3) are the chosen spatial coordinates and t is the time at which one samples the property. The spatial coordinates are often considered as the cartesian coordinates (x, y, z) (and will be so in the following derivations) but may be converted to cylindrical or spherical coordinates if the problem is more simply analysed in this way.

8.1.1.3 ***Lagrangian Frame of Reference:***

The Lagrangian frame of reference considers a control volume that is not fixed in space and as a result the particular property of fluid which is of interest is solved for over this control volume for a period of time. Thus, the property being analysed is linked to the control volume as it moves and deforms with the fluid. In this sense, the position variables of the control volume is not completely independent as was the case with the Eulerian approach as they are defined in terms of the position from which the particular control volume originated. Thus a fluid property can be defined as:

Eq 8.2. $$\phi = \phi\left(\underline{\boldsymbol{X}}, t\right)$$

Where:

$$\underline{\boldsymbol{X}} = \boldsymbol{X}(X, Y, Z)$$

(x_0, y_0, z_0) describes the initial position which identifies the control volume being considered at a specific time, t.

Both the Lagrangian and Eulerian frames of reference are important in the derivation of the governing equations for application in CFD. This is because the way in which a control volume is defined in the Lagrangian approach allows the conservation laws of mass, momentum and energy to be easily applied to a particular control volume containing an unchanging collection of fluid particles. The governing equations can then be derived and finally converted into the Eulerian frame of reference. This conversion is crucial for a CFD analysis where the numerical mesh is a fixed in space and time (i.e. in the Eulerian reference frame).

8.1.2 Governing Equations of Fluid Flow Fundamental Theorems

The governing equations of fluid flow are primarily the conservation of mass, momentum and energy. To be able to derive these equations an integral approach will be considered for an arbitrary control volume which contains a fixed set of fluid particles travelling through the bulk fluid. Key to this approach are the fundamental mathematics of Reynold's Transport Theorem. To give a point of reference in the following derivations, the Divergence Theorem of Gauss, Stokes' Theorem and Green's Theorem will be stated as well as the concept of the material derivative briefly discussed.

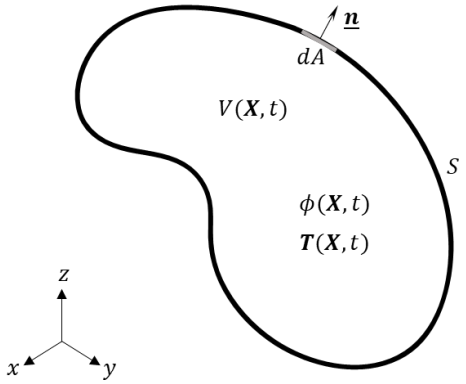

Figure 8-1: Continuum arbitrary control volume

The key theorems are presented in relation to the arbitrary control volume illustrated Figure 8-1 for which

$\boldsymbol{T}$: Represents a vector or tensor quantity

V: The control volume being integrated over

S: The surface (in 3D) or line (in 2D) which bounds the control volume

$\underline{\boldsymbol{n}}$: The normal to the differential portion of the surface

ϕ: A scalar field over the domain of the control volume

8.1.2.1 *Divergence Theorem:*

The volume integral of the divergence of some vector or tensor quantity over an arbitrary control volume is related to the surface integral over the surface of the control volume by:

Eq 8.3. $$\int_V \nabla \cdot \boldsymbol{T}\, dV = \int_S \mathbf{T} \cdot \underline{\mathbf{n}}\, dS$$

In the case where the problem is 2D the divergence theorem simplifies to Green's theorem.

8.1.2.2 *Stokes' Theorem:*

For a piecewise smooth surface with which is bounded by a closed curve that has a positive orientation (i.e. anti-clockwise). The integral of a value, $\boldsymbol{F}$, (which has partial derivatives over the surface) along the curve is equivalent to the integral of the curl over the surface:

Eq 8.4. $$\int_S (\nabla \times \boldsymbol{F}) \cdot\, dS = \oint_C \mathbf{F} \cdot dr$$

8.1.2.3 *Green's Theorem:*

For any smooth scalar function, ϕ, it's integral over the control volume of a fixed mass of particles is related to the integral over the bounding surface, S, with normal $\boldsymbol{n}$ by:

Eq 8.5. $$\int_S \phi \frac{\partial \phi}{\partial n} dS = \oint_C [\nabla\phi \cdot \nabla\phi + \phi\nabla^2\phi] dV$$

8.1.2.4 *Material Derivative:*

The material derivative is used to re-define the differential change in some value, $d\Gamma$, in the Lagrangian reference frame over some small step in time, dt to the Eulerian reference frame. Considering that, in the Lagrangian configuration, the spatial coordinates are functions of t and the initial coordinate of the control volume element and so the cartesian coordinate at the current time can be described by:

$$\boldsymbol{x} = \boldsymbol{x}(x, y, z, t)$$

Thus a small change in the quantity $d\phi$ can be shown through differential calculus to be:

Eq 8.6. $$d\phi = \frac{\partial \phi}{\partial t} dt + \frac{\partial \phi}{\partial x} dx + \frac{\partial \phi}{\partial y} dy + \frac{\partial \phi}{\partial z} dz$$

By dividing through by the change in time, dt

Eq 8.7. $$\frac{d\phi}{dt} = \frac{\partial \phi}{\partial t} + \frac{\partial \phi}{\partial x}\frac{dx}{dt} + \frac{\partial \phi}{\partial y}\frac{dy}{dt} + \frac{\partial \phi}{\partial z}\frac{dz}{dt}$$

By considering the limit as $dt \to 0$, the term on the left hand side tends towards the material derivative or the temporal derivative of Γ with respect to time in the Lagrange reference frame. In addition it can also be seen that the limits of each of the differential multipliers in the terms on the right hand side are the components of the velocity vector of the mass of fluid at that point. Thus the material derivative of the property Γ with respect to time in the Lagrange reference frame is formulated using Eulerian configuration representations by:

Eq 8.8. $$\frac{D\phi}{Dt} = \frac{\partial \phi}{\partial t} + (\boldsymbol{u} \cdot \nabla)\phi$$

8.1.2.5 ***Reynolds' Transport Theorem:***

The Reynolds' Transport Theorem is key to be able to express the material derivative of the integral of a fluid property ϕ over a control volume in the Eulerian configuration. To do this consider the arbitrary volume in Figure 8-2

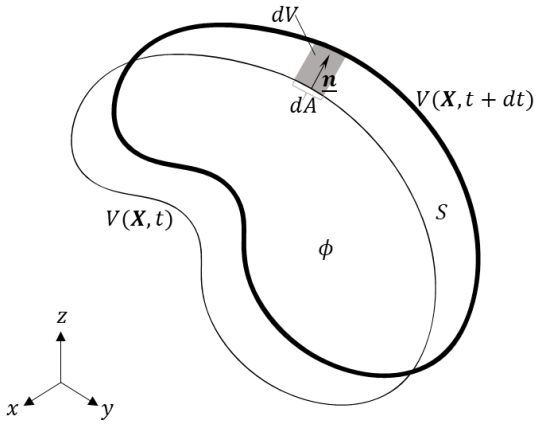

Figure 8-2: Abitrary continuous control volume at time t and t + dt

At a given time, t, the total ϕ, that is contained in the control volume is

$$\int_{V(t)} \phi dV$$

Where $\phi(\boldsymbol{x}, t) = \phi(x, y, z, t)$

Using a differential approach to analysing the material derivative of this quantity means that the material derivative can be expressed as:

$$\frac{D}{Dt}\int_{V(t)} \phi dV = \lim_{\delta t \to 0}\left[\frac{1}{\delta t}\left\{\int_{V(t+\delta t)} \phi(\boldsymbol{x},\ t + \delta t)dV - \int_{V(t)} \phi(\boldsymbol{x}, t)dV\right\}\right]$$

As an algebraic manipulation we add and subtract the same term from the right-hand side (RHS)

Eq 8.9. $$\frac{D}{Dt}\int_{V(t)}\phi dV = \lim_{\delta t\to 0}\left[\frac{1}{\delta t}\left\{\int_{V(t+\delta t)}\phi(\boldsymbol{x},\ t+\delta t)dV - \int_{V(t)}\phi(\boldsymbol{x},\ t+\delta t)dV + \int_{V(t)}\phi(\boldsymbol{x},\ t+\delta t)dV - \int_{V(t)}\phi(\boldsymbol{x},t)dV\right\}\right]$$

This can be reorganised to conveniently collect terms and by applying the rules of integration is simplified to:

Eq 8.10. $$\frac{D}{Dt}\int_{V(t)}\phi dV = \lim_{\delta t\to 0}\left[\frac{1}{\delta t}\int_{V(t+\delta t)-V(t)}\phi(\boldsymbol{x},\ t+dt)dV\right] + \lim_{\delta t\to 0}\left[\frac{1}{\delta t}\int_{V(t)}\phi(\boldsymbol{x},\ t+\delta t)-\phi(\boldsymbol{x},t)dV\right]$$

By the fundamental expression of a derivative, the second term on the RHS can be expressed as:

Eq 8.11. $$\lim_{\delta t\to 0}\left[\frac{1}{\delta t}\int_{V(t)}\phi(\boldsymbol{x},\ t+\delta t)-\phi(\boldsymbol{x},t)dV\right] = \int_{V(t)}\frac{\partial\phi(\boldsymbol{x},t)}{\partial t}dV$$

With reference Figure 8-2 the elementary change in volume, dV, can be expressed in terms of the velocity of the control volume and the surface area by:

Eq 8.12. $$dV = \boldsymbol{u}\cdot\boldsymbol{n}\delta t dA$$

This is able to be substituted as the $\boldsymbol{u}\cdot\boldsymbol{n}\delta t$ term is effectively the displacement of the control volume after a time δt perpendicular to the surface at time t. By substituting this into the first terms of Eq 8.10 the term becomes:

Eq 8.13. $$\lim_{\delta t\to 0}\left[\frac{1}{\delta t}\int_{V(t+\delta t)-V(t)}\phi(\boldsymbol{x},\ t+\delta t)dV\right] = \lim_{\delta t\to 0}\left[\frac{1}{\cancel{\delta t}1}\int_{V(t+\delta t)-V(t)}\phi\boldsymbol{u}\cdot\boldsymbol{n}\cancel{\delta t}dA\right]$$

The assumption is made that the change of the volume is so small that, in fact, the value of ϕ remains constant over the volume and that the difference in the volume is approximately equivalent to the surface area bounding the volume. Thus:

Eq 8.14. $$\lim_{\delta t\to 0}\left[\int_{V(t+\delta t)-V(t)}\phi\boldsymbol{u}\cdot\boldsymbol{n}dA\right] = \oint_{A(t)}\phi\boldsymbol{u}\cdot\boldsymbol{n}dA$$

By substituting the rearrangements of term 1 and term 2, the Eq 8.10 becomes:

Eq 8.15. $$\frac{D}{Dt}\int_{V(t)}\phi dV = \int_{V(t)}\frac{\partial\phi(\boldsymbol{x},t)}{\partial t}dV + \oint_{A(t)}\phi\boldsymbol{u}\cdot\boldsymbol{n}dA$$

The divergence theorem can then be used to convert the surface integral of the second term to a volume integral resulting in:

Eq 8.16. $$\frac{D}{Dt}\int_{V(t)}\phi dV = \int_{V(t)}\frac{\partial\phi(\boldsymbol{x},t)}{\partial t} + \nabla\cdot(\phi\boldsymbol{u})dV$$

This result is the weak form of the expression of the Lagrangian configuration in terms of the Eulerian derivatives. To extract the strong for it can be shown that:

Eq 8.17. $$\frac{D}{Dt}\int_{V(t)}\phi dV = \int_{V(t)}\frac{D}{Dt}\phi dV$$

Because the following derivation has assumed that the control volume which is being analysed in completely arbitrary, then it must be necessary that it holds for any control volume chosen. For this to hold for any control volume then, it is necessary that the integrands on the left and right-hand side of the equations are equivalent. Thus:

Eq 8.18. $$\frac{D\phi}{Dt} = \frac{\partial\phi(\boldsymbol{x},t)}{\partial t} + \boldsymbol{\nabla}\cdot(\phi\boldsymbol{u})$$

This result expresses the material derivative of a scalar property ϕ in terms of the Eulerian reference configuration. This formulation has a slight nuance which differentiates it from the material derivative discussed previously in that the material derivative assumes constant something or other

RTT is crucial in the development of the conservation laws which constitute the governing equations of fluid flow. The result the weak or integral form of RTT will hence be used.

8.1.3 Governing Equations of Fluid Flow Derivation

The governing equations of fluid flow are derived from the fundamental principles of conservation of mass, momentum and energy. These derived equations are collectively known as the Navier-Stokes Equations and have remained unchanged since 1845.

8.1.3.1 ***Conservation of Mass***

If one considers the control volume shown in Figure 8-1 which is followed in the Lagrangian reference frame, it is necessary that, although the shape of the volume may deform and move, the mass contained within the volume remains constant. Consider that the mass contained with in the volume is described by:

Eq 8.19. $$m = \int_V \rho dV$$

Considering that it is known that this quantity does not change over time, it follows that the material derivative of the mass is zero. Thus:

Eq 8.20. $$\frac{D}{Dt}\int_V \rho dV = 0$$

By applying RTT in it's weak form, and by making $\phi = \rho$, this simply becomes:

Eq 8.21. $$\frac{D}{Dt}\int_V \rho dV = \int_{V(t)}\frac{\partial\rho}{\partial t} + \nabla\cdot(\rho\boldsymbol{u})dV = 0$$

Due to the assumption of the control volume being completely arbitrary it must be the case that the integrand must be zero to satisfy the equation above. Thus the conservation of mass for both incompressible and compressible fluids can be re written as:

Eq 8.22. $$\frac{\partial \rho}{\partial t} + \nabla \cdot (\rho \boldsymbol{u}) = 0$$

By applying the product rule the second term can be re written as:

Eq 8.23. $$\nabla \cdot (\rho \boldsymbol{u}) = \rho \boldsymbol{\nabla} \cdot \boldsymbol{u} + (\boldsymbol{\nabla} \rho) \cdot \boldsymbol{u}$$

For incompressible cases however, the density of the fluid is assumed to be constant and thus:

Eq 8.24. $$\boldsymbol{\nabla} \rho = 0$$

The conservation of mass then simplifies to:

Eq 8.25. $$\frac{\partial \rho}{\partial t} + \rho \boldsymbol{\nabla} \cdot \boldsymbol{u} = 0$$

The same assumption of incompressibility also necessitates that density is constant over time too. By applying this constraint and dividing through by the density it can be shown that, for an incompressible fluid, the conservation of mass requires that the divergence of the velocity vector field is zero. This is known as the continuity equation which states:

Eq 8.26. $$\boldsymbol{\nabla} \cdot \boldsymbol{u} = 0$$

8.1.3.2 ***Conservation of Momentum***

Consider the Figure 8-1 which illustrates an arbitrary control volume which has a surface traction as well as a body force acting on it. The conservation of momentum is based on Newton's second law of motion which states that the rate of change of momentum is equal to the total force acting on that mass of fluid.

To adequately describe the conservation of momentum, a brief overview of the forces which may act on the fluid will be given to derive the most general form of Newton's second law which can then be used to derive the Navier-stokes equations for an incompressible Newtonian fluid.

Consider that the momentum of an element of fluid is the product of the mass of the control volume (which remains constant) and its velocity and thus the rate of change of momentum ($\frac{Dp}{Dt}$) can be described by:

Eq 8.27. $$\frac{Dp}{Dt} = \int_V \frac{D}{Dt}(\rho \boldsymbol{u}) dV$$

And that the total force acting on the control volume is the combination of the body (i.e. gravity) and surface forces (i.e. pressure, stress and shear) which are

Eq 8.28. $$\boldsymbol{F} = \int_V \rho \boldsymbol{g} dV + \int_S \boldsymbol{\tau} \cdot \boldsymbol{n} dS$$

Using the divergence theorem

Eq 8.29. $$\boldsymbol{F} = \int_V \rho \boldsymbol{g} + \boldsymbol{\nabla} \cdot \boldsymbol{\tau} dV$$

Where

$\boldsymbol{g}$: The vector for the gravitational force per unit mass

$\boldsymbol{\tau}$: is the total stress tensor (2nd order) which describes the force per unit area which acts on the surface of the element of fluid contained in the control volume

Thus the rate of change of momentum through Newton's second law can be described in the weak form as:

Eq 8.30. $$\int_V \frac{D}{Dt}(\rho \boldsymbol{u}) dV = \int_V \rho \boldsymbol{g} + \boldsymbol{\nabla} \cdot \boldsymbol{\tau} dV$$

Due to the arbitrariness of the control volume being analysed this can only be satisfied if the integrands are equal thus the strong form is recovered:

Eq 8.31. $$\frac{D}{Dt}(\rho \boldsymbol{u}) - \rho \boldsymbol{g} - \boldsymbol{\nabla} \cdot \boldsymbol{\tau} = 0$$

This result is known as the Cauchy equation for momentum and can be generally applied to any fluid so long as the constitutive relation between the stress and rate of deformation is known.

The total stress tensor is a combination of the stresses caused by the pressure which is exerted on the element of fluid as well as the normal and tangential viscous stresses. Thus, the total stress tensor can be described by:

Eq 8.32. $$\boldsymbol{\tau} = -p\boldsymbol{I} + \boldsymbol{T}$$

Where $\boldsymbol{T}$ is a second order tensor which describes the viscous stresses acting on the element of fluid and $\boldsymbol{I}$ is the identity tensor.

This can be substituted into Eq 8.31 and simplified:

Eq 8.33. $$\frac{D}{Dt}(\rho \boldsymbol{u}) - \rho \boldsymbol{g} - \boldsymbol{\nabla} \cdot (-p\boldsymbol{I} + \boldsymbol{T}) = 0$$

Eq 8.34. $$\frac{D}{Dt}(\rho \boldsymbol{u}) - \rho \boldsymbol{g} + \boldsymbol{\nabla} p - \boldsymbol{\nabla} \cdot \boldsymbol{T} = 0$$

At this point it is important to note that, for a Newtonian fluid the constitutive equation for $\boldsymbol{T}$ is:

Eq 8.35. $$\boldsymbol{T} = 2\mu\boldsymbol{D} + \lambda(\boldsymbol{\nabla}\cdot\boldsymbol{u})\boldsymbol{I}$$

Where:

μ: is the coefficient of dynamic viscosity

$\boldsymbol{D}$: is the deformation tensor where, for a Newtonian fluid, $\boldsymbol{D} = \frac{1}{2}(\boldsymbol{\nabla u} + (\boldsymbol{\nabla u})^T)$

λ: is the coefficient of bulk viscosity

While this is the case, for an incompressible Newtonian fluid, the continuity equation negates the second term in the stress tensor leaving

Eq 8.36. $$\boldsymbol{T} = 2\mu\boldsymbol{D}$$

Thus, the Navier-Stokes equation for an incompressible Newtonian fluid is:

Eq 8.37. $$\frac{D}{Dt}(\rho\boldsymbol{u}) = -\boldsymbol{\nabla}p + \boldsymbol{\nabla}\cdot(2\mu\boldsymbol{D}) + \rho\boldsymbol{g}$$

The coefficient of dynamic viscosity can, in some cases vary based on the concentration, temperature and pressure and so, if, in addition, the coefficient of dynamic viscosity is constant, then the Navier-Stokes Equations further simplify to:

Eq 8.38. $$\frac{D}{Dt}(\rho\boldsymbol{u}) = -\boldsymbol{\nabla}p + \mu\boldsymbol{\nabla}^2\boldsymbol{u} + \rho\boldsymbol{g}$$

This result is known as the Cauchy equation for momentum and can be generally applied to any fluid so long as the constitutive relation between the stress and rate of deformation is known. By substituting the constitutive equation for a Newtonian fluid and by applying RTT the conservation of momentum in the Eulerian reference frames are found and expressed as

Eq 8.39. $$\frac{\partial}{\partial t}(\rho\boldsymbol{u}) = -\boldsymbol{\nabla}p - \boldsymbol{\nabla}\cdot\big((\rho\boldsymbol{u})\otimes\boldsymbol{u}\big) + \mu\boldsymbol{\nabla}^2\boldsymbol{u} + \rho\boldsymbol{g}$$

8.2 APPENDIX 2: SIMPLE AND PISO ALGORITHMS

Consider the face and node numbering convention in the uncomplicated, staggered orthogonal 2D mesh in Figure 3-7. In accordance to this numbering scheme, the discretised x-component of momentum equations (which is similar to the y-component) for the (i,J) face can be expressed as:

Eq 8.40. $$a_{i,J}u_{i,J} = \sum a_{nb}u_{nb} + \left(P_{I-1,J} - P_{I,J}\right)A_{i,J} + b_{i,J}$$

Eq 8.41. $$a_{I,j}u_{I,j} = \sum a_{nb}u_{nb} + \left(P_{I,J-1} - P_{I,J}\right)A_{I,j} + b_{I,j}$$

Where:

- Coefficients $a_{i,J}$ and a_{nb} are calculated based on the chosen upwinding scheme
- P is the pressure at a point defined by the subscript
- b is the total momentum source term at the face defined by the subscript
- u is the x-component of the velocity relevant to each term to simplify subscripts

It should be noted that full mathematical rigour will be spared for the sake of balancing brevity with detail and subsequently some results will be stated. The reader is referred to [76] for comprehensive detail.

The SIMPLE algorithm begins by substituting an initial guess of a pressure field, P^*, and an initial guess of a velocity field, u^* into the discretised momentum equations in Eq 8.40 and Eq 8.41 to yield

Eq 8.42. $$a_{i,J}u^*_{i,J} = \sum a_{nb}u^*_{nb} + \left(P^*_{I-1,J} - P^*_{I,J}\right)A_{i,J} + b_{i,J}$$

And similarly, for the y-component.

The correct pressure, P, and the guessed pressure, P^*, are related by a pressure correction term, P' and similarly for the x and y velocity components (u and v) such that:

Eq 8.43. $$P = P^* + P'$$

Eq 8.44. $$u = u^* + u'$$

Eq 8.45. $$v = v^* + v'$$

Eq 8.40 is subtracted from Eq 8.42 and by considering Eq 8.43 - Eq 8.45 the discretised momentum equation can be expressed in terms of the correction factor of each field property instead

Eq 8.46. $$a_{i,J}u'_{i,J} = \sum a_{nb}u'_{nb} + \left(P'_{I-1,J} - P'_{I,J}\right)A_{i,J}$$

The primary assumption of the SIMPLE algorithm is that the summation term is assumed to be zero. Thus by applying this assumption and by dividing through by $a_{i,J}$:

Eq 8.47. $$u'_{i,J} = \frac{A_{i,J}}{a_{i,J}}\left(P'_{I-1,J} - P'_{I,J}\right)$$

And similarly, for the y-component.

While keeping this result in mind, one then turns to the discretised form of the continuity equation

Eq 8.48. $$\left[(\rho uA)_{i+1,J} - (\rho uA)_{i,J}\right] + \left[(\rho vA)_{I,j+1} - (\rho vA)_{I,j}\right] = 0$$

The continuity equation can be expressed in terms of the predicted pressures by substituting the values for the corrected velocities from Eq 8.47 into Eq 8.48, accounting for the continuity imbalance due to an inaccurate guess and through rearrangement. This results in

Eq 8.49. $$a_{I,J}P'_{I,J} = a_{I+1,J}P'_{I+1,J} + a_{I-1,J}P'_{I-1,J} + a_{I,J+1}P'_{I,J+1} + a_{I,J-1}P'_{I,J-1} + b'_{I,J}$$

Where $b'_{I,J}$ accounts for the continuity imbalance to force the zero condition.

Eq 8.49 can then be used to solve for P' to find the corrected pressure field. At this point it is common to introduce the pressure under-relaxation factor, α_p which restricts the advancement of the pressure field to assist in stability of the algorithm. Thus, the corrected pressure field is instead:

Eq 8.50. $$P = P^* + \alpha_P P'$$

Using this corrected pressure field, the corrected velocities can be found through Eq 8.40 and Eq 8.41. In the same way as the pressure field, the velocities can also have a correction factor introduced which updates the velocity through:

Eq 8.51. $$u = \alpha_v u^* + (1 - \alpha_v)u'$$

Eq 8.52. $$v = \alpha_v v^* + (1 - \alpha_v)v'$$

This loop may be iterated more than once in a time-step to improve the accuracy of the pressure and velocity fields. In a steady-state case, convergence criteria can be defined such that the iteration stops once the solution does not change significantly. In a transient case, a numerical time-step method would be applied to find the first guess of the pressure field at the next time step and the SIMPLE algorithm started again.

An algorithm schematic is presented in Figure 8-3 [76]. The PISO algorithm is based on the SIMPLE algorithm and differs by introducing more than one corrector step before testing

convergence. This adaptation, based on the same notation, is shown in a schematic of the algorithm in Figure 8-4 [76].

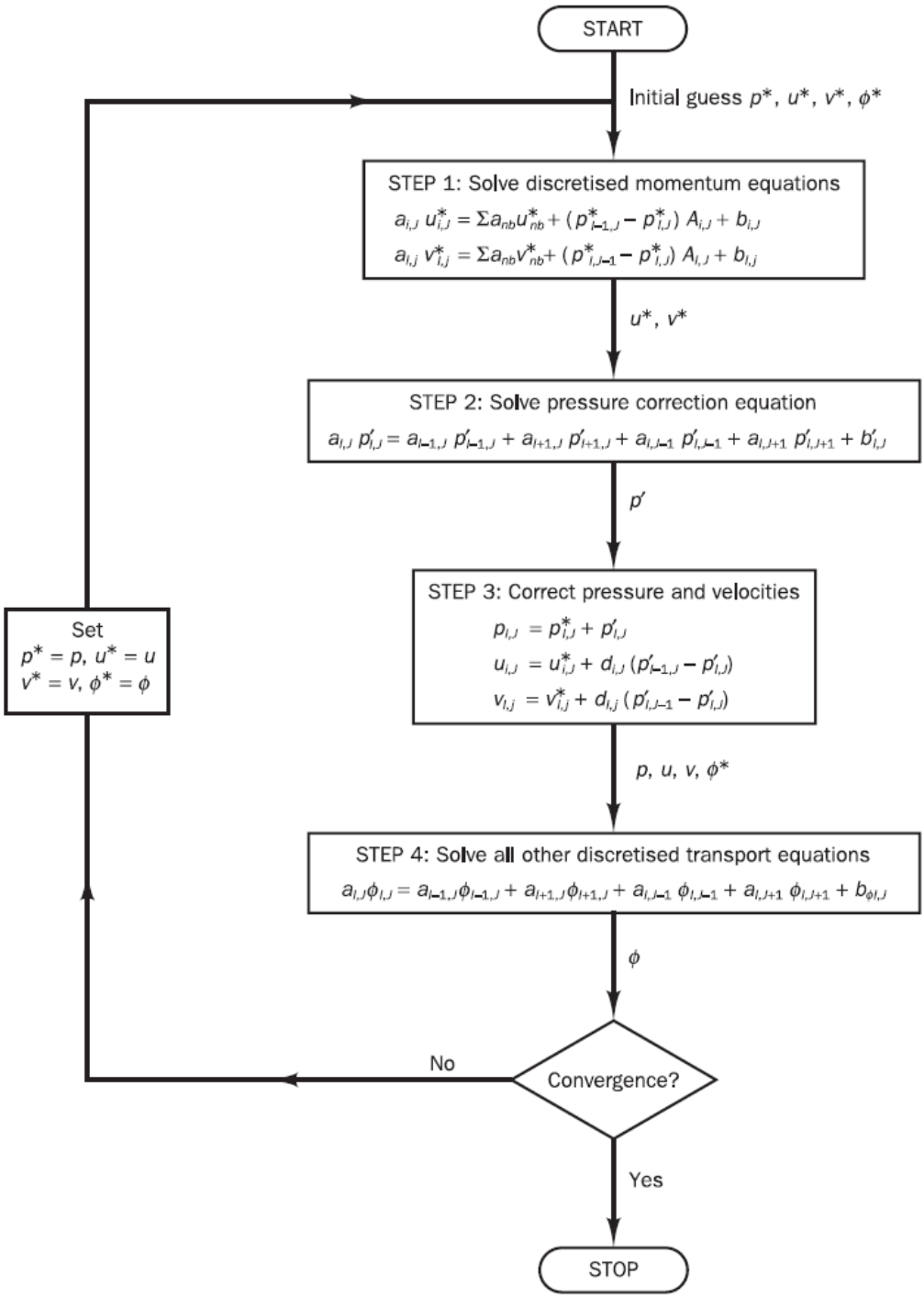

Figure 8-3: SIMPLE Algorithm flow chart by Versteeg et al. [75]

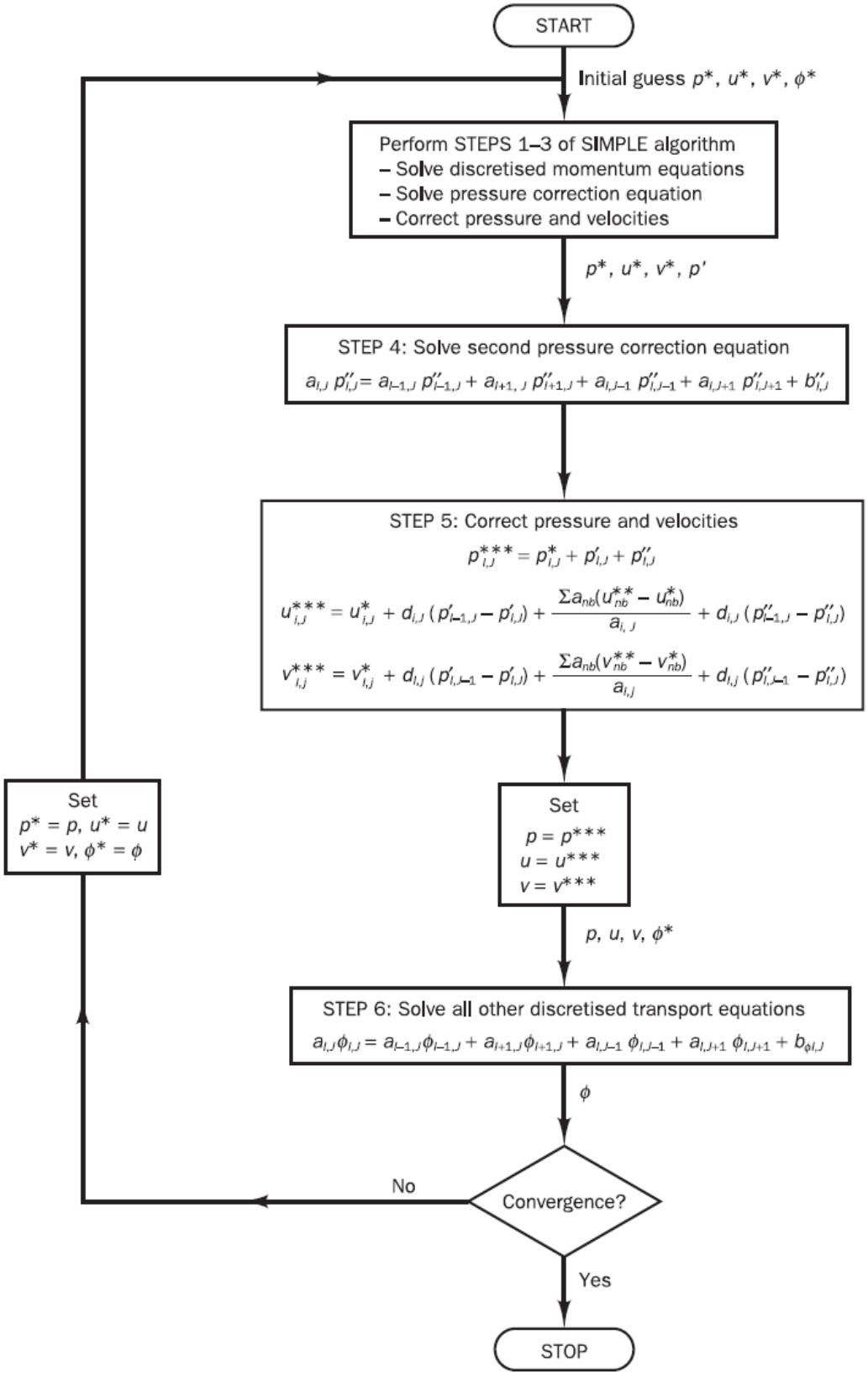

Figure 8-4: PISO Algorithm flow chart by Versteeg et al. [75]

8.3 APPENDIX 3: EXAMPLE OF CLINICAL PROTOCOL INFORMATION SHEET

COARCTATION OF THE AORTA IMAGING PROTOCOL

Overview

The purpose of this document is to give a clear and concise description of the primary areas of interest for clinical measurements of blood flow velocity to aid the development of a computational fluid dynamics (CFD) platform to model blood flow through the aorta in a child with coarctation of the aorta.

Please note:

- In each case below, echocardiograph velocity measurements that are relevant for both a pre and post repair case are given. To acquire as many of these measurements as possible will be ideal.
- Although not completely standard clinical procedure, CT is a fundamental pre-requisite and inclusion criteria for this study.
- Please also note a reference for the location if, for any reason, it deviates from the description below.

Patient Qualification:

Patients who qualify for this study are those who:

1. Are patients with coarctation of the aorta
2. Have pre-repair/diagnostic CTAs (NB)
3. Have normal branch artery configurations
4. May or may not have a bicuspid aortic valve

Data Collection Protocol:

- When a patient is identified based on the above criteria, the echocardiograph measurements as stated in
- Table 1 should, ideally be taken on the same day or as soon as possible after the first CTA investigation. This is to ensure that there are no significant differences between the structures at the time of the CTA and the time of the echo due to growth of the patient or remodelling due to the coarctation.
- ECG should be connected at the start of the echo investigation so that **diameter measurements** can be taken at **peak systole**
- Following the CoA repair echocardiograph measurements as stated in Table 2 should be taken as soon as possible to maintain a similar timeframe as the first investigation. The point here is to minimise variability in data due to growth of the patient.
- A post-operative CTA scan is not a compulsory requirement however if one is conducted it should be included in the data pack. Should a CTA not be conducted then it is still important that the echocardiograph measurements in Table 2 are taken soon after the repair.

Note:

* Echocardiography measurements may be pulse or continuous wave doppler as is applicable to the measurement being taken. Preference should be given to continuous wave doppler where possible and all meaurements should be taken with angle correction on.

* The colour map of the cross-section is to be shown while the beam is as parallel to the flow as possible.

* If there are limitations such as bifurcations or it becomes a risk to do so please go as far away from the branch at the arch as is possible.

The priority for the measurements here is to be able to collect data at the points that constitute the inlet and outlets of the region of interest that we are going to model blood flow through. That is to say that the inlet to the model will be at the ascending aorta and each vessel (left subclavian, brachiocephalic, left common carotid and descending aorta) are the outlets to the system. It is important to know the velocity at each of these points to accurately model the body of flow. In addition, the internal points are necessary to be able to ensure the calibration of the model is accurate.

Coarcted Aorta prior to repair:

Table 1: List of pressure and velocity measurements to be taken prior to the repair of the coarctation

With reference to Figure 1. (All measurements recorded for 4 cardiac cycles unless specified otherwise)

Echocardiography and colour map measurements:	
A. Ascending Aorta - Maximum and mean velocity, colour map and diameter measurement taken downstream of the aortic valve and out of the vicinity of the valves.	
B. Descending Aorta - Maximum and mean velocity, colour map and diameter at the cross-section of the descending aorta. Measurement taken prior to the diaphragm	
C. Brachiocephalic artery - Maximum and mean velocity, colour map and diameter just prior to bifurcation.	
D. Left common carotid artery (LCCA) - Maximum and mean velocity, colour map and diameter at cross-section at the point that is approximately equal to 25 mm away from the branch at the aortic arch.	
E. Left subclavian artery (LSCA) – Maximum and mean velocity, colour map and diameter at cross-section of the point that is approximately equal to 25 mm away from the branch at the aortic arch.	
F. Pressure gradient across the coarctation	

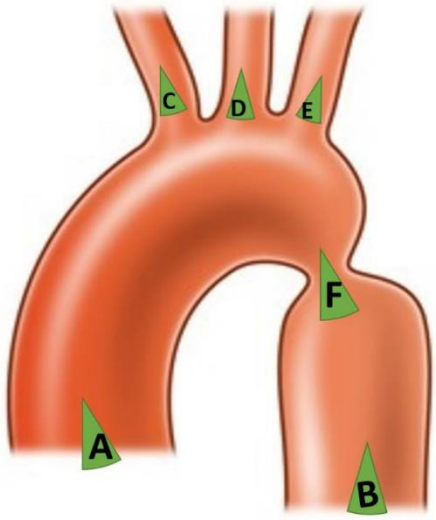

Figure 1: Pre-repair coarctation

Post-repair aorta:

Table 2: List of pressure and velocity measurements to be taken following the repair of the coarctation

With reference to Figure 2 (All measurements recorded 4 cardiac cycles unless specified otherwise)	
Priority echocardiography, colour map and diameter measurements:	
A. Ascending Aorta - Maximum and mean velocity and colour map measurement taken downstream of the aortic valve and out of the vicinity of the valves.	
B. Descending Aorta - Maximum and mean velocity and colour map at the cross-section of the descending aorta. Measurement taken prior to the diaphragm	
C. Brachiocephalic artery - Maximum and mean velocity, colour map just prior to bifurcation.	
D. Left common carotid artery (LCCA) - Maximum and mean velocity, colour map and diameter at cross-section at the point that is approximately equal to 25 mm away from the branch at the aortic arch.	
E. Left subclavian artery (LSCA) - Maximum and mean velocity, colour map and diameter at cross-section of the point that is approximately equal to 25 mm away from the branch at the aortic arch.	
F. Coarctation repair site – Maximum and mean velocity, colour map and diameter at midpoint repair site.	

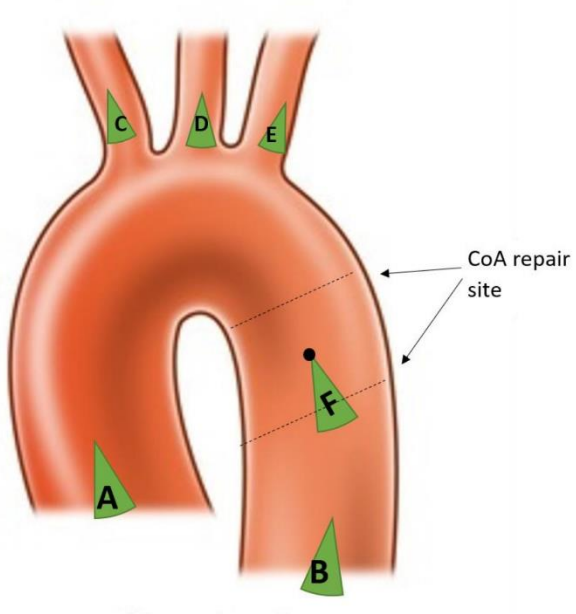

Figure 2: Post repair aorta measurements

PATIENT DATA FORM - PRE-REPAIR COARCTATION OF THE AORTA

PATIENT ID: _____

PATIENT AGE: _____

DATE OF PRE-REPAIR ECHOCARDIOGRAPH INVESTIGATION: _____

DATE OF PRE-REPAIR CTA INVESTIGATION: _____

COMMENT ON OTHER ACCOMPANYING HEART DEFECTS:
(FOR EXAMPLE, ABNORMAL BRANCH STRUCTURES OR BICUSPID AORTIC VALVE)

_____

_____

_____

_____

PRE-REPAIR ECHOCARDIOGRAPH SETUP CHECKLIST:

	CHECK
1. ECG pads connected	
2. Echo angle correction on	

MEASUREMENT CHECKLIST MATRIX:

Letters relate to Figure 1 *1 = Velocity (mean and max)* *2 = Colour map* *3 = Peak systolic diameter*

4 = Location label

#	1	2	3	4
A				
B				
C				
D				
E				
F				

COMMENT ON ANY DEVIATIONS TO POSITION OF MEASUREMENT THAT HAD TO BE MADE FROM INSTRUCTIONS IN

TABLE 1 IF ANY:

_____

_____

_____

_____

PATIENT DATA FORM - POST-REPAIR COARCTATION OF THE AORTA

PATIENT ID: _____

DATE OF POST-REPAIR ECHOCARDIOGRAPH INVESTIGATION: _____

DATE OF POST-REPAIR CTA INVESTIGATION (IF APPLICABLE): _____

COMMENT ON APPROACH TO REPAIR (STENTING, BALLOONING ETC):

_____

_____

_____

_____

POST-REPAIR ECHOCARDIOGRAPH SETUP CHECKLIST:

	CHECK
1. ECG pads connected	
2. Echo angle correction on	

MEASUREMENT CHECKLIST MATRIX:

Letters relate to Figure 2 *1 = Velocity (mean and max)* *2 = Colour map* *3 = Peak systolic diameter*

4 = Location label

#	1	2	3	4
A				
B				
C				
D				
E				
F				

COMMENT ON ANY DEVIATIONS TO POSITION OF MEASUREMENT THAT HAD TO BE MADE FROM INSTRUCTIONS IN Table 2 IF ANY:

_____

_____

_____

_____

8.4 APPENDIX 4: GRID INDEPENDENCE TEST

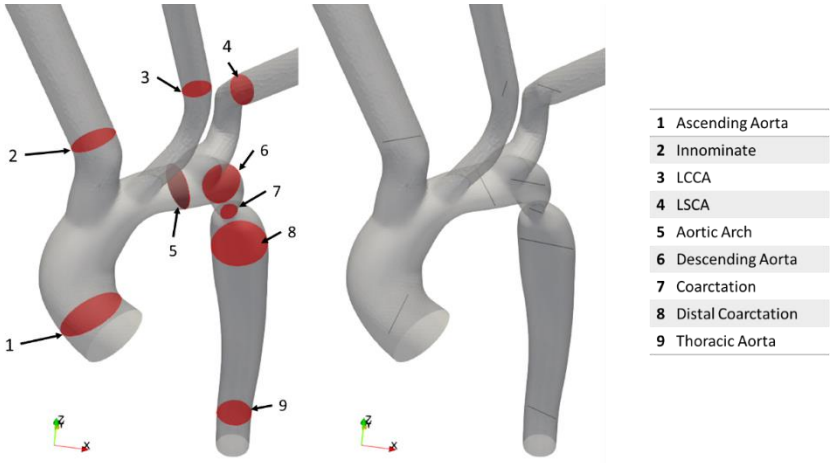

Figure 8-5: Figure illustrating cross section and diameter lines and their naming convention where pressure and velocity were assessed for grid independance

The grid independence study was conducted by comparing average pressures taken at 25 sample points on each plane in Figure 8-5 as well as the average value of the velocity magnitude along the diameters of the coarctation and ascending aorta patch. These velocity measurements were compared because the coarctation velocity was a focal point of the study and the ascending aorta, whose flow regime was fairly simple, was suspected to only vary as a result of the grid refinement and not numerical fluctuations. For interest sake, the velocity plots across each diameter are presented but only the ascending aorta and coarctation values were used. The results are presented graphically in Figure 8-6 to Figure 8-11 and Table 8-1 to Table 8-3.

It is interesting to note how, for most sites, the velocity and pressure plots seem to agree qualitatively. However, in case 1, where flow is chaotic due to the constriction, there are a few instances where there is variation between each mesh. In comparison, the study for case 3, where flow is somewhat more regular, each velocity profile matches quite closely. The discrepancies in the case 1 grid independence study was not investigated in this project and was note considered to be an indication that the result was dependant on the mesh. However, these discrepancies may be indication that turbulence models and more accurate boundary conditions are required.

The tabulated results of each grid independence test show that in most cases the result was independent of the grid with a very small deviation between refinements (<2%). However, there were some spurious deviations in the order of 50% in case 1 and case 2. These deviations were considered in the context of the values upon which they were based which were, compared to the global maxima, very small. Thus it was decided that, because the values that were used in calculating the error were very small, a small deviation for reasons other than

mesh refinement (numerical or computational) would correspond to a large deviation in refinement. Thus is was, in all three cases, found that the medium refinement where the number of cells were ~2 million was sufficiently fine.

8.4.1 Pre-Repair Case (Case 1)

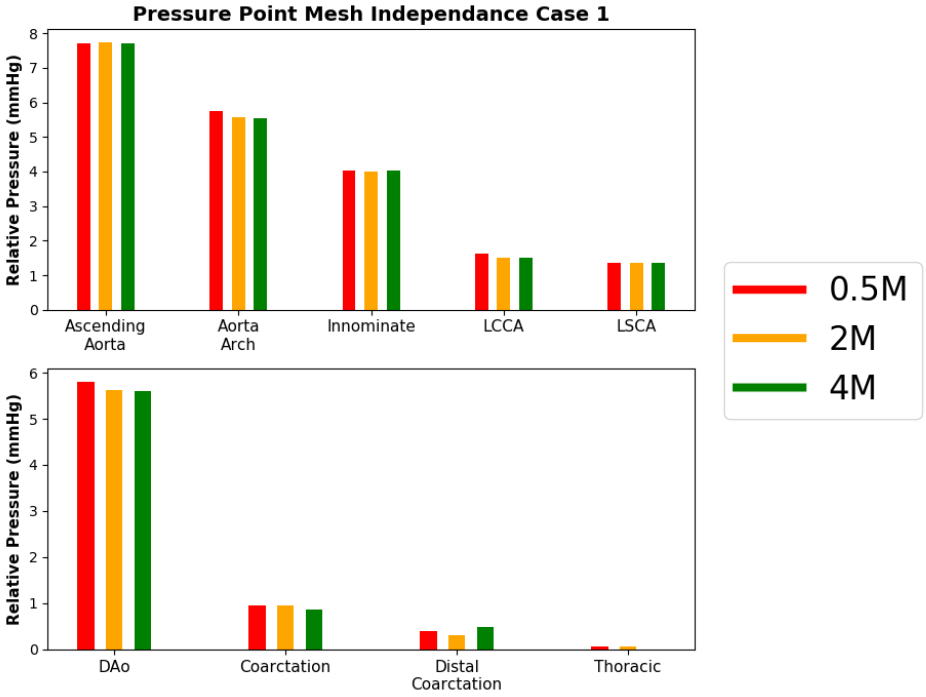

Figure 8-6: Probe data average relative pressure data using 25 sample points from each plane in Figure 8-5

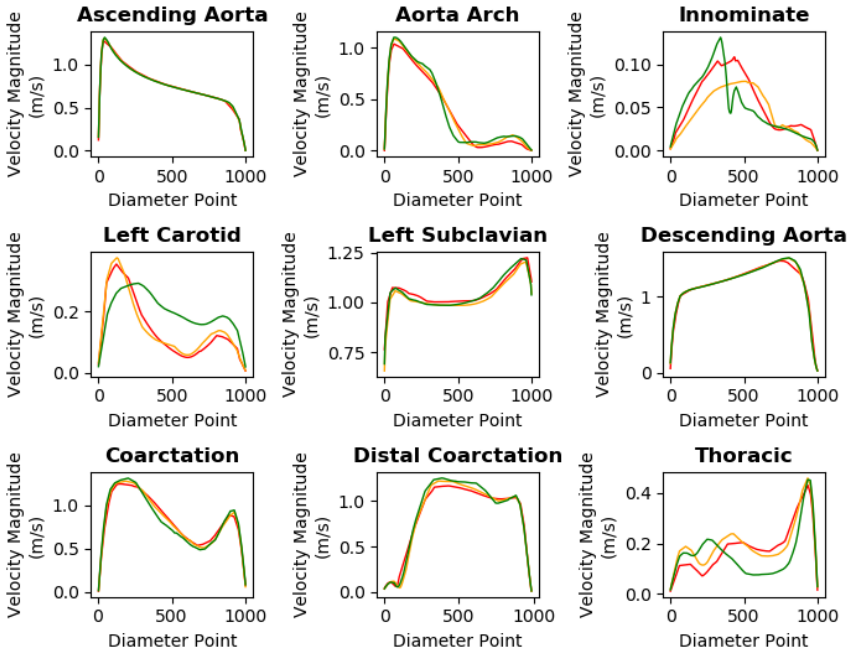

Figure 8-7: Velocity magnitude plot across each diameter line in Figure 8-5

Table 8-1: Tabulation of grid independence data from figures above where percentage errors are colour coded according to how they relate to the 5% threshold

CASE 1																	
		1		2	3		4	5	6	7		8	9				
		$V_{ave_{line}}$	$P_{Ave_{probe}}$	$P_{Ave_{probe}}$	$P_{Ave_{probe}}$		$P_{Ave_{probe}}$	$P_{Ave_{probe}}$	$P_{Ave_{probe}}$	$V_{ave_{line}}$	$P_{Ave_{probe}}$	$P_{Ave_{probe}}$	$P_{Ave_{probe}}$				
MESH 1		0.767	7.722	5.764	4.020		1.624	1.366	5.790	1.053	3.982	0.410	0.079				
MESH 2		0.767	7.729	5.565	4.010		1.515	1.358	5.623	1.030	3.887	0.320	0.100				
MESH 3		0.766	7.724	5.547	4.023		1.491	1.367	5.600	1.047	3.819	0.502	0.024				
	% Changes																
1st Refinement		0.026	0.091	3.460	0.241		6.752	0.629	2.885	2.108	2.385	21.82	27.07				
2nd Refinement		0.104	0.068	0.321	0.329		1.551	0.677	0.3984	1.610	1.749	56.83	75.91				

8.4.2 Post-Repair Case (Case 2)

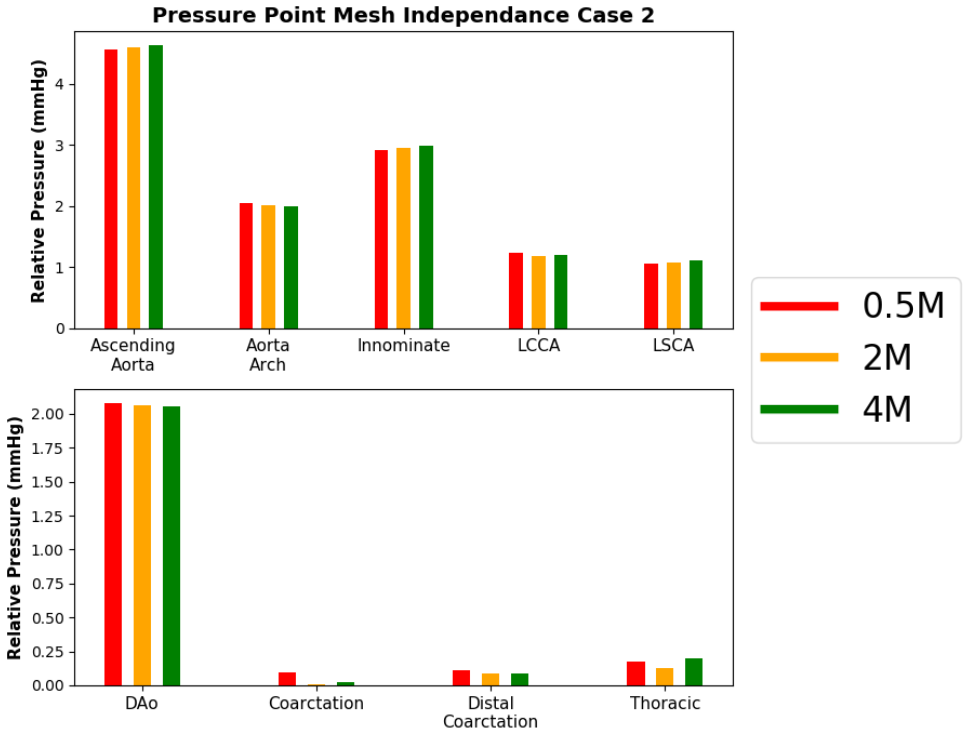

Figure 8-8: Probe data average relative pressure data using 25 sample points of case 2 from each plane in Figure 8-5

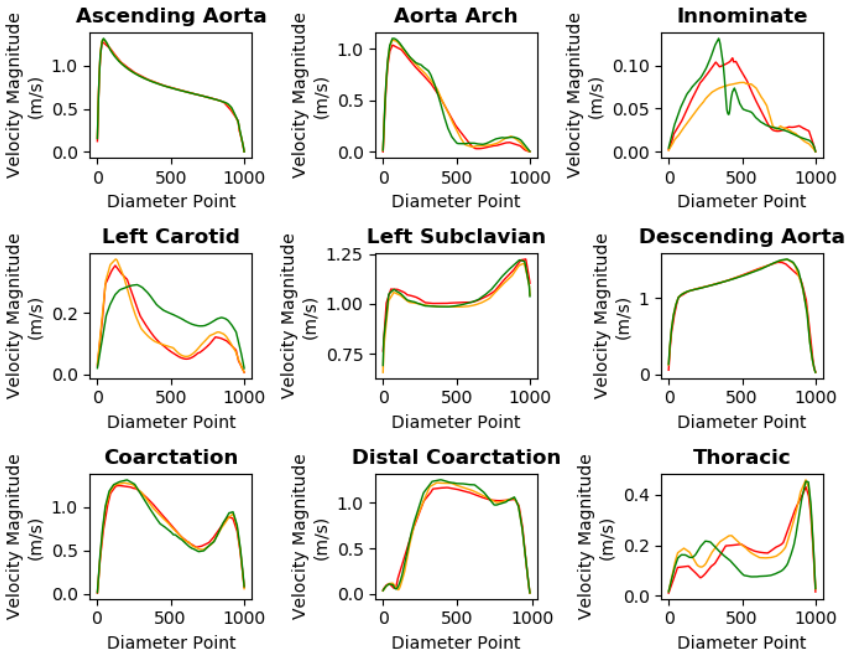

Figure 8-9: Velocity magnitude plot across each diameter line shown in Figure 8-5

Table 8-2: Tabulation of grid independence data from case 2 figures above where percentage errors are colour coded according to how they relate to the 5% threshold

CASE 2																	
	1		2	3	4	5	6	7		8	9						
	$V_{ave_{line}}$	$P_{Ave_{probe}}$	$P_{Ave_{probe}}$	$P_{Ave_{probe}}$	$P_{Ave_{probe}}$	$P_{Ave_{probe}}$	$P_{Ave_{probe}}$	$V_{ave_{line}}$	$P_{Ave_{probe}}$	$P_{Ave_{probe}}$	$P_{Ave_{probe}}$						
MESH 1	0.769	4.563	2.044	2.908	1.228	1.058	2.082	0.919	0.128	0.108	0.200						
MESH 2	0.768	4.601	2.014	2.940	1.176	1.076	2.063	0.924	0.064	0.090	0.165						
MESH 3	0.768	4.622	1.991	2.978	1.192	1.101	2.057	0.934	0.068	0.085	0.218						
% Changes																	
1st Refinement	0.130	0.833	1.467	1.101	4.234	1.701	0.913	0.544	50	16.67	17.50						
2nd Refinement	0	0.456	1.142	1.293	1.361	2.323	0.291	1.082	6.250	5.556	32.12						

8.4.3 Healthy Aorta Case (Case 3)

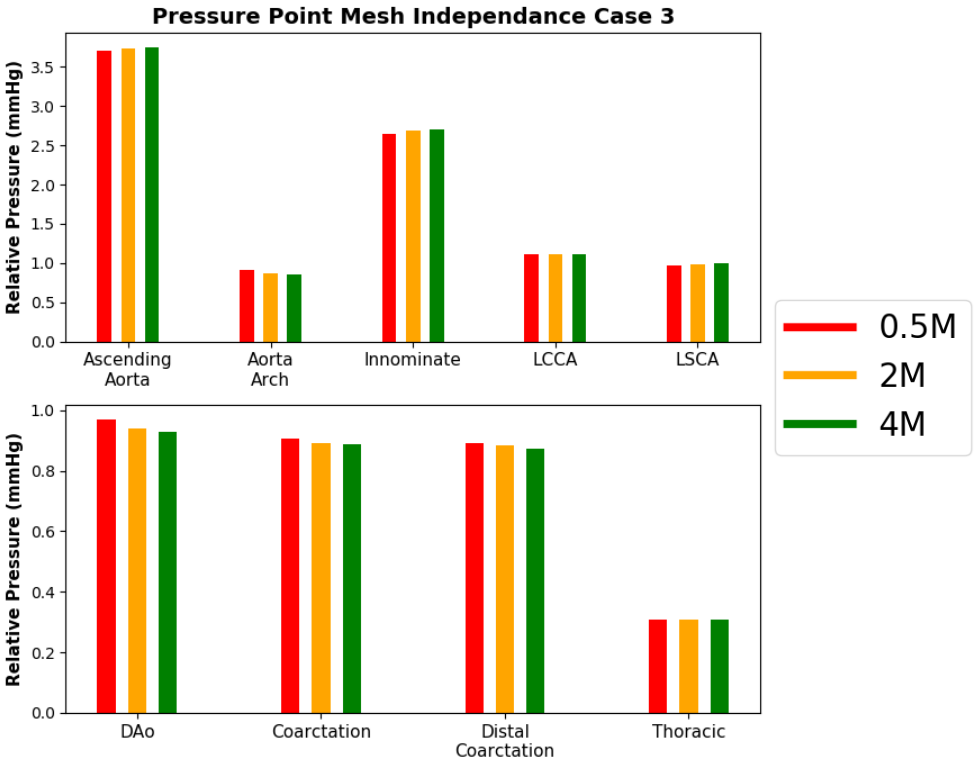

Figure 8-10: Probe data average relative pressure data using 25 sample points of case 2 from each plane in Figure 8-5

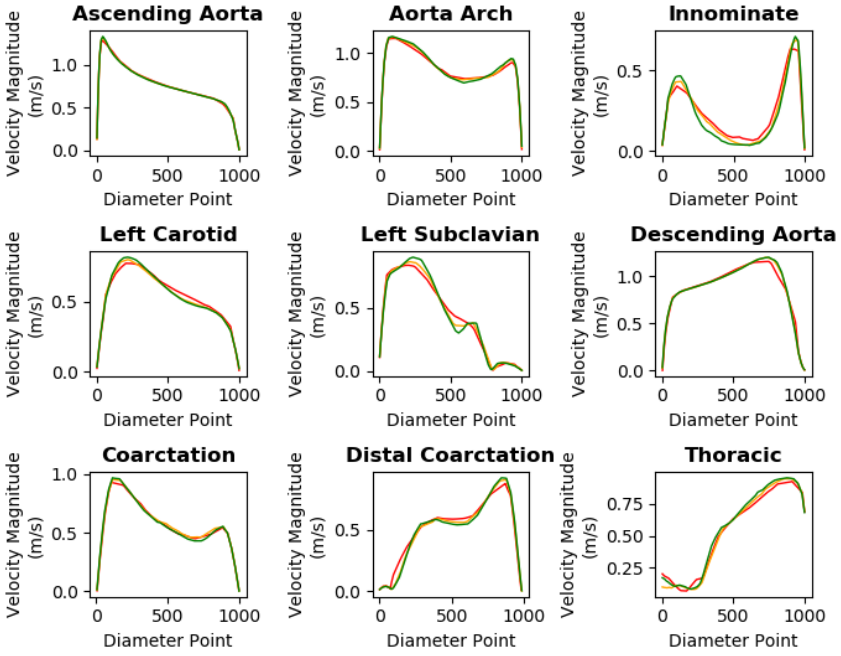

Figure 8-11: Velocity magnitude plot across each diameter line shown in Figure 8-5

Table 8-3: Tabulation of grid independence data from figures above where percentage errors are colour coded according to how they relate to the 5% threshold

CASE 1																	
	1		**2**	**3**	**4**	**5**	**6**	**7**		**8**	**9**						
	$V_{ave_{line}}$	$P_{Ave_{probe}}$	$P_{Ave_{probe}}$	$P_{Ave_{probe}}$	$P_{Ave_{probe}}$	$P_{Ave_{probe}}$	$P_{Ave_{probe}}$	$V_{ave_{line}}$	$P_{Ave_{probe}}$	$P_{Ave_{probe}}$	$P_{Ave_{probe}}$						
MESH 1	0.7687	3.712	0.905	2.650	1.119	0.974	0.9703	0.4467	0.9045	0.8901	0.3408						
MESH 2	0.7680	3.734	0.874	2.684	1.105	0.984	0.941	0.4491	0.889	0.885	0.341						
MESH 3	0.7677	3.745	0.851	2.704	1.106	0.999	0.929	0.4504	0.888	0.873	0.337						
	% Changes																
1st Refinement	0,091	0,59	3,42	1,28	1,25	1,02	3,02	0,53	1,71	0,57	0,058						
2nd Refinement	0,039	0,29	2,63	0,74	0,09	1,52	1,27	0,28	0,11	1,35	1,17						

8.5 APPENDIX 5: EXAMPLE HPC JOB SUBMISSION FILE

```
#!/bin/bash
#PBS -P MECH1194
#PBS -l select=1:ncpus=24:mpiprocs=24:nodetype=haswell_reg
#PBS -q smp
#PBS -l walltime=24:00:00
#PBS -o /home/lswanson/lustre/foamJobs/mesh_refArch/tet1/simOut/
#PBS -e /home/lswanson/lustre/foamJobs/mesh_refArch/tet1/simerr/
#PBS -m abe
#PBS -M liam.swanson.hpc@gmail.com

# Set this environment variable explicitly.
export
PBS_JOBDIR=/home/lswanson/lustre/foamJobs/coarctation/tetMesh/unrepaired/tetcoa0

# Explicitly change to the job directory
cd $PBS_JOBDIR
nproc=`cat $PBS_NODEFILE | wc -l`
exe=icoFoam

echo "FoamFile" > system/decomposeParDict
echo "{"  >> system/decomposeParDict
echo "  version             2.0;" >> system/decomposeParDict
echo "  format            ascii;" >> system/decomposeParDict
echo "  class       dictionary;" >> system/decomposeParDict
echo "  object decomposeParDict;" >> system/decomposeParDict
echo "}"  >> system/decomposeParDict
echo "numberOfSubdomains " $nproc ";" >> system/decomposeParDict
echo "method scotch;" >> system/decomposeParDict

decomposePar -force > decompose.out
mpirun -np $nproc -machinefile $PBS_NODEFILE $exe -parallel > foam.out
reconstructPar -latestTime > reconstruct.out
```

8.6 APPENDIX 6: CONFERENCES AND PUBLICATIONS

8.6.1 Conferences

1. *The development of a computational fluid dynamics pipeline for the study of tetralogy of Fallot and coarctation of the aorta in a developing world context.* Poster presentation. The Inaugural PROTEA Workshop. 13-15 March 2019. Southern Sun Newlands Hotel, Cape Town, South Africa.
2. *The Development of an open source CFD pipeline for the study of coarctation of the aorta and tetralogy of Fallot in a developing world context*. Oral presentation. 6th International Conference on Computational and Mathematical Biomedical Engineering. 10-12 June 2019. Tohoku University, Sendai City, Japan.
3. *The development of a computational fluid dynamics pipeline for the study of tetralogy of Fallot and coarctation of the aorta in a developing world context.* Poster presentation. European Society of Cardiology Congress 2019. 31 August – 4 September 2019. Paris expo Porte de Versailles, Paris, France.

8.6.2 Publications

1. Swanson L, Owen B, Keshmiri A, Deyranlou A, Aldersley T, Lawrenson J, Human P, De Decker R, Fourie B, Comitis G, Engel ME, Keavney B, Zühlke L, Ngoepe M and Revell A, (2020), "A Patient-Specific CFD Pipeline Using Doppler Echocardiography for Application in Coarctation of the Aorta in a Limited Resource Clinical Context". Front. Bioeng. Biotechnol. 8:409. doi: 10.3389/fbioe.2020.00409